

Toward Sustainable, Colorless, and Transparent Photovoltaics: State of the Art and Perspectives for the Development of Selective Near-Infrared Dye-Sensitized Solar Cells

Fionnuala Grifoni, Matteo Bonomo, Waad Naim, Nadia Barbero, Thomas Alnasser, Iva Dzeba, Marco Giordano, Arshak Tsaturyan, Maxence Urbani, Tomas Torres, Claudia Barolo,* and Frédéric Sauvage*

Dye-sensitized solar cell (DSSC) is one of the promising photovoltaic (PV) technologies for applications requiring high aesthetic features combined with energy production such as building integration PV (BIPV). In this context, DSSCs have the ability to be wavelength selective, thanks to the development of new sensitizers by molecular engineering. The long history of dye research has afforded is technology different colorations for reaching panchromatic light absorption. However, nearly 45% of radiation from sunlight lies in the near-infrared (NIR) region, where human cones are not sensitive. This review provides the reader with key information on how to selectively exploit this region to develop colorless and transparent PV based on DSSC technology. Besides selective NIR absorbers, the triptych photoanode, counter-electrode, and redox mediator are together contributing to reach high aesthetic features. Details of all the components, interplay, and an opinion on the technological limitations to reach colorless and transparent NIR-DSSC are herein discussed in relationship with BIPV applications.

we registered a rise of power installed from renewable sources during the last decade, a significant amount of effort is still necessary to introduce more substantially renewable energies into the energy mix to fulfill the future demand. In this context, solar energies and, more particularly, PV technologies are at the center of an important stake. According to EU Market Outlook for Solar Power, the year 2020 witnessed the most substantial growth of solar energy production in Europe since 2010.^[1]

The dominant silicon-based technologies represent a market share of ca. 90%. However, emerging technologies are being under exploration to improve solar competitiveness and find new applications. The concept of transparent PV modules has emerged to render the solar panels visually non-intrusive, an important aspect

for building, automotive, or urban-street integration. Different approaches have been followed: from the extremely thin opaque absorber to wavelength-selective thin-film PV, for which only the non-visible part of the solar spectrum is converted.^[2–8]

1. Introduction

One current challenge for humanity is to revolutionize the way energy is produced, distributed, and consumed. Even though

F. Grifoni, W. Naim, T. Alnasser, I. Dzeba, F. Sauvage
Laboratoire de Réactivité et Chimie des Solides
Université de Picardie Jules Verne (UPJV)
CNRS UMR 7314, 33 rue Saint Leu, Amiens 80039, France
E-mail: frederic.sauvage@u-picardie.fr

M. Bonomo, N. Barbero, M. Giordano, A. Tsaturyan, C. Barolo
Dipartimento di Chimica
NIS Interdepartmental and INSTM Reference Centre
Università degli Studi di Torino
Via Pietro Giuria 7, Torino 10125, Italy
E-mail: claudia.barolo@unito.it

 The ORCID identification number(s) for the author(s) of this article can be found under <https://doi.org/10.1002/aenm.202101598>.

© 2021 The Authors. Advanced Energy Materials published by Wiley-VCH GmbH. This is an open access article under the terms of the Creative Commons Attribution License, which permits use, distribution and reproduction in any medium, provided the original work is properly cited.

DOI: 10.1002/aenm.202101598

A. Tsaturyan
Institute of Physical and Organic Chemistry
Southern Federal University
Rostov-on-Don 344090, Russia

M. Urbani, T. Torres
Instituto Madrileño de Estudios Avanzados (IMDEA)-Nanociencia
c/Faraday, 9, Cantoblanco, Madrid 28049, Spain

T. Torres
Departamento de Química Orgánica
Universidad Autónoma de Madrid
Madrid 28049, Spain

T. Torres
Institute for Advanced Research in Chemical Sciences (IAdChem)
Universidad Autónoma de Madrid
Madrid 28049, Spain

C. Barolo
ICxT Interdepartmental Centre
Università degli Studi di Torino
Via Lungo Dora Siena 100, Turin 10153, Italy

The theoretical limit of power conversion efficiency (PCE) for a single junction wavelength-selective transparent photovoltaic (TPV) technology, combining UV-selective and NIR-selective absorption, with an average visible transmittance (AVT) of 100% is 20.5%. In practice, only 10.8% can be expected after considering all optical losses from the selective conversion of both UV and NIR region. For the same AVT, the PCE is theoretically lower for nonselective broadband absorbing cells. Hence, selective TPV, i.e., selective conversion of either the UV and/or NIR part of the solar spectrum, represents an important stake for the advancement of such TPV technologies.^[9]

The only technologies that can afford selective conversion in the NIR are molecular-based ones, such as organic PV (OPV), luminescent solar cells (LSC), quantum dots solar cells (QDSC), and dye-sensitized solar cells (DSSC). For those, light absorption involves electronic transitions from discrete levels and can be adjusted through the tuning of the molecular structure, in contrast with the crystalline semiconductors for which unselective photon absorption occurs. For example, the first selective TPV was based on an OPV, which achieved 1.3% PCE and an AVT of 65%.^[10] Soon after, this technology made noteworthy progress with Chen et al., who achieved 4% PCE and an AVT of 64%.^[11] On the other hand, LSC technology has displayed the highest value for AVT of 88.3%, with a lower PCE of 0.4%.^[12,13] In between these technologies, DSSC emerged to be one of the most interesting semitransparent/transparent PV technologies because i) the dye absorbance can potentially exploit selectively the near-infrared (NIR) part of the solar spectrum, which represents ca. 45% of the solar irradiance until 1700 nm^[14] (**Figure 1**), ii) they are based on optically transparent conductive oxide glass that affords to achieve high transparency in the visible range and iii) they can also be associated with tandem applications in association with a UV top cell to maximize light capturing outside the human eyes photopic response. Given the multiple advantages described above, the potential outcome of developing a sustainable colorless and transparent DSSC module appears highly promising.

After introducing the working principle and the specific needs for NIR-DSSCs, an overview of the aspects to be considered for the development of new efficient transparent materials and the

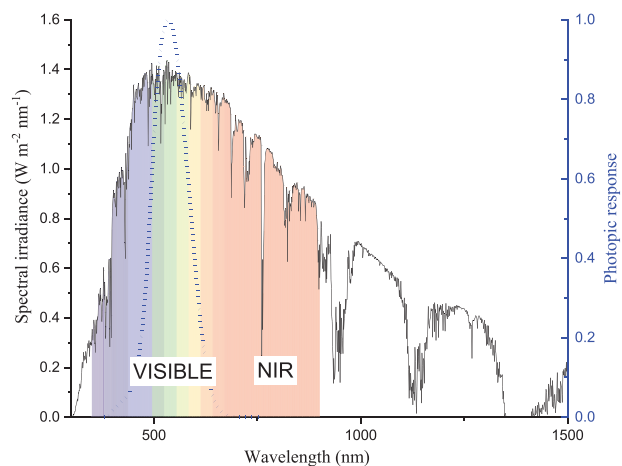


Figure 1. Solar radiation spectrum at sea level on a clear day (A.M. 1.5G) and photopic response in blue.

key characterization techniques needed for the optimization of the materials is described in Section 2. Section 3 discusses individually each component, namely sensitizer (Section 3.1), photoanode (Section 3.2), redox couples (Section 3.3), counter-electrode (Section 3.4) and antireflective coating (Section 3.5) with the aim to present potential exploration for NIR-DSSC technology. For this type of application, the power conversion efficiency (PCE) and transparency/color evaluation are the same weighted metrics. Our assessment on how the transparency and device coloration need to be reported is herein discussed.

2. Materials Design and Characterization toward NIR-DSSCs

NIR-DSSC does not only mean developing new materials. It also calls for possible adaptation of existing time-resolved characterization techniques to monitor the NIR region. In this section, it is given an overview of the concept of transparency, injection, regeneration and recombination processes. It affords to emphasize the possible issues that can be encountered by narrowing the absorber's bandgap.

2.1. Device Structure and Working Principles

DSSC technology is the sole existing electrochemical PV technology, thus composed of two electrodes separated by an electrolyte (**Figure 2**). The photoanode is at its heart. It is composed of a large bandgap mesoporous layer typically of anatase TiO₂ nanoparticles. A self-assembled monolayer of dye is chemically adsorbed on the nanocrystals to ensure incident sunlight absorption.^[15] The counter electrode (CE) consists of an electrocatalyst layer deposited upon FTO glass to facilitate the electron transfer for the reduction of the oxidized form of the redox mediator, typically I₃⁻/I⁻ or Co(III/II) complexes are used.

The operating principle in DSSCs under light and load involves four main processes with different time scales: i) light absorption by the dye followed by electron injection from the dye excited-state to the conduction band of the semiconductor (fs-ps), ii) dye regeneration (ns-μs) iii) electron transport towards collection (ms) and iv) diffusion of the redox mediator to/from the counter electrode (ms-s). A more detailed description of these processes can be obtained in the literature.^[16-20] The focus here will be given to the limiting factors for transparent selective NIR-DSSCs. The electron injection can enter in competition with the deactivation processes of the excited states. The dye regeneration can also compete with the back electron transfer reaction (i.e., geminate recombination).

The successful production of current relies not only on reaching a quantitative yield of electron injection and dye regeneration but also requires the minimization of the nongeminate recombination dynamic compared to the transport time. Each unfavorable deactivation path requires to be at least 10³ times slower than the favorable pathway to reach 99+ % yield. One important challenge to overcome when integrating lower bandgap NIR dyes is nested in keeping successful energy alignment to favor both injection and regeneration steps. This restriction limits enormously the number of dyes that can be adapted

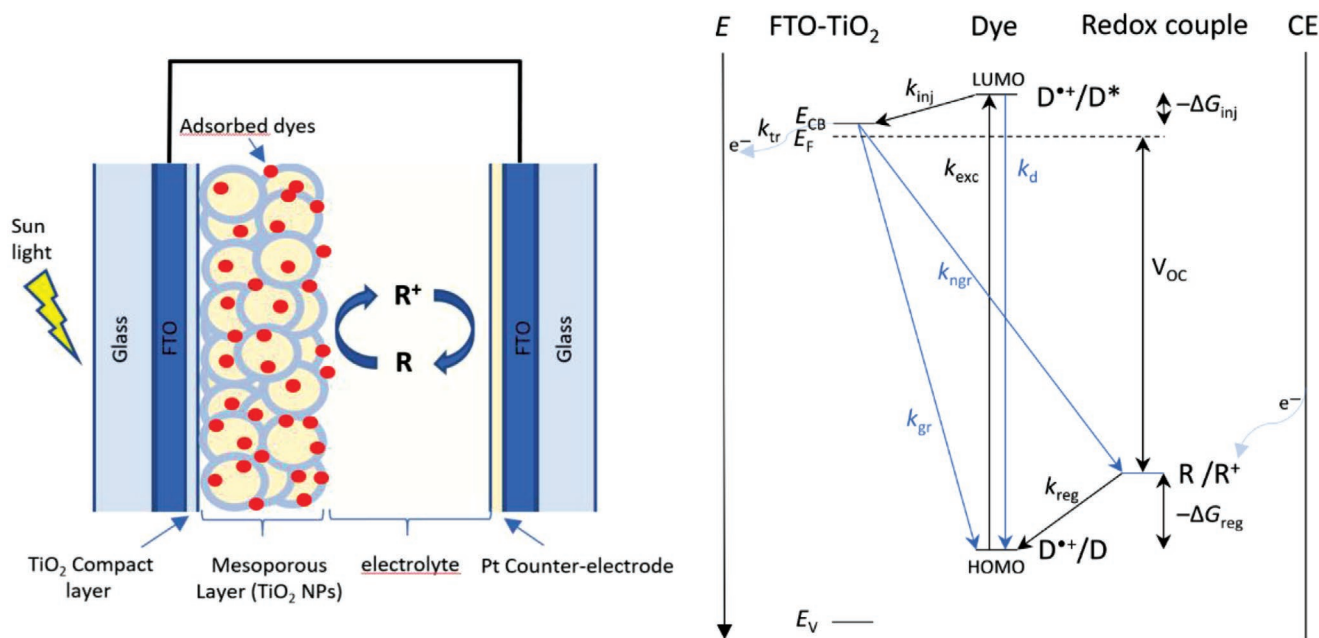


Figure 2. Schematic representation of a DSSC (left) and the different charge transfer processes taking place under load and illumination (right): Photoexcitation (k_{exc}), electron injection (k_{inj}), deactivation of the excited state of the dye (k_d), dye regeneration (k_{reg}), geminate electron recombination (k_{gr}), nongeminate electron recombination (k_{ngr}), electron diffusion transport (k_{dif}), redox couple reduction at the CE. $-\Delta G_{inj}^{\circ}$ and $-\Delta G_{reg}^{\circ}$, are corresponding to the driving force energy for electron injection and dye regeneration, respectively being the potential difference between the conduction band of semiconductor and LUMO level of the dye. $-\Delta G_{reg}^{\circ}$, corresponds to the driving force for regeneration being the potential difference between the ground state oxidation potential of the dye $E^{\circ}(D^{+}/D)$ and the redox couple $E^{\circ}(R^{+}/R)$.

to the benchmark TiO₂ nanoparticles and the conventional redox mediators introduced so far. Needless to remind that all dyes developed for this technology since the seminal work of Graetzel et al. were based on matching with the conduction band edge of TiO₂ and the chemical potential of iodine/iodide redox mediator. This duo upper bounds experimentally the light conversion to around 920 nm considering ca. 500 mV energy losses related to overpotentials needed for both injection and dye regeneration. Looking outside this box with a longer-term view of perspectives, clear opportunities exist on developing NIR-DSSC, however at the cost of totally rethinking the materials to operate specifically with the NIR dye and their associations.

2.2. Transparency and Aesthetic Assessment

One main outcome for prompting the development of NIR-DSSC is the selective transparent PV (TPV). The first key metric to evaluate is the average visible transmittance value (AVT). AVT is defined as the weight of the integration of the transmission spectrum of the PV device against the photopic response of the Human eye; as such, AVT is calculated from the following equation:

$$AVT = \frac{\int T(\lambda)V(\lambda)S(\lambda)d(\lambda)}{\int V(\lambda)S(\lambda)d(\lambda)} \quad (1)$$

where λ is the wavelength, T is the transmission, V is the photopic response and S is the solar photon flux (A.M. 1.5G). The absorption spectrum of the human eyes photopic response is shown in Figure 1. The theoretical PCE limit of a single

junction selective TPV technology has been calculated to 21% with an AVT of 100% while being 0% for a nonwavelength selective PV.^[9] It decreases to a maximum of 14% PCE in the case of a non-wavelength selective for an AVT of 50%, before to rapidly decline for AVT greater than 50%. For a nonwavelength selective DSSC, a maximum of 44% AVT was reported for semitransparent DSSCs based on the visible absorbing benchmark organometallic Ru complex dye (N719).^[21,22] In 2014, Han et al. reported a green see-through DSSC with a PCE of 3.66% and a maximum transmittance value of 60% at 560 nm. Their work is based on the cosensitization between two efficient dyes absorbing in the visible range: a D- π -A dye (Y1) for blue-light conversion ($\lambda = 400$ nm) and a squaraine dye (HSQ5) as a nearly NIR dye ($\lambda = 700$ nm) leading to a final green semitransparent device.^[23] Recently, a photochromic semi-transparent DSSC was also proposed by Demadrille et al., reporting an AVT value of 59% in the dark without photovoltaic activity. The AVT value decreases to 27% upon illumination leading to a maximum PCE of 3.7%.^[24] To empower the adoption of this technology in the TPV market, the development of NIR-wavelength-selective DSSC has been rapidly targeted as both transparency and efficiency can be finely adjusted. The first colorless and transparent NIR-DSSC concept is based on cyanine dye coded VG20 reaching a remarkable AVT of 76%.^[25] This dye shows a maximum PCE of 3.1%, which is a modest value given the state of the art in opaque technologies but brings important added values in terms of aesthetic and integration opportunities. As the PCE and AVT are often inversely related, Traverse et al. proposed introducing a new metric, the Light Utilization Efficiency (LUE), to rationalize the PCE and AVT values.^[12] LUE is defined as the product of AVT and PCE:

$$LUE = AVT \times PCE \quad (2)$$

The LUE compares different TPV technologies against theoretical limits and represents an overall system efficiency from both electrical and aesthetic aspects.

To define the acceptable range of optical properties of the TPV by the windows industry, the quantification of the ability of the devices to render some colors is becoming another fundamental metric. As it is not possible to measure color directly, it is always based on the comparison.^[26] Moreover, under different illuminants, colors may appear different. Therefore, a reference system is mandatory. This conscious or subconscious comparison of the color appearance of objects under a reference or a standard illuminant is defined as color rendering.^[27] The Commission Internationale de l'Eclairage (CIE), which is considered to be the authority on the science of light and color, introduced the color rendering index (CRI) as a metric to describe quantitatively how accurately the color of a given object is rendered either from a light source or through a transparent medium as the TPV devices, with respect to an "ideal" illumination source (Figure 3). CRI value is calculated within an evolution of functions as an average score on eight different test color samples. Starting with the definition of the color matching functions $\bar{x}(\lambda)$, $\bar{y}(\lambda)$ and $\bar{z}(\lambda)$ as the numerical description of the chromatic response of the observer (the $\bar{y}(\lambda)$ function is identical to the eye photopic response), reflecting that human color vision possesses trichromacy (since the cone sensitivity functions are usually not used directly in color calculation), the CIE introduced in 1931 the tristimulus values (X, Y, Z) as a replacement for the red, green, blue system, giving the stimulation of each of these three primary colors needed to match the color of the reference. As such, the tristimulus values X, Y, and Z are determined considering the light source's spectral power distribution (SPD), A.M. 1.5G(λ) in the case of TPV, and SPD of the tested sample or rather the transmittance curve, $\tau(\lambda)$, of the TPV device. The tristimulus values of the light transmitted by a TPV are:

$$X_t = \sum_{380}^{780} A.M.1.5G(\lambda) \tau(\lambda) \bar{x}(\lambda) \Delta(\lambda) \quad (3)$$

$$Y_t = \sum_{380}^{780} A.M.1.5G(\lambda) \tau(\lambda) \bar{y}(\lambda) \Delta(\lambda) \quad (4)$$



Figure 3. Illustration of the effect of CRI value on color perception.

$$Z_t = \sum_{380}^{780} A.M.1.5G(\lambda) \tau(\lambda) \bar{z}(\lambda) \Delta(\lambda) \quad (5)$$

In addition, the spectral reflectivity of each of the eight standard test color samples, $\beta_i(\lambda)$, needs to be taken into consideration in deriving the 1931 CIE tristimulus values (of light transmitted by the TPV and reflected by each of the eight test colors):

$$X_{t,i} = \sum_{380}^{780} A.M.1.5G(\lambda) \tau(\lambda) \beta_i(\lambda) \bar{x}(\lambda) \Delta(\lambda) \quad (6)$$

$$Y_{t,i} = \sum_{380}^{780} A.M.1.5G(\lambda) \tau(\lambda) \beta_i(\lambda) \bar{y}(\lambda) \Delta(\lambda) \quad (7)$$

$$Z_{t,i} = \sum_{380}^{780} A.M.1.5G(\lambda) \tau(\lambda) \beta_i(\lambda) \bar{z}(\lambda) \Delta(\lambda) \quad (8)$$

Subsequently, the relative magnitudes of these tristimulus values are calculated, obtaining the chromaticity coordinates (x , y , and z). However, only (x , y) coordinates are needed to describe the color into a 2D chromaticity diagram (CIE1931 color space). As it is expedient for the color difference to be proportional to the geometrical difference in the chromaticity diagram, the CIE introduced the (u , v) chromaticity coordinates for the CIE1976 color space, also calculated from the X, Y, Z tristimulus values.

$$x = \frac{X}{X+Y+Z} \quad (9)$$

$$y = \frac{Y}{X+Y+Z} \quad (10)$$

$$z = \frac{Z}{X+Y+Z} \quad (11)$$

$$u = \frac{4X}{X+15Y+3Z} \quad (12)$$

$$v = \frac{6X}{X+15Y+3Z} \quad (13)$$

Moreover, the CRI calculation procedure takes into account the adaptive color shift that follows from the human ability of chromatic adaptation to certain illumination environments without substantial loss of color perception. Thus the (u , v) coordinates are transformed into (c , d) coordinates, leading to the calculation of the trichromatic coordinates correction after distortion by chromatic adaptation ($u'_{t,i}$, $v'_{t,i}$).

$$c_n = \frac{4 - u_n - 10v_n}{v_n} \quad (14)$$

$$d_n = \frac{1.708v_n + 0.404 - 1.481u_n}{v_n} \quad (15)$$

where $n = t$ for the test sample t,i the for test sample with the contribution of test color samples reflectivity and r for reference illuminant.

$$u'_{i,i} = \frac{10.872 + 0.8802 \frac{c_{t,i}}{c_i} - 8.2544 \frac{d_{t,i}}{d_i}}{15.518 + 3.2267 \frac{c_{t,i}}{c_i} - 2.0636 \frac{d_{t,i}}{d_i}} \quad (16)$$

$$v'_{i,i} = \frac{5.520}{15.518 + 3.2267 \frac{c_{t,i}}{c_i} - 2.0636 \frac{d_{t,i}}{d_i}} \quad (17)$$

Now, as the brightness (of a light source) and the lightness (for an object) are factors that define the color seen, CIE introduced the brightness/lightness coordinate W^* , that along with derived adaptive color-shifted chromaticity coordinates, we obtain the 1964 CIE uniform color space.

$$W^*_{i,i} = 25 \left(\frac{100Y_{t,i}}{Y_t} \right)^{\frac{1}{3}} - 17 \quad (18)$$

$$u^*_{i,i} = 13W^*_{i,i} (u'_{i,i} - 0.1978) \quad (19)$$

$$v^*_{i,i} = 13W^*_{i,i} (v'_{i,i} - 0.3122) \quad (20)$$

Nonetheless, the quantification of the change in chromaticity coordinates of the test color samples when illuminated with the reference source or the transmitted source is a key step to evaluate the resultant color change, used in the final step in calculating the color rendering index; as such, the CRI is calculated from the following equation:

$$CRI = \frac{1}{8} \sum_{i=1}^8 \left[100 - 4.6 \sqrt{(\Delta u^*_i)^2 + (\Delta v^*_i)^2 + (\Delta W^*_i)^2} \right] \quad (21)$$

CRI varies between 0 and 100. A value greater than 90% is generally considered to be of excellent quality. Mallick et al. introduced CRI metric to assess the visual comfort of DSSC. They report values between 83 and 93% for colored-semi-transparent DSSCs. For the first transparent NIR-DSSC, the work on VG20 dye already demonstrated very high CRI values lying between 92.1% and 96.3% depending on the electrolytes (vide infra).

Based on the CIE1976, the 3D color space CIELAB was also introduced and can be found as an alternative color metric to x,y chromaticity diagram. In this color space, the chromaticity coordinates used are a^* , b^* while L^* indicates lightness, representing the human perception of contrast for a given (a^* , b^*), and are also determined from the X, Y, Z tristimulus values.^[28] These values should also be considered other than the CRI for a complete and clear color analysis, as they are considered a standard in the window industry. On this scale, a^* value indicates the red-green component of the color, while the yellow and blue components are represented on the b^* axis. L^* is represented on a vertical axis with values from 0 (black) to 100 (white). An important point when dealing with the CIELAB color space is that the CRI requirement differs depending on the a^* , b^* values; negative a^* and b^* values, revealing a blue-tinted color, require CRI > 90% whereas a CRI > 95% is needed for yellow- or red-tinted colors corresponding to a^* and b^* close to zero or positive.^[29]

To validate the measurements carried on TPV, Lunt's group has also introduced the photon balance at every wavelength as a necessary consistency check.^[29] The sum of the independent measurements gives the photon balance, and if this value is equal or lower to 1, then the single evaluations are verified. The measurements to consider for this validation are the external quantum efficiency EQE(λ), transmittance $T(\lambda)$, and reflectance $R(\lambda)$ and have to be evaluated on the transparent device:

$$EQE(\lambda) + T(\lambda) + R(\lambda) \leq 1 \quad (22)$$

The non-fulfillment of this consistency check suggests an overestimation in one of these three data sets that may be deriving from an incorrect way of measuring. To prevent such failure, it is important to avoid the "double-pass" effect by placing a matte black background and considering the correct area of the device in the photovoltaic performance characterization. Furthermore, the evaluation of transmittance and reflectance of the transparent device should be in the absence of a reference sample in the case of a double-beam spectrometer since reflections on solid films become more complex and cannot be easily referenced to a piece of glass. A more detailed explanation of how to accurately measure these parameters is found in previous works of Lunt's group.^[29]

2.3. Time-Resolved Characterization Techniques

Narrowing the dye's bandgap value raises important defies in reducing all internal energy losses to reach a sufficiently high level of performance. Different time-resolved characterization techniques have been specifically developed or adapted for the characterization of DSSC to monitor electron injection and dye regeneration kinetics.

2.3.1. Monitoring of Electron Injection

Electron injection is an ultrafast process taking place within ps down to fs-time scale. This calls for ultrafast spectroscopies such as femtosecond pump-probe transient absorption spectroscopy^[30,31] or fluorescence up-conversion.^[32] Alternatively, less complex spectroscopies can already provide some valuable indications, such as time-correlated single-photon counting (TCSPC), albeit the latter has a limited time resolution of few tenths of picoseconds. Thus, TCSPC does not always provide a robust assessment of the competing mechanisms that can occur, such as energy transfer processes between monomer and aggregates, intersystem crossing, or injection competition between aggregates and monomer.

The injection quantum yield (ϕ_{inj}) is the value that defines how efficient state the electron injection is compared to the excited states' deactivation paths. It can be evaluated either from the rate constants of the processes involved, namely k_{inj} and k_d (Equation 23) or from the change of absorbance due to the formation of transients dye (radical) cation, ΔA_c and electron, ΔA_e according to Equation 24 for which the molar absorption coefficient, ϵ_c is required, and where T and N_0 represent the transmittance of the excitation light and the number of incident

excitation photons per unit area. Several reported methods are used to determine the molar absorption coefficient of the dye (radical) cation.^[19,33] For an efficient electron injection, k_{inj} should be two orders of magnitude higher than k_d .

$$\phi_{inj} = \frac{k_{inj}}{k_{inj} + k_d} \quad (23)$$

$$\phi_{inj} = \frac{\Delta A_c}{\epsilon_c (1-T) N_0} = \frac{\Delta A_c}{\epsilon_c (1-T) N_0} \quad (24)$$

2.3.2. Monitoring of Dye Regeneration

Dye regeneration can be the second phenomenon limiting the IPCE value. Dye regeneration kinetic is studied using ns pump-probe transient absorption spectroscopy by following the depopulation of the transient dye (radical) cation in the presence (k_{reg}) or absence (k_{gr}) of the redox couple. The geminate recombination rate constant, or the back electron transfer from TiO_2 to the dye radical cation (k_{gr}) is a competitive process to the dye regeneration (k_{reg}), thus defining the regeneration yield (ϕ_{reg}) (Equation 25):

$$\phi_{reg} = \frac{k_{reg}}{k_{reg} + k_{gr}} = \frac{\tau_{gr}}{\tau_{gr} + \tau_{reg}} \quad (25)$$

It is common that the ground-state absorption spectra of the dye overlap with the transient absorption spectra of the formed dye's radical cation. The expansion of the spectral probe range towards the NIR region is helpful to probe the evolution of absorbance related to the free carrier population in the anatase TiO_2 .^[34]

3. Materials

The development of efficient colorless NIR-DSSC relies on the design of specific transparent materials with tailored properties. A trade-off between high AVT and high efficiency renders the selection of the materials more complicated than for opaque technologies. Throughout this section, it is selected different constituent materials possibly of interest for improving NIR-DSSC technology. The sustainability of the proposed materials is also considered since the final aim of technology industrialization.

3.1. NIR Sensitizers

Research and development of NIR sensitizers is at the heart of the NIR-DSSC problematics as it rules not only the efficiency as standard DSSCs but also the final level of aesthetic. A conventional photosensitizer requirement is to reach panchromatic absorption, covering all visible and near-infrared absorption, as they represent the main contributions to solar irradiance. A common approach toward panchromatic absorption is dye engineering to broaden its spectral response. A well-known example for Ru complexes is N749 dye, also known as "Black

Dye."^[35] The introduction of a terpyridyl ligand resulted in an extended response of 100 nm compared to the benchmark N719 dye. To further improve the weak absorption of Ru (II) dyes in the NIR, other routes have been explored like in the case of N1044 dye where the combination of the optical properties given by π -conjugated bipyridyl groups with the panchromatic response ensured by quaterpyridine ligands, led to an absorption broadness more extended than the Black Dye, with a conversion tail in the IPCE spectrum reaching 33% at 800 nm and extended till 910 nm.^[36] Nevertheless, the low molar extinction coefficient in the near-infrared region of this class of dyes led to the investigation of other sensitizers based on different transition metal or metal-free organic dyes and the use of NIR dyes as cosensitizers.^[37]

However, involving metal to ligand charge transfer (MLCT) transition in this class of dyes renders difficult the selective absorption of the NIR region. The design of a sensitizer fulfilling this requirement should stem from singlet-to-singlet transitions with narrowed gap energies. As a consequence, both electron injection and dye regeneration kinetics will be affected, therefore representing one important challenge in the optimization of such dyes and their interplay in the system with the selective contacts. In order to assure an effective electron injection, it is typically well-verified that the LUMO level should be located at least 0.2 eV above the conduction band edge of TiO_2 . This will place the LUMO level of the sensitizers at ca. -3.75 eV versus vac. and thus its HOMO level in the range of -5.25 eV versus vac. for a sensitizer with a bandgap in a range of 1.5 eV (ca. 820 nm). Specific dye designs are also required when replacing conventional redox mediators with a metal-based redox couple to afford successful dye regeneration. One approach consists of adding the bulky triarylamine building block with four alkyl chains known as "The Hagfeldt donor."^[38]

There is a great variety of NIR dyes that have been synthesized for DSSC.^[39] Nevertheless, to reach selective NIR-DSSC, the dye requires an absorption close to zero in the whole spectral region covered by the human cones. The different classes of dyes possessing energetic levels that can ensure an efficient injection while having a bandgap sufficiently narrow to selectively absorb the NIR region are limited. Mainly polymethine, phthalocyanines, and porphyrins are of interest.^[17,40-43]

3.1.1. Polymethine Dyes

Polymethine dyes are highly conjugated molecules well known for NIR absorption. They are characterized by a high molar extinction coefficient and easily tunable properties through modification of central core or lateral units. They have been first explored as sensitizers for silver halide photography, associated with other large bandgap semiconductor materials, and as probes for biological systems.^[44,45] By varying the length of the polymethine chain and the lateral groups' nature, it is possible to shift the $S_0 \rightarrow S_1$ transition from the visible towards the NIR region. However, one important drawback in this class of dyes is the self-aggregation, mainly when anchored onto the semiconductor surface. Aggregates are very detrimental not only for the device performance but also for transparency level since they can induce absorption band broadening or even

cause an onset of new absorption bands, which can overlap with the human eyes photopic response, therefore conferring device coloration.^[46] Aggregation can be mitigated either by a cosensitization approach, the addition of a deaggregating agent such as the chenodeoxycholic acid (CDCA) or via the introduction of bulky lateral units or long alkyl chains.^[46]

Squaraine Dyes: Squaraine dyes have been widely developed for applications in DSSC because of the large versatility offered by this molecular platform toward new molecular design.^[47,48] The core of the structure is a four-membered aromatic ring derived from squaric acid. Depending on the lateral units, they are categorized as unsymmetric or symmetric. The first beliefs were that unsymmetrical squaraine is needed to reach good performance thanks to the directionality created in the excited states. This led to the development of many derivatives, such as the most-known SQ01 by Nazeeruddin et al.^[49] (Table 1 entry 1). A $-C_8$ alkyl chain was inserted as N-alkyl substituent to reduce dye aggregation on the semiconductor's surface, leading to a PCE of 4.5% ($J_{sc} = 10.5 \text{ mA cm}^{-2}$, $V_{oc} = 603 \text{ mV}$, FF = 0.71). However, this dye is not red-shifted enough since the maximum absorption is at 636 nm only. The addition of an aromatic ring in the indolenine structure induced a bathochromic shift of 25 nm for SQ02 other than improving photovoltage and photocurrent with an overall 5.4% PCE ($J_{sc} = 11.3 \text{ mA cm}^{-2}$, $V_{oc} = 667 \text{ mV}$, FF = 0.72) (Table 1 entry 2).^[50] However, the flat benzoindolenine structure brings more pronounced π stacking. An effective approach for red-shifting was proposed by Geiger et al. who synthesized a squaraine dimer BSQ01, presenting a strong and sharp absorption at 730 nm (Table 1 entry 3).^[51] The presence of two chromophores units in the structure leads to a very high molar extinction coefficient ($\epsilon = 389\,000 \text{ M}^{-1} \text{ cm}^{-1}$). However, the performances of this type of dye were rather limited (PCE = 1.3% $J_{sc} = 3.11 \text{ mA cm}^{-2}$, $V_{oc} = 545 \text{ mV}$, FF = 0.76). Following this concept, Maeda et al. proposed the LSQ series that reached 2.3% PCE for LSQa dye ($J_{sc} = 9.05 \text{ mA cm}^{-2}$, $V_{oc} = 0.46 \text{ V}$, FF = 0.54) and strong absorption between 770 and 800 nm, however with tails in the visible range (Table 1 entry 4–6).^[52] Subsequently, trimers TSQ-a and TSQ-b were also developed by the same group.^[53] These dyes can absorb over 800 nm; however, they also show intense absorbance in the visible region, making them not suitable to reach a colorless device. This approach of oligomerization of squaraine was not further pursued because of the limited success and the high synthetic complexity.

Magistris et al. developed VG5 dye, where the simple introduction of a benz[c,d]indolenine unit shows a 36% IPCE at 800 nm with a tail of conversion up to 900 nm, though with low efficiency of 1.1% ($J_{sc} = 7.3 \text{ mA cm}^{-2}$, $V_{oc} = 350 \text{ mV}$, FF = 0.43) (Table 1 entry 7).^[54] The anchoring group in VG5 dye is not located on this benzoindolenine unit but on the other indolium ring. The opposite position does not show as good performances as Maeda et al. later demonstrated.^[55] A remarkable accomplishment was achieved by Han et al. with HSQ5.^[23] This hemisquaraine dye reached a maximum PCE of 2.3% when associated with a very thick opaque photoanode structure ($J_{sc} = 5.47 \text{ mA cm}^{-2}$, $V_{oc} = 603 \text{ mV}$, FF = 0.70) (Table 1 entry 8). Unfortunately, this dye partially absorbs in the visible range, jeopardizing its application in colorless devices.

The need for developing asymmetric squaraine was questioned following the development of the symmetrical VG1

dye showing similar performances to SQ01 counterpart dye (PCE = 4.6% $J_{sc} = 9.4 \text{ mA cm}^{-2}$, $V_{oc} = 629 \text{ mV}$, FF = 0.77) (Table 1 entry 9).^[56] It has two anchoring groups on the indolenine moieties and C_8 alkyl chains. VG1's IPCE spectrum is red-shifted of 15 nm and it generates more photocurrent due to the locked structure in the *cis* conformation, as also proved by Maeda and Han who inserted a dicyanovinylene unit as an electron-withdrawing group on the squaric core (SQM-1a) (PCE = 4.6% $J_{sc} = 9.4 \text{ mA cm}^{-2}$, $V_{oc} = 629 \text{ mV}$, FF = 0.77) (Table 1 entry 10).^[57] Since then, these different works seed many different structures. Viscardi et al. developed VG10 dye (Table 1 entry 11), incorporating for the first time two carboxylic acid directly conjugated on the benzoindolenine ring instead of on the N-alkyl substituent. It delivers a PCE of 6.2% ($J_{sc} = 13.6 \text{ mA cm}^{-2}$, $V_{oc} = 641 \text{ mV}$, FF = 0.70).^[58] Compared to its corresponding unsymmetrical squaraine VG13, VG10 also shows a slight red-shift absorption with a maximum at 673 nm. Han et al. demonstrated the advantages of positioning two carboxylic anchoring groups in terms of stability to suppress dye desorption (HSQ4 reaches a PCE = 5.6% $J_{sc} = 15.6 \text{ mA cm}^{-2}$, $V_{oc} = 558 \text{ mV}$, FF = 0.65) in association with a low-volatile electrolyte based on MPN (Table 1 entry 12).^[59]

Squaraine dyes particularly suffer from a photoisomerization process involving *cis*- and *trans*-configurations, limiting their cell efficiency.^[60] The first strategy to address this issue is adding a second anchoring moiety^[56] that provides a stronger electronic coupling with the semiconductor surface and greater stability. This also contributes to a slight bathochromic shift even though not sufficient to reach the NIR region. A second approach is the insertion of long alkyl chains on the lateral substituents^[58] that increases the steric hindrance, thus preventing intramolecular rotation. Another approach is the functionalization of the squaric core unit to lock the structure into the *cis*-configuration.^[61]

The addition of electron-withdrawing groups on the core unit induces a bathochromic shift of the maximum absorption of about 50 nm and the occurrence of a second absorption band at higher energies. These observations were made on a diethylthiobarbituric moiety^[58] and a dicyanovinyl group leading to a 30% increase in PCE.^[17] A greater bathochromic shift can be achieved with a cyano-ester moiety.^[59] Galliano et al. designed a series of squaraine dyes combining all these features to obtain a photoconversion onset that reaches 51% maximum IPCE at 740 nm with a tail of conversion up to 800 nm for the VG12-C8 dye bearing a cyano-ester group on the squaraine central core and two benzoindolenine units.^[61] However, an important drawback for TPV application with the central functionalization is the occurrence of an absorption band in the visible region, thus limiting their use for transparent DSSCs substantially.

Cyanine Dyes: Cyanine dyes belong to the polymethine class that possesses several key characteristics for their application in NIR-DSSCs. Their tunability to shift the absorption maximum with the introduction of the vinylene moiety ($-\text{CH}=\text{CH}-$) made them an interesting molecular platform for the purpose of NIR-DSSCs.

The first cyanine dye for DSSC was limited to the conversion of light in the visible region. It yielded low PCE values inferior to 1%.^[62] Soon after, different studies were taking advantage of these dyes to absorb in the NIR region to maximize

Table 1. Photovoltaic performance and squaraine dyes in NIR-DSSC.

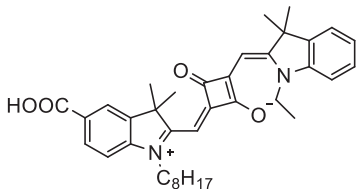
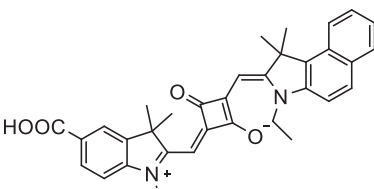
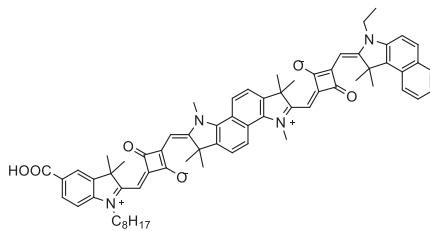
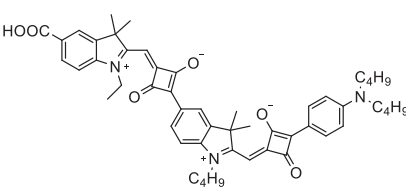
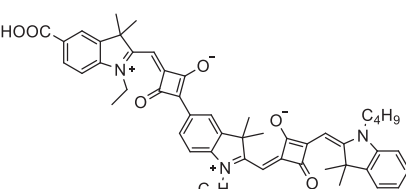
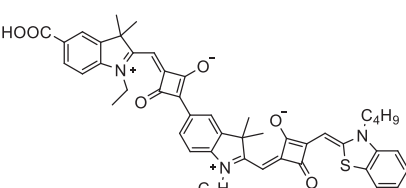
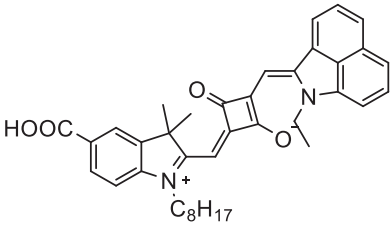
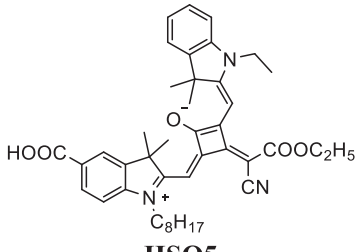
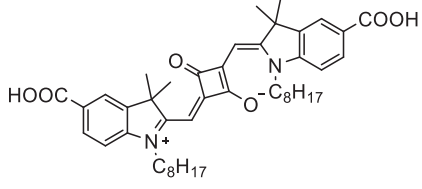
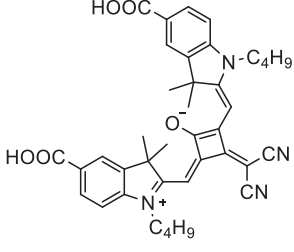
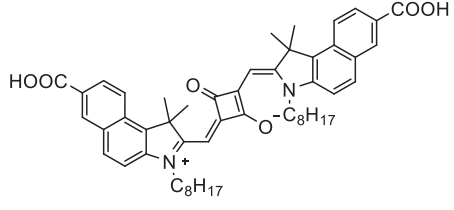
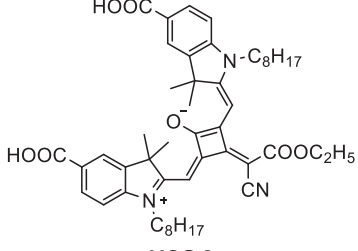
Entry	Dye	λ_{MAX} [nm] ϵ [$\text{M}^{-1} \text{cm}^{-1}$]	J_{SC} [mA cm^{-2}]	V_{OC} [mV]	FF	PCE [%]	Refs.
1	 SQ01	$647\,292 \times 10^3$ (DMF)	10.5	603	0.71	4.5	[49]
2	 SQ02	$662\,319 \times 10^3$ (DMF)	11.3	667	0.72	5.4	[50]
3	 BSQ01	$730\,389 \times 10^3$ (DMF)	3.11	545	0.76	1.3	[51]
4	 LSQa	$777\,174 \times 10^3$ (CHCl_3)	9.05	460	0.54	2.26	[52]
5	 LSQb	$779\,180 \times 10^3$ (CHCl_3)	8.64	410	0.57	2.01	[52]
6	 LSQc	$800\,189 \times 10^3$ (CHCl_3)	9.01	400	0.51	1.82	[52]

Table 1. Continued.

Entry	Dye	λ_{MAX} [nm] ϵ [$\text{M}^{-1} \text{cm}^{-1}$]	J_{SC} [mA cm^{-2}]	V_{OC} [mV]	FF	PCE [%]	Refs.
7	 VG5	769 n/a (EtOH)	7.29	350	0.43	1.10	[54]
8	 HSQ5	$693\ 178 \times 10^3$ (DMF)	5.47	603	0.70	2.30	[23]
9	 VG1	$646\ 350 \times 10^3$ (EtOH)	9.4	629	0.77	4.6	[56]
10	 SQM1a	$705\ 158 \times 10^3$ (CHCl_3)	14.2	500	0.51	3.6	[57]
11	 VG10	$673\ 300 \times 10^3$ (EtOH)	14.3	623	0.69	6.2	[58]
12	 HSQ4	$703\ 137 \times 10^3$ (DMF)	15.6	558	0.65	5.7	[59]

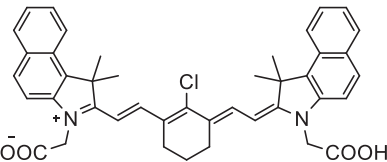
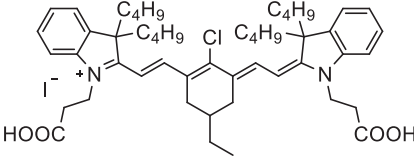
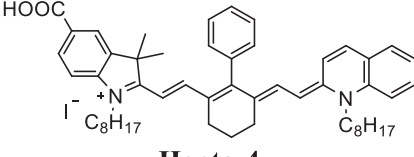
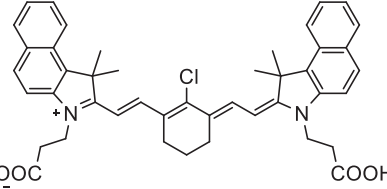
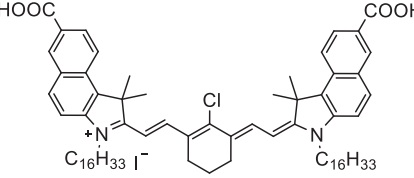
the harvesting capability of DSSC by cosensitization^[63,64] or to explore selective NIR-DSSC.^[65]

Sayama et al. synthesized a series of cyanine dyes, Cyn, for which the absorption maximum was red-shifted from 443, 555, to 660 nm by increasing the number of vinylene units from 0 to 2, with the latter achieving the best performance with a PCE of 2.5% and an IPCE maximum of 50% up to 600 nm.^[66] One of the most efficient NIR dyes is the cyanine NK-6037 reported by Arakawa et al. in 2009, achieving a PCE of 2.3% ($J_{sc} = 8.85 \text{ mA cm}^{-2}$, $V_{oc} = 450 \text{ mV}$, $FF = 0.58$) (Table 2 entry 1).^[65] The introduction of the benzo-condensed heteroaromatic unit in the polymethine chain leads to a shift in the absorption over 800 nm. When associated with an unusually thick photoanode (i.e., >25 μm), they reported an IPCE of over 50% at 840 nm with a tail extending up to ca. 950 nm. Later Matsui et al. proposed another cyanine dye associated with ZnO photoanode.^[67] This dye, coded KFH-3 ($\lambda = 787 \text{ nm}$ and $\epsilon = 263000 \text{ M}^{-1} \text{ cm}^{-1}$),

was synthesized with an ethyl group in *para* position of the chloro-cyclohexene (Table 2 entry 2). The authors achieved an overall 1.2% PCE ($J_{sc} = 3.34 \text{ mA cm}^{-2}$, $V_{oc} = 490 \text{ mV}$, $FF = 0.76$) for a 7 μm thick TiO_2 electrode and an IPCE maximum of 33% at ca. 790 nm.

A comparison between symmetrical and unsymmetrical cyanine dyes was investigated by Nüesch et al. They showed that, similarly to squaraines, the symmetrical cyanine offers a red-shifted absorption and the highest molar extinction coefficients.^[68] The dye Hepta4 of the aforementioned series is designed as a polymethine core rigidified by a cyclohexene moiety and one anchoring carboxylic group terminating the benzoindolenine (Table 2 entry 3). The dye reached an absorption maximum at 758 nm ($\epsilon = 82\,500 \text{ M}^{-1} \text{ cm}^{-1}$) and a PCE of 1.2% ($J_{sc} = 3.22 \text{ mA cm}^{-2}$, $V_{oc} = 480 \text{ mV}$, $FF = 0.78$). In 2015, Ziolk et al. discussed the challenges of using NIR cyanine-based DSSC through ultrafast transient absorption

Table 2. Photovoltaic performance and cyanine dyes in NIR-DSSC.

Entry	Dye	λ_{MAX} [nm]	ϵ [$\text{M}^{-1} \text{ cm}^{-1}$]	J_{sc} [mA cm^{-2}]	V_{oc} [mV]	FF	PCE [%]	Refs.
1	 NK6037	822	146×10^3 (EtOH)	8.85	450	0.58	2.3	[65]
2	 KFH-3	787	263×10^3 (MeOH)	3.34	490	0.76	1.2	[67]
3	 Hepta-4	758	82.5×10^3 (EtOH)	3.22	480	0.78	1.2	[68]
4	 MK-245	824	146×10^3 (EtOH)	2.51	375	0.49	0.46	[30]
5	 VG20-C16	834	154×10^3 (EtOH)	11.2	422	0.65	3.1	[25]

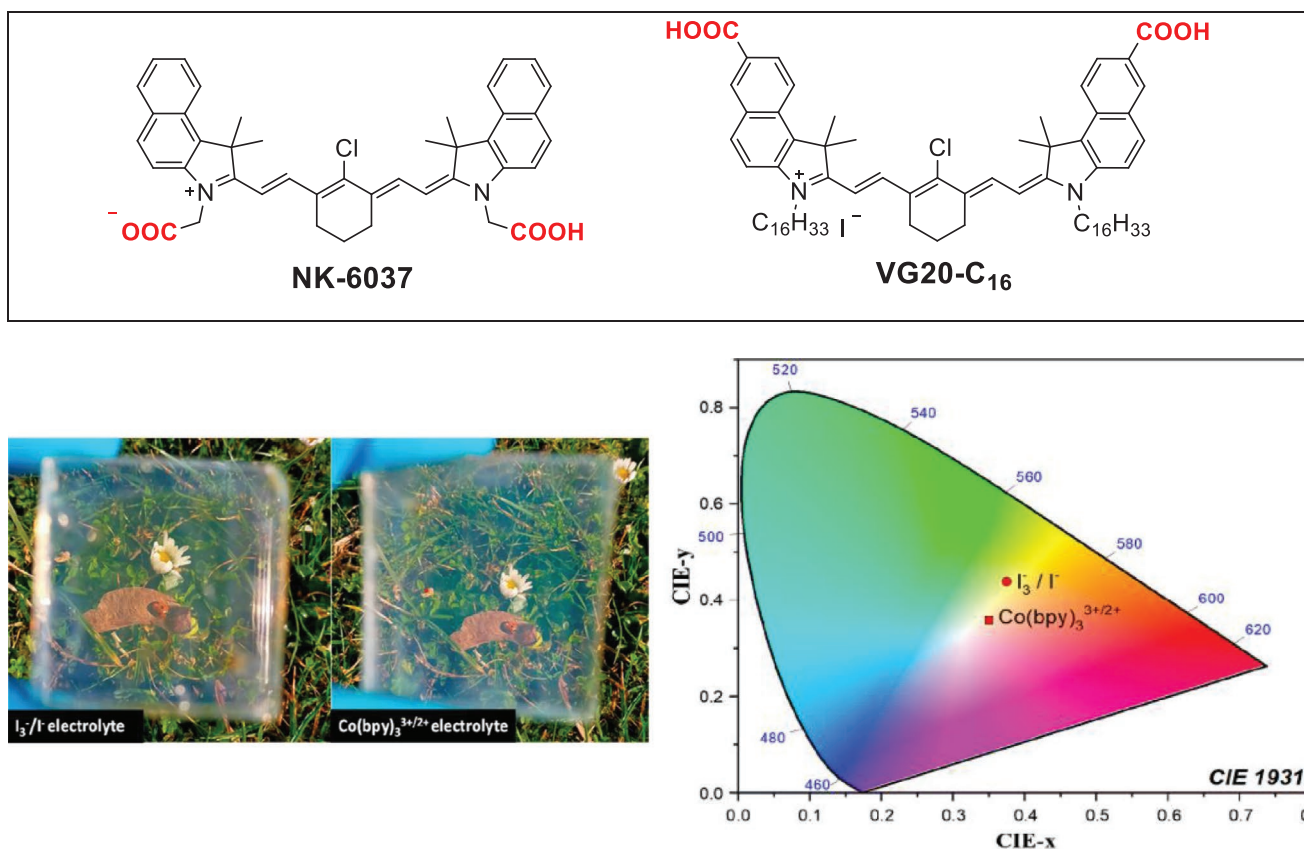


Figure 4. Comparison between the NK-6037 and VG20 structures. Two pictures of transparent NIR-DSSC with VG20-C₁₆ and I₃⁻/I⁻ redox couple and Co(bpy)^{3+/2+} (bottom left) and CIE 1931 color space diagram of the resulting NIR-DSSC (bottom right). Reproduced with permission.^[25] Copyright 2021, American Chemical Society.

spectroscopy. His work provides a first explanation on the rather low PCE systematically obtained based on the strong tendency for dye aggregation. They investigated MK-245 dye, whose structure is closely related to NK-6037, however without being as efficient (PCE = 0.46%, $J_{sc} = 2.51 \text{ mA cm}^{-2}$, $V_{oc} = 375 \text{ mV}$, FF = 0.49) (Table 2 entry 4, Figure 4).^[30]

The highest power conversion efficiency under AM 1.5G conditions reported so far is VG20-C₁₆ dye reaching 3.1% PCE (Table 2 entry 5, Figure 4).^[25] Its absorption lies perfectly outside the human eyes photopic response. As a result, a maximum of AVT of 76% has been reported and a CRI value above 94%, which constitutes today the best characteristics obtained so far for selective NIR-DSSC and the first proof of concept of a totally transparent and colorless DSSC for TPV applications.

3.1.2. Phthalocyanine

Phthalocyanines are 2D tetrapyrrolic macroheterocycles containing 18 delocalized p-electrons that exhibit absorption maxima in the red/near-infrared (NIR) region (blue pigment). Their high molar extinction coefficient and their thermal and chemical stability make this type of dyes suitable for DSSC application.^[69,70] The optical and electronic properties can be adjusted by structural engineering of the Pc macrocycle, that is, the metal center, the peripheral, nonperipheral, and axial substitution, which

allows, in particular, to tune their redox potential and extend/shift their absorption toward the NIR region. Nevertheless, this class of dyes holds two important issues in the field of DSSC, their strong tendency to aggregate and their relatively low solubility. Phthalocyanines were introduced to DSSC technology in 1995 by Shen et al.^[71] Soon after, this class of dyes has grasped rapid interest for photovoltaic applications because of their appealing optical characteristics and, in particular, to harvest light in the red/NIR regions of the solar spectrum. In 1999, Nazeruddin et al. pioneered the utilization of a symmetrically substituted phthalocyanine (ZnTcPc) as a promising blue dye for efficient and stable DSSC, which achieved an overall power conversion efficiency of 1% with a remarkable IPCE of 43% ($J_{sc} = 5.4 \text{ mA cm}^{-2}$, $V_{oc} = 416 \text{ mV}$, FF = 0.45) (Table 3 entry 1).^[72] In the same work, they also examined the differences between symmetrically and nonsymmetrically substituted phthalocyanines. With the latter, the authors pointed out the advantages of developing unsymmetrically substituted Pcs in order to obtain a “push-pull” structure that improves the directionality of intramolecular charge transfer processes and injection into TiO₂ nanocrystals. In addition, the introduction of bulky groups in the periphery of the Pc (such as *tert*-butyl) is essential to improve the solubility of the dye and helps to limit aggregation. Following this concept, sensitizers TT1^[73] and PCH001^[74] were reported in 2007 with PCE above 3% (Table 3 entry 2 and 3) and an IPCE reaching 75% at 700 nm (PCE = 3.5% $J_{sc} = 7.6 \text{ mA cm}^{-2}$,

Table 3. Photovoltaic performances of phthalocyanine dyes towards NIR-DSSC.

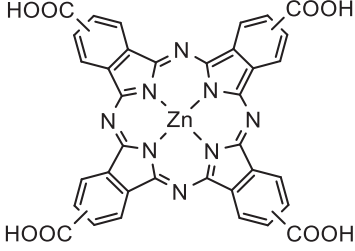
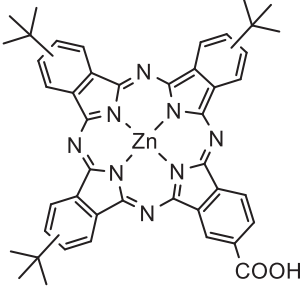
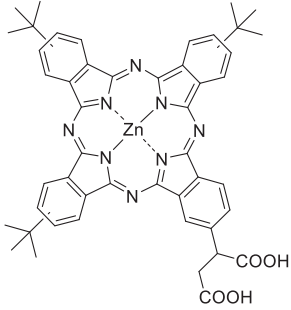
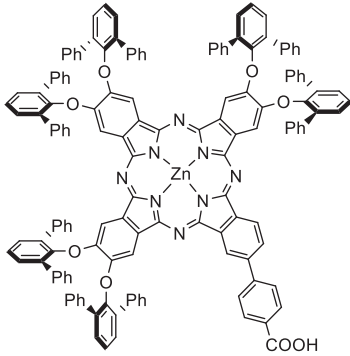
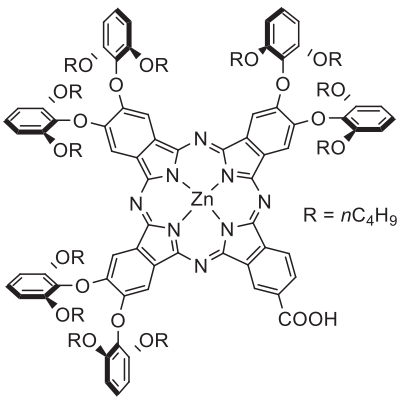
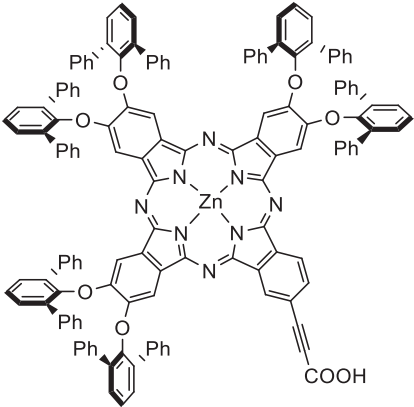
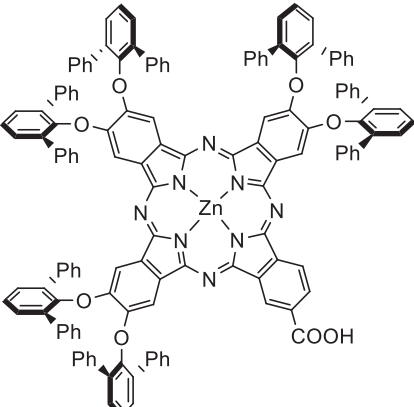
Entry	Dye	λ_{MAX} [nm] ϵ [$\text{M}^{-1} \text{cm}^{-1}$]	J_{SC} [mA cm^{-2}]	V_{OC} [mV]	FF	PCE [%]	Refs.
1	 <p>ZnTcPc</p>	686 33 $\times 10^3$ (EtOH)	5.4	416	0.45	1.0	[72]
2	 <p>TT1</p>	680 160 $\times 10^3$ 606 32 $\times 10^3$ 350 80 $\times 10^3$ (THF)	7.6	617	0.75	3.5	[73]
3	 <p>PCH001</p>	692 191 $\times 10^3$ (EtOH)	6.5	635	0.74	3.05	[74]
4	 <p>PcS6</p>	684 81.3 $\times 10^3$ (THF)	10.4	630	70	4.6	[75]

Table 3. Continued.

Entry	Dye	λ_{MAX} [nm] ϵ [$\text{M}^{-1} \text{cm}^{-1}$]	J_{SC} [mA cm^{-2}]	V_{OC} [mV]	FF	PCE [%]	Refs.
5	 <p>PcS20</p>	$695.93.3 \times 10^3$ $675.87.1 \times 10^3$ $642.21.4 \times 10^3$ $613.20.4 \times 10^3$ $359.46.8 \times 10^3$ (Toluene)	15.1	600	0.71	6.4	[80]
6	 <p>TT40</p>	$698.89.1 \times 10^3$ $675.81.3 \times 10^3$ $639.18.6 \times 10^3$ $612.17.4 \times 10^3$ $361.51.3 \times 10^3$ $296.26.9 \times 10^3$ (THF)	12.3 ^[81] 13.9 ^[82]	638 ^[81] 621 ^[81]	0.70 ^[81] 0.70 ^[81]	5.50 ^[81] 6.01 ^[81]	[81]
7	 <p>TT58</p>	692.138×10^3 676.132×10^3 $639.22.9 \times 10^3$ $612.27.5 \times 10^3$ $361.70.1 \times 10^3$ (THF)	12.8	618	0.69	5.5	[82]

$V_{\text{oc}} = 617$ mV, FF = 0.75 for TT1 and PCE = 3.1% $J_{\text{sc}} = 6.5$ mA cm^{-2} , $V_{\text{oc}} = 635$ mV, FF = 0.74 for PCH001). However, these macrocycles still display aggregation, despite the presence of *tert*-butyl groups in their periphery, which have limited for a long time to improve further the performances of Pc-based dyes in DSSC, since aggregation degrades their electron injection efficiency drastically. In fact, it is necessary to use a large excess of coadsorbent (typically CDCA) to decrease aggregation level

and thus to reach optimal performances of these dyes in DSSC (ratio dye / CDCA of 1:100–1:2000). This constitutes the main drawback because it limits the total amount of Pc molecules that can be chemisorbed on the semiconductor's surface, hence the J_{sc} .

To tackle this issue a breakthrough stemmed in 2010 from the group of Kimura, who introduced 2,6-diphenylphenoxy groups at the peripheral positions of the Pc (PcS6; Table 3 entry 4).^[75]

The PCE raised over 4% for a Pc dye for the first time, with a 4.6% value obtained with PcS6, which is considerably higher than the 2.6% value obtained for the *tert*-butyl peripherally-substituted analog (PcS2) studied in the same work ($J_{sc} = 10.4 \text{ mA cm}^{-2}$, $V_{oc} = 630 \text{ mV}$, $FF = 0.70$). The diphenylphenoxy moieties completely suppress aggregation of the Pc molecules and, indeed, no- or very low amount of CDCA was necessary to reach optimal performance for this new family of dyes. In addition, the presence of heteroatom donating groups (oxygen) directly linked to the Pc macrocycle is also known to be beneficial in terms of better optical and energetic properties.^[76] In particular, it produces a further intensification of the “push-pull” effect and an appreciable red-shift of the Q-band absorption, which, together with the suppression of aggregation, are responsible for the considerable improvement in performances. This led to the development of the PcS dyes family^[77–80] with constant improvement in performances over the years, to reach a maximum PCE of 6.4% with PcS20, peripherally-substituted with 2,6-dibutoxyphenols and a carboxyl group as the acceptor/anchor unit ($J_{sc} = 15.1 \text{ mA cm}^{-2}$, $V_{oc} = 600 \text{ mV}$, $FF = 0.71$) (Table 3 entry 5).^[80]

At the same time, Nazeeruddin and Torres’s groups reported a sterically hindered Pc dye, TT40 (Table 3 entry 6), substituted at the periphery with six bulky 2,6-diphenylphenoxy groups, achieving a PCE of 5.5% and with an IPCE greater than 85% at 700 nm ($J_{sc} = 12.3 \text{ mA cm}^{-2}$, $V_{oc} = 638 \text{ mV}$, $FF = 0.70$).^[81] Noteworthy, TT40 gave higher PCE value than PcS6 previously reported by Mori’s group (5.5% vs 4.6%). TT40 and PcS6 have the same peripheral substitution from the structural point of view but differ from the acceptor/anchor part, a carboxyethynyl and carboxyphenyl group, respectively. The authors revealed the important contribution of the ethynyl moiety as a bridge, which is beneficial for optimal electronic coupling between the Zn^{II} Pc and TiO_2 . In further work, the same authors reported an analog dye, TT58, with the same peripheral substitution as its predecessor TT40, but with a direct connection between the carboxyl group and the Pc macrocycle (Table 3 entry 7).^[82] TT58 reached a PCE of 5.6% (6.05% under 0.1 sun) with an IPCE greater than 90% at 700 nm, the latter being so far the highest value ever reported for a Pc dye ($J_{sc} = 12.8 \text{ mA cm}^{-2}$, $V_{oc} = 618 \text{ mV}$, $FF = 0.69$). In this new work, the previous dye TT40 was also further optimized to a 6.0% PCE ($J_{sc} = 13.9 \text{ mA cm}^{-2}$, $V_{oc} = 621 \text{ mV}$, $FF = 0.70$). Although the new Pc TT58 underperformed slightly TT40 under the same optimized condition (5.57% vs 6.01%), the excellent performance of this dye suggests, contrary to what had previously been claimed, that the bulkiness of the diphenylphenoxy moieties does not exert a critical influence on the adsorption capabilities of this family of compounds, regardless of the distance between the Pc core and the carboxyl group. This family of dyes demonstrated already strong absorption and conversion in the red part of the solar spectrum; however, it still requires a substantial amount of work in order to bring the absorption beyond 800 nm, a threshold ensuring colorless features.

3.1.3. Porphyrins

Porphyrins (Pors) are tetrapyrrolic macroheterocycles containing 18 delocalized p-electrons macroheterocycle, synthetic

analogues of Pcs, and distinguished by a strong absorption in the visible region with a high molar extinction coefficient and tunable redox properties. Their thermal and chemical stability is quite high, although lower when compared to Pc. On the counterpart, Pors tend to aggregate much less than Pcs, which is a major advantage for NIR-DSSC to ensure high performance on the one hand and colorless features on the other hand. As well, structural engineering throughout the metal center, axial substituents, the four *meso*- and eight *b*-positions offers a very large panel to tune their redox potential and electronic properties.

Given that the great majority of porphyrins usually display most of their absorption in the visible region at ca. 400–600 nm, they have not been considered as real NIR-sensitizers for DSSCs until now. However, by proper structural engineering, several porphyrins with extended absorption toward the red/NIR regions have been reported in the past years. In fact, this has been the key success for the most efficient porphyrin dyes reported in DSSC to date.^[83] In particular, the “push-pull” porphyrin dyes SM315^[84] and GY50^[85] reported by Grätzel group’s and collaborators, display extended absorption up to ca. 800 nm, thanks to the incorporation of the proquinoidal benzothia-diazole (BTD) unit directly connected to one *meso* position, and a donor amine N-linked to the macrocycle on the other *meso* side (Table 4 entry 1 and 2). SM315 reaches high IPCE values across the whole visible wavelength range (80% from 450 to 750 nm) and extends up to 800 nm. The extension of absorption of these porphyrins toward the red and NIR regions of the solar spectrum while maintaining high IPCE values greatly contributed to the successive improvement in performances over the years with respect to the former generation of porphyrin dyes (i.e.: YD2^[86] and YD2-0-C8^[87]). SM315 and GY50 achieved record efficiency of ca. 13% in DSSC, which stand one of the highest certified values ever reported in DSSC for a single dye (PCE = 13.0% $J_{sc} = 18.1 \text{ mA cm}^{-2}$, $V_{oc} = 910 \text{ mV}$, $FF = 0.78$ for SM375 and PCE = 12.8% $J_{sc} = 18.5 \text{ mA cm}^{-2}$, $V_{oc} = 885 \text{ mV}$, $FF = 0.77$ for GY50).

In a different strategy, Luo et al. used an N-annulated perylene (NP) as an efficient electron donor, fused (WW4) or nonfused (WW5), to the push-pull structure of the porphyrin (Table 4 entry 3 and 4).^[88] Thanks to the improved π -conjugation of the porphyrin macrocycle through the carbon rich-structure of the NP moiety, these dyes exhibit red-shifted absorption spectra with remarkably intense near-IR absorption, in particular for the fused one (WW4), which is extended up to 920 nm with maxima at 792 nm ($\epsilon = 75.4 \times 10^3 \text{ M}^{-1} \text{ cm}^{-1}$), and more modest for the nonfused analog WW5 with a maximum at 679 nm ($\epsilon = 75.4 \times 10^3 \text{ M}^{-1} \text{ cm}^{-1}$). Although WW4 showed the best light-harvesting ability with intense absorption in the NIR region, this dye achieved a poor PCE of 0.3% ($J_{sc} = 3.0 \text{ mA cm}^{-2}$, $V_{oc} = 500 \text{ mV}$, $FF = 0.30$), in stark contrast with the non-fused analog WW5 that reached a value of 10.3% ($J_{sc} = 18.4 \text{ mA cm}^{-2}$, $V_{oc} = 766 \text{ mV}$, $FF = 0.73$). The poor performances of WW4 were rationalized by the mismatch of its energetics levels, namely a too low-lying HOMO and non-disjointed HOMO/LUMO profiles, which leads to an insufficient driving force for electron injection. This last example illustrates that the extension to the red and NIR features of a porphyrin dye through structural changes must be carefully engineered and is not necessarily (and in fact not often) accompanied by a net gain in performances

Table 4. Photovoltaic performance and porphyrin dyes towards NIR-DSSC.

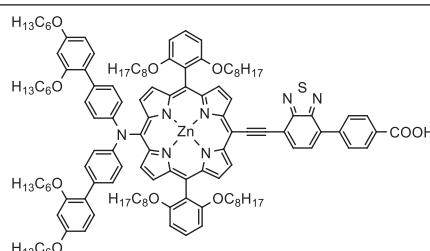
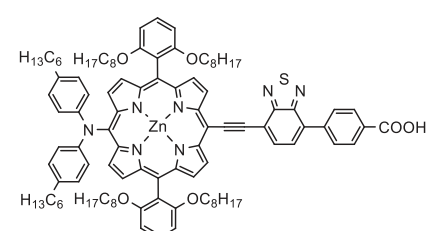
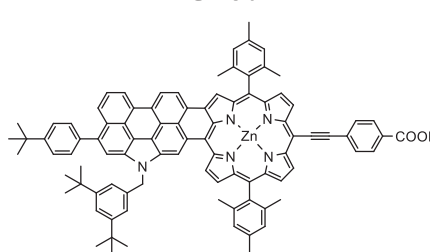
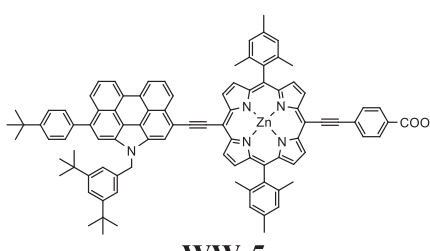
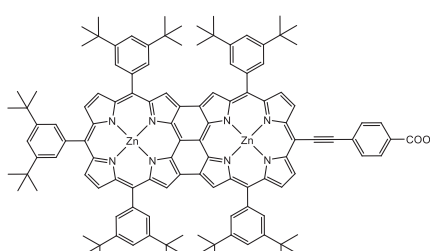
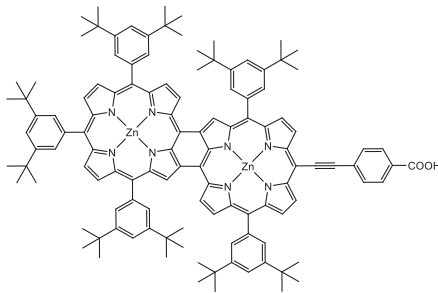
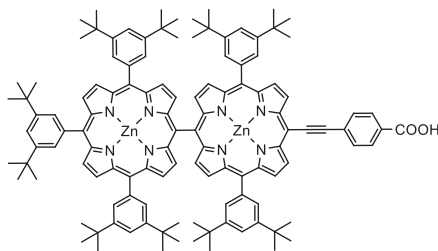
Entry	Dye	λ_{MAX} [nm] ϵ [$\text{M}^{-1} \text{cm}^{-1}$]	J_{SC} [mA cm^{-2}]	V_{OC} [mV]	FF	PCE [%]	Refs.
1	 <p>SM315</p>	$440\ 105 \times 10^3$ $454\ 117 \times 10^3$ $581\ 12 \times 10^3$ $668\ 53 \times 10^3$ (THF)	18.1	910	0.78	13.0	[84]
2	 <p>GY50</p>	$453\ 119 \times 10^3$ $538\ 11 \times 10^3$ $665\ 53 \times 10^3$ (THF)	18.53	885	0.773	12.75	[85]
3	 <p>WW-4</p>	$444\ 552 \times 10^3$ $540\ 69.9 \times 10^3$ $792\ 75.4 \times 10^3$ (DCM)	3.00	500	0.299	0.3	[88]
4	 <p>WW-5</p>	$441\ 158.5 \times 10^3$ $446\ 115.3 \times 10^3$ $502\ 61.5 \times 10^3$ $679\ 75.4 \times 10^3$ (DCM)	18.43	766	0.733	10.3	[88]
5	 <p>YDD2</p>	$437\ 116 \times 10^3$ $492\ 68 \times 10^3$ $580\ 167 \times 10^3$ $1011\ 26 \times 10^3$ $1169\ 59 \times 10^3$ (DCM / pyridine 100:1)	<0.5	400	n/a	< 0.5	[89]

Table 4. Continued.

Entry	Dye	λ_{MAX} [nm] ϵ [$\text{M}^{-1} \text{cm}^{-1}$]	J_{SC} [mA cm^{-2}]	V_{OC} [mV]	FF	PCE [%]	Refs.
6		442 165 $\times 10^3$ 505 90 $\times 10^3$ 579 84 $\times 10^3$ 617 48 $\times 10^3$ 665 28 $\times 10^3$ 756 27 $\times 10^3$ 845 102 $\times 10^3$ (DCM/ pyridine 100:1)	<0.5	460	n/a	< 0.5	[89]
7		429 186 $\times 10^3$ 445 199 $\times 10^3$ 490 265 $\times 10^3$ 547 20 $\times 10^3$ 753 77 $\times 10^3$ (DCM/ pyridine 100:1)	9.23	605	0.73	4.1%	[89]

for DSSC applications. Along the same lines, other interesting examples are the fused (YDD3) and doubly fused (YDD2) porphyrin dimers reported by Diau and co-workers (Table 4 entry 5 and 6).^[89] The fusion between the two macrocycles allows a full conjugation over the two coplanar porphyrin structures, which is not possible for the nonfused analog (YDD0) (Table 4 entry 7). These dimers possess improved and very appealing optical features, with intense and broad absorption in the entire visible spectrum and remarkably intense near-IR absorption for both fused dimers. In the NIR region, YDD3 displays intense absorption bands with maxima 756 and 845 nm, whereas those of YDD2 are much wider but range from 900 to 1300 nm. However, both YDD2 and YDD3 exhibit poor cell performance with negligible generated photocurrent (0.12 and 0.23 mA cm^{-2} , respectively), which is again in sharp contrast with the non-fused analog YDD0 that displays great performances with a high J_{SC} value of 9.2 mA cm^{-2} and an overall PCE of 5.2%. In other words, YDD2 and YDD3 are not capable of photoinjecting electrons in the TiO_2 . Once again, this is rationalized by the mismatch of their energetic levels, a too low-lying LUMO with respect to the TiO_2 -CB, making the electron-injection process noneffective. Although important synthetic efforts afforded significant to progress in the porphyrin class of dyes by reaching the NIR conversion, still selective NIR absorption remains to be demonstrated through molecular engineering.

To conclude for this section, many classes of dyes have been investigated and dye engineering has afforded to develop DSSC panels with a variety of colors with very good level of performances. However, in the case of NIR-DSSC, the choice of sensitizers becomes limited to few classes. In the current state of the art, the most interesting family from an optical point of view remains the polymethine dyes. Particularly interesting seem to be cyanine dyes due to their absorption spectrum's tunability, thanks to which is possible to obtain weak absorption in the

visible while having a sharp and strong absorption in the NIR region (Figure 5). In analogy to many dyes, one crucial limitation is the formation of aggregates, penalizing both performances and aesthetics. Femtosecond transient absorption spectroscopy clearly assigned that the performance limitation with cyanine dyes stems from three competitive paths, i.e., energy transfer from monomer to aggregates, radiative decay of the short-lived excited states versus monomer injection.^[25,30] All three steps are in the same range of halftime.

This issue can be partially mitigated either by introducing a long lateral alkyl chain, via a bulky lateral unit or by adding deaggregating agent into the dye solution such as the conventional chenodeoxycholic acid (CDCA).^[25,90]

The small driving force limits the electron injection. For VG20-C₁₆ dye, this was overcome by adding a high concentration of potential determining Li⁺ cation in the electrolyte and by removing *tert*-butylpyridine and guanidinium cations from the electrolyte. It leads to an increase of short-circuit current density from 5.5 to 12.1 mA cm^{-2} and injection yield ϕ_{inj} up to 35%. On the contrary, in the case of squaraine dyes, it is reported that despite the small driving force for injection ($-\Delta G_{\text{inj}}^{\circ}$ of 0.15 eV for SQ26 and 0.45 eV for SQ41) similar k_{inj} ($6.7 \times 10^{11} \text{ s}^{-1}$ and $7.7 \times 10^{11} \text{ s}^{-1}$ respectively) are found on account of the strong electronic coupling.^[90] Consequently, the addition of Li⁺ is not as fundamental and may even affect the level of molecular aggregation as it has been already demonstrated with VG1 dye.^[91]

Other than polymethine dyes, we have also proposed PcS and Pors in this section. At the current state of the art, a NIR-DSSC based on these dyes may not be as colorless and transparent as the polymethine ones, due to absorption residuals in the visible range with a high molar extinction coefficient. This is particularly visible for Pors as shown in Figure 5. However, their high thermal and chemical stability makes them suitable for the application in building integration. Furthermore, many

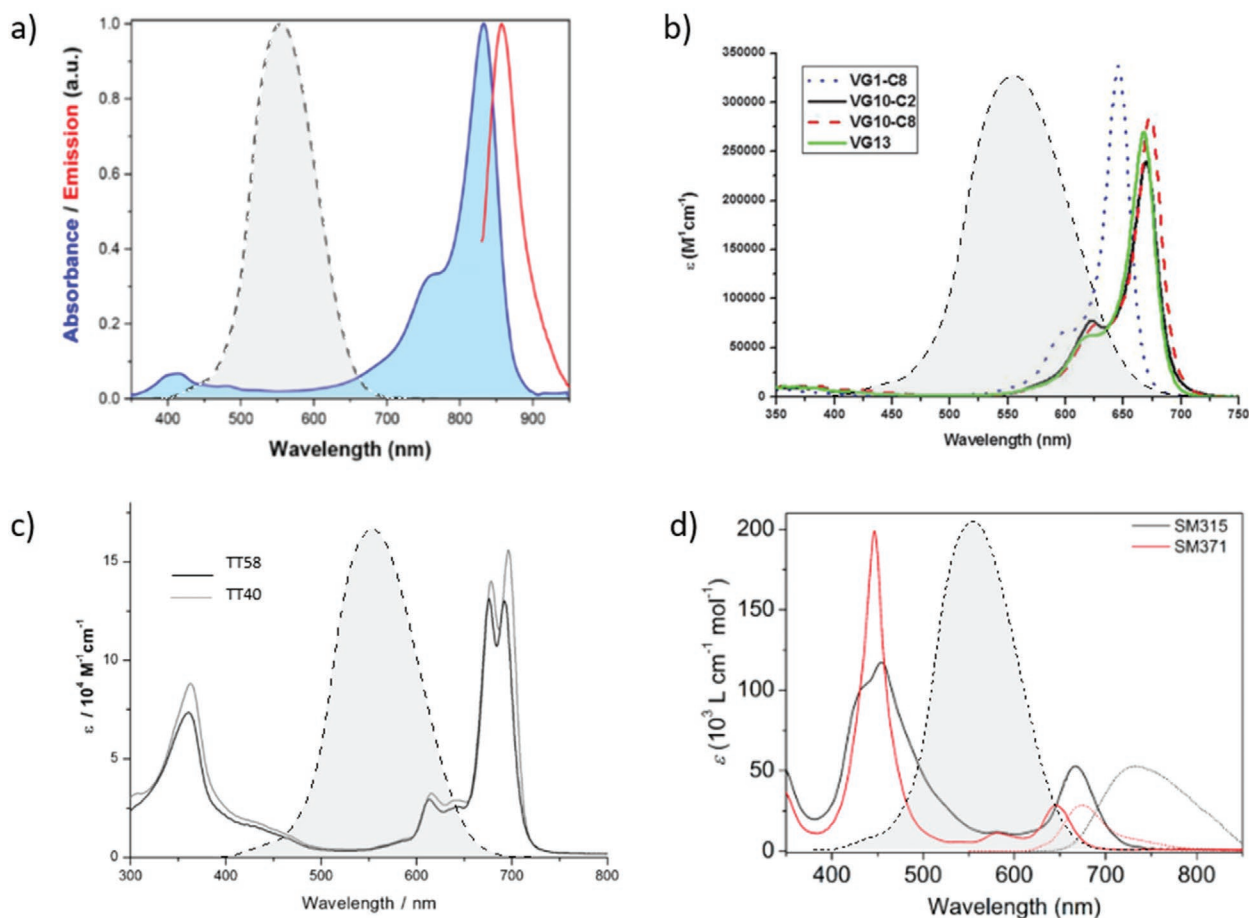


Figure 5. a) Normalized UV–vis absorption spectrum of VG20-C16 in solution (blue curve) and steady-state photoluminescence (red curve) in 9/1 (v/v) ethanol/DMSO solvent mixture (dye concentration $100 \mu\text{mol L}^{-1}$, CDCA concentration 50mmol L^{-1}). Reproduced with permission.^[25] Copyright 2021, American Chemical Society. b) Absorption spectra of VG10-C2 (solid black line), VG10-C8 (dashed red line), VG13 (solid green line) and VG1-C8 (dotted blue line) in ethanol. Reproduced with permission.^[58] Copyright 2014, Royal Society of Chemistry. c) UV/Vis spectra in THF of TT58 (black line) and TT40 (gray line). Reproduced with permission.^[84] Copyright 2014, Springer Nature. d) Absorption (solid line) and normalized emission ($\lambda_{\text{ex}} = 440 \text{nm}$ dashed line) spectra for SM371 (red) in THF solution. Reproduced with permission.^[84] Copyright 2014, Springer Nature. The photopic response of the human eye is represented as a gray area for comparison in all graphs. All figures are Reproduced with permission.

efforts have already been made in terms of dye engineering, paving the way for new opportunities, particularly in the case of Pors, for which the aggregation issue also seems to be an important limitation compared to the other classes of dyes.

3.2. Fully Transparent Photoanode

Reducing the amount of internal energy losses requires minimizing the driving force for electron injection, thus calling for the most efficient electronic coupling between the dye excited states and the large bandgap semi-conductor. However, in addition to this important feature that will impact on the power conversion efficiency, the technology's particular benefit stems from aesthetic aspects in terms of transparency and coloration. For this, not only having a dye free of absorption bands in the visible range is needed to ensure no coloration features, but it also calls for a large bandgap semiconductor greater than 3.0 eV and nanocrystals free of aggregates to avoid light scattering accordingly to Mie-scattering theory which would be detrimental for the AVT value.

Typically, the photoanode is based on a mesoporous layer made of anatase TiO_2 nanoparticles (NPs) with thicknesses in the range of few micrometers. However, different alternatives have been explored such as ZnO ,^[92–94] SnO_2 ,^[95–97] Nb_2O_5 ,^[98] brookite and B form of TiO_2 ^[99,100] or ternary metal oxides such as the spinel Zn_2SnO_4 ^[101,102] or the perovskite SrTiO_3 ^[103] (Figure 6). The most used is anatase titania due to its high chemical stability, low cost, low toxicity and versatile ways of synthesis.^[104–108] Furthermore, because of its large bandgap of 3.2 eV, it is characterized by high transparency in the visible and NIR-spectral range. Figure 6 presents both valence band (VB) and conduction band (CB) edges position of different metal-oxide semiconductors already used in DSSC. The potential positions are extracted from the literature for a $\text{pH} \approx 1$. For most NIR dyes, the LUMO level is very close to the semiconductors CB edge, therefore strongly limiting electron injection kinetic.

In the case of the NIR-DSSC, the AVT is an additional metric to consider for the photo-anode optimization. Indeed, increasing excessively the electrode's thickness will affect the device AVT, thus the aesthetic rendering.

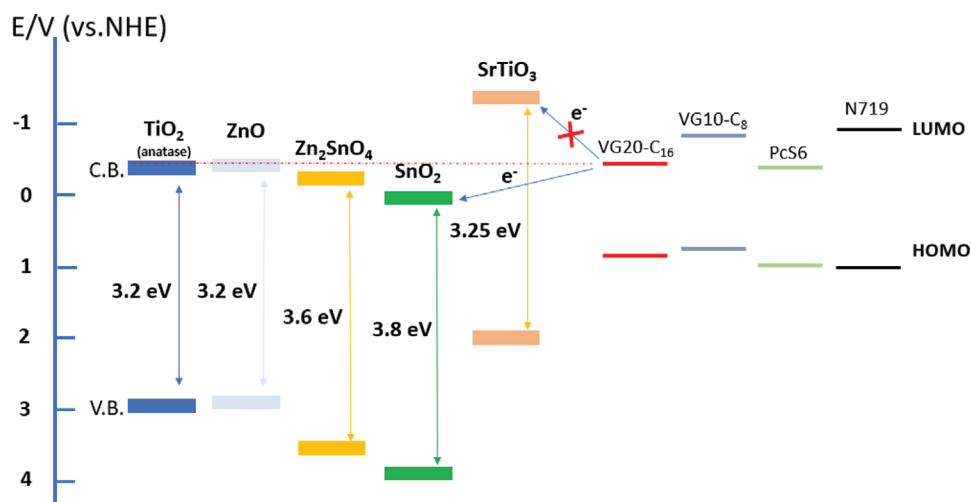


Figure 6. Valence band (VB) and conduction band (CB) position of different metal-oxide semiconductors used in DSSC, compared with HOMO and LUMO levels of commonly used N719 dye and NIR-absorbing dyes.

A careful control in the CB edge position, to which the design of a NIR dye is bounded, can be achieved through low levels of donor aliovalent doping. Indeed, the $3d^0$ electronic configuration of the Ti^{4+} confers a high sensitiveness to impurities and doping that will affect the optoelectronic characteristics of TiO_2 . A broad range of dopants has been explored in the literature,^[109,110] but not all meet the criteria for NIR-DSSC applications as the CB varies its position depending on the dopant nature. Consequently, TiO_2 's optical bandgap and electron injection rate can be affected.

Various authors reported that doping with Cr^{3+} ,^[111] or hypervalent cations such as Nb^{5+} ,^[112,113] V^{5+} ,^[114] W^{6+} ,^[115–117] or Ta^{5+} ^[118] is the most promising approach to decrease the CB position by few tens of mV. Generally, the introduction of hypervalent cation into the anatase crystal structure creates donor levels and shallow traps below the CB, which can favor the electron injection in the particular case where the lack of driving force limits the injection yield. The dopant is introduced either in substitution of the Ti^{4+} when ionic radii are comparable or is positioned in interstitial sites, thus generating excess oxygen stoichiometry as charge compensation mechanism. As demonstrated by Chandiran et al., Nb^{5+} doping of anatase TiO_2 is a successful mean to increase the photoanode transparency by 5–10% as a result of the Burstein-Moss effect.^[112] However, care has to be exercised since a too high level of doping will create an excessive amount of deep traps which will affect the charge collection efficiency. Following this, they have highlighted both a gain in PCE and transparency in the visible range for the photoanode by doping TiO_2 with Nb^{5+} from 0.5 to 2 mol%. On semitransparent DSSC based on ruthenium polypyridyl C101 dye, they achieved a PCE increase from 7.4% to 8.1% with a low doping level of 0.5 mol%. More recently, those interesting results with Nb^{5+} doping have been adapted with success to ZnO-based DSSC ($\varnothing_{NPs} = 25$ nm), leading to an optimal doping level of 3 wt%.^[119]

Alternatives to anatase TiO_2 have been explored, mainly with the aim to improve charge collection or to decrease energy losses for electron injection. ZnO has been rapidly explored due to the very similar band structure to TiO_2 and the higher

electron mobility, i.e., TiO_2 : $0.1\text{--}1\text{ cm}^2\text{ V}^{-1}\text{ s}^{-1}$ ^[120] compared to $1\text{--}5\text{ cm}^2\text{ V}^{-1}\text{ s}^{-1}$ for ZnO.^[92–94,121] However, ZnO presents as a major drawback a rapid corrosion process in contact with iodine and lower chemical stability under acidic and basic conditions. This issue strongly jeopardizes both the stability and the performance of the solar cell, except if new redox mediators developed along the NIR-DSSC will pave the way to the utilization of ZnO.

Alternatively, SnO_2 is very interesting for NIR-DSSC application because of their higher transparency in the visible range due to the 3.8 eV bandgap value, the more oxidizing CB edge than TiO_2 and the higher electron mobility reaching up to $100\text{--}200\text{ cm}^2\text{ V}^{-1}\text{ s}^{-1}$ on a nanocrystalline film.^[122,123] However, faster electron recombination has been reported with the redox couple or with the dye cation.^[124,125] We estimate that further development of this semiconductor for NIR-DSSC is highly relevant, particularly in association with possible new NIR dyes or discarded NIR-dyes already developed but poorly efficient in association with the anatase TiO_2 as a result of too low-lying LUMO levels.^[126]

As an intermediate between TiO_2 and SnO_2 in terms of CB position, Zn_2SnO_4 has a CB edge located at -0.35 V versus NHE with an optical bandgap value of 3.6 eV.^[127,128] Optimized synthesis of this zinc stannate for DSSC has been reported in the literature by Chen et al. with different sizes and morphologies.^[128] The authors reported a PCE of 3.5% in association with N719 dye, a value low compared to TiO_2 , possibly due to too large energy losses for the injection process. However, Zn_2SnO_4 has the advantages of being chemically stable in the electrolyte compared to ZnO and exhibits higher electron mobility (ca. $10\text{--}15\text{ cm}^2\text{ V}^{-1}\text{ s}^{-1}$).^[127,129]

An effective strategy to reduce at least nongeminate recombination when fast one-electron redox couples are used is the surface modification of the NPs with a subnanometer thick shell of wide bandgap materials such as MgO ,^[130,131] SiO_2 ,^[132] Al_2O_3 ,^[133–135] ZnO ,^[136] ZrO_2 ,^[137] or $BaCO_3$.^[138] In the case of selective NIR-DSSC, Naim et al. reported in association with very low colored cobalt-based complexes redox couple an optimal PCE

for a very thin shell of 0.1 nm of Ga₂O₃.^[25] The authors observed an increase of both J_{sc} from 7.6 to 8.6 mA cm⁻² and V_{oc} from 387 to 406 mV, leading to a PCE increase from 1.9% to 2.3%. For selective NIR-DSSC, considering new materials than anatase TiO₂ nanocrystals can be extremely worthwhile not only to possibly improve AVT and PCE compared to current state-of-the-art, but it will open a new path to introduce new selective NIR-dyes having lower-lying LUMO levels than current NIR-dyes. Indeed, a broad range of NIR-dyes may have been discarded from the beginning because of the absence of charge injection into the TiO₂ nanocrystals and may become efficient new dyes in association with SnO₂ for instance, which is actually very promising in terms of transparency level as demonstrated in our group based on preliminary results associated with VG20-C₁₆ dye.

3.3. Redox Couples for NIR-DSSC

Currently, the major energy losses in DSSC are related to the dye regeneration for which the conventional I₃⁻/I⁻ redox couple requires at least 400 mV overpotential due to the two-electron transfer and bond creation.^[139] More than 200 mV is also needed in association with Co^{3+/2+} mediators. Although it is a fast redox couple, the oxidation of the Co²⁺ state leads to high reorganization energy due to structural rearrangement induced by the Jahn-Teller effect (single electron populating the antibonding E_g orbitals).^[140] The suitability of an efficient redox couple in a NIR-DSSC depends on several properties, namely i) its ability to regenerate the oxidized dye efficiently with low reorganization energy, ii) fast electron transfer rate at the counter electrode, iii) fast mass transport in particular within the mesoporous network, iv) high thermal, photo, and chemical

stability, and v) low molar extinction coefficient in the visible range (lower than 1000 L mol⁻¹ cm⁻¹). We can estimate that optimally the redox mediator should have a formal potential in the range of + 0.65 V versus NHE (normal hydrogen electrode) to reach high level of performance in conjunction with the already explored NIR-dyes (Figure 7).^[141]

Tri-iodide species are strongly absorbing below 450 nm, thus limiting the CRI and AVT values because of the obtained orange color of the electrolyte. To replace I₃⁻/I⁻ redox shuttle, metal-based redox couples have the great advantage of the redox potential tunability, fast redox couple as well as their optoelectronic properties, which can also be tuned by the introduction of an inductive donor or withdrawing units, which modify electron density on the metal center.^[142,143] A more oxidizing redox potential, closer to the dye HOMO level, would allow obtaining higher V_{oc} as a result of internal reduced energy losses for the dye regeneration.^[144] Two main classes of redox couples are existing. The first relies on metal complexes, i.e., Co^{3+/2+}, Cu^{2+/1+}, Fe^{3+/2+} or Ni^{4+/3+}. The second class of mediators is the pure organic molecules that can be transparent and non-corrosive, as the nitroxide or disulfide/sulfide systems.

3.3.1. Cobalt-Based Redox Systems

Historically, cobalt complexes represent a successful way to replace tri-iodide/iodide redox couple. It is a fast redox couple with, however, relatively nongeminate recombination kinetic due to low-spin (LS) to high-spin (HS) transition.^[145,146] When optimized, the use of cobalt complexes afford to increase the cell photovoltage through a decrease of internal energy losses. It led to important progress in the field of DSSC with successful PCE record braking up to today 14.3% PCE.^[147]

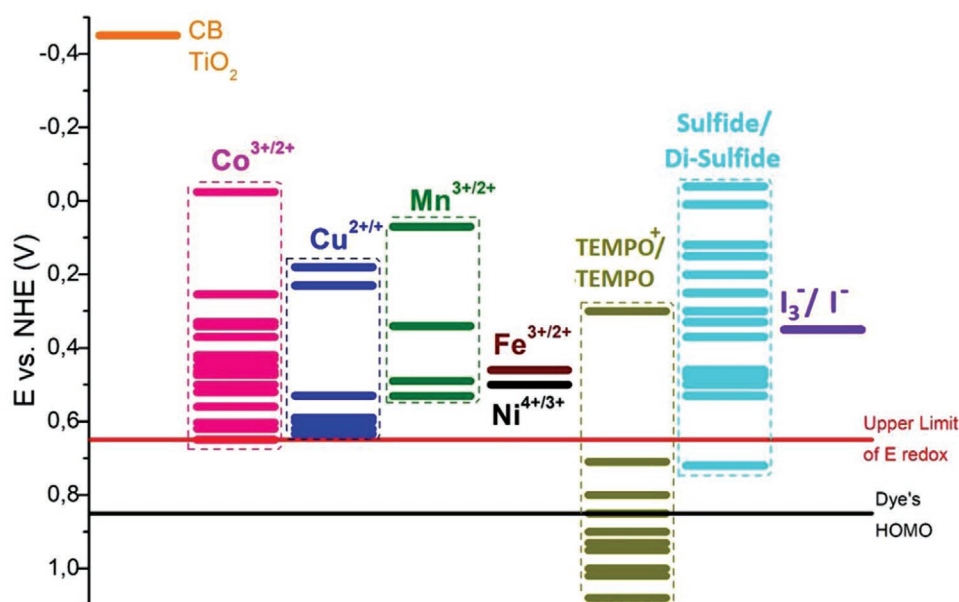


Figure 7. The dispersion of redox potentials for different types of redox mediators. Color of the lines are coded type of redox mediator: purple—cobalt-based, blue—copper-based, olive—manganese-based, wine—iron-based, black—nickel-based complexes. Dark yellow—TEMPO-based, cyan—disulfide-based organic redox mediators, violet—iodine redox mediator. The orange line shows the conductive band level for TiO₂. A black vertical line denotes the HOMO level of dyes for NIR-DSSC (see text for further details).

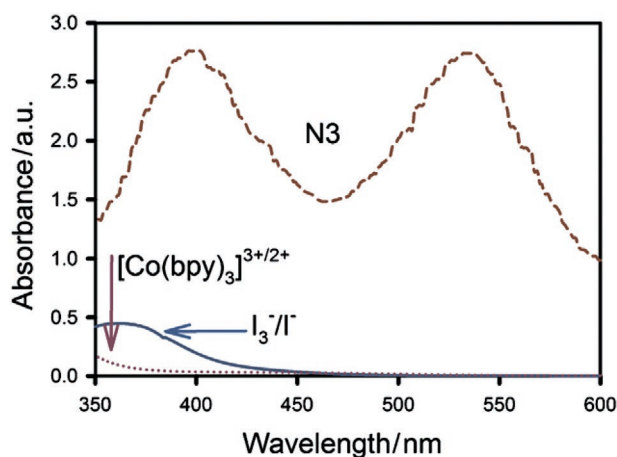


Figure 8. Absorption spectra of typical I_3^-/I^- and $[Co(bpy)_3]$ electrolytes, diluted to represent absorption of the electrolytes in the mesoporous films. Also shown is the absorption spectrum of the N3 dye for comparison. Reproduced with permission.^[157] Copyright 2012, Royal Society of Chemistry.

One advantage of introducing Co complexes for the field of the NIR-DSSC stems from the low absorption coefficient of both the reduced and oxidized form. The reduced form has just a weak absorption feature in the visible region compared to the typical I_3^-/I^- redox couple (Figure 8). The type of counterion can also slightly influence the absorption spectra and the apparent diffusion coefficient.^[148,149]

The physical properties of cobalt-based redox couples strongly depend on the spin states. All cobalt-based redox couples are characterized by Co(III) species having a closed-shell electron structure without unpaired electrons, which results in a low-spin state and translates into low absorption in the blue part visible region.^[150] For Co(II) species, the situation is not straightforward because the energy difference between the HS and LS configuration is relatively low. As such, spin-crossover processes can take place, which leads to a decreasing of formal redox potential and higher internal reorganization energy.^[151,152] The ground spin state depends on the ligand field strength. It can induce energy splitting of the t_{2g} and e_g orbitals.^[153–155] Cobalt-based mediators should preferably be close to the Co(II) state's spin-crossover point to achieve high dye-regeneration rates.^[151]

One of the first efforts to improve DSSC transmittance was reported in 2015 by Zaman Molla and co-workers, who combined a conductive oxide-free DSSC with a commercially available cobalt-based tris-bipyridyl electrolyte (Table 5 entry 1).^[145,156] The authors achieved similar photovoltage than the standard tri-iodide/iodide-based electrolyte.

In order to improve the cell photovoltage, common efforts from different groups focused on ligand modifications to replace the tris-bipyridine for increasing the redox potential.^[147,158] DFT calculations could be of particular interest in exploring the effects of ligand modification on the computed redox potential (Table 5 entry 2).^[159] Adding oxygen atoms on the peripheral ligand ring effectively increases the redox potential. Compared with bidentate ligands, tridentate ligands such as for instance the 6-(1H-pyrazol-1-yl)-2,2'-bipyridine,^[160] pentadentate (2,6-bis(1,1-bis(2-pyridyl)ethyl)pyridine)^[161] or the

most challenging to synthesize hexa-coordinated 6,6'-bis(1,1-di(pyridine-2-yl)ethyl)-2,2'-bipyridine, hexapyridyl 6,6'-bis(1,1-di(pyridine-2-yl)ethyl)-2,2'-bipyridine ligand (bpyPY4)^[162] are not only improving the complex stability but also afford reducing internal energy losses for the dye regeneration. The redox potential is not highly sensitive to the size of the ring or the relative position (ortho/meta/para) of multiple nitrogen atoms but subtle to the number of nitrogen/oxygen atoms.^[159]

Hamann et al. reported in 2012 three types of cobalt-based redox mediator, namely $[Co(R2-bpy)_3]^{3+/2+}$ (R = H, Me, t-Bu) (Table 5 entry 3 and 4), $[Co(X-phen)_3]^{3+/2+}$ (X = H, Cl, NO_2) (Table 5 entry 5–7). Through variation of the ligands and the introduction of electron-donating or electron-withdrawing substituents, the formal potential can be tuned by over 0.5 V. As above mentioned, an ideal redox potential of 0.65 V versus NHE can be achieved with the $[Co(dbbip)_2]^{3+/2+}$ (Table 5 entry 8).^[157] Of course, this is only indicative and some other closely related redox couples with a slightly lower redox potential remain important to be explored. This is the case for instance of the $[Co(phen)_3]^{3+/2+}$ or the $[Co(Cl-terpy)_2](TFSl)_{2/3}$ complex (Table 5 entry 9) for which the redox potential is slightly higher than the $[Co(bpy)_3]^{3+/2+}$ one (0.56 V vs. NHE).^[148] Both the reduced and oxidized forms of $[Co(Cl-phen-terpy)_2](TFSl)_{2/3}$ complexes show absorption maxima in the UV region, at 287 nm, with an extinction coefficient of 69700 and 62300 $L\ mol^{-1}\ cm^{-1}$, respectively (Figure 9a), thus opening the way to colorless devices.^[149]

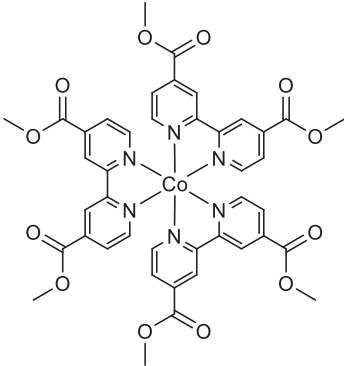
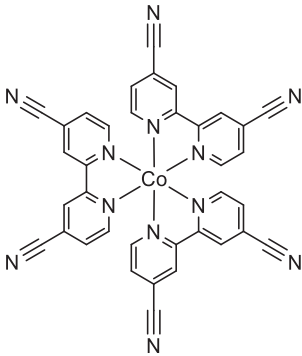
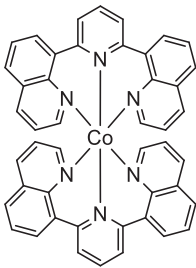
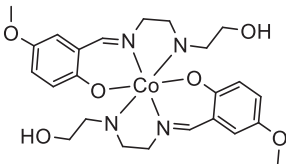
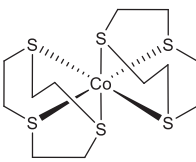
Another promising candidate as a transparent redox mediator is a cobalt complex based on bis[2,6-bis(1'-butylbenzimidazol-2'-yl)pyridine] ligand (dbbip).^[164,165] It displays a weak absorption of both oxidation states in the UV, i.e., $\lambda_{max} = 321\ nm$ for the $[Co(dbbip)_2]^{2+}$ and $\lambda_{max} = 309$ and 344 nm for the $[Co(dbbip)_2]^{3+}$ (Figure 9b). Its redox potential is 0.604 V versus NHE, which is comparable with the selected ideal threshold. Unfortunately, one drawback may stem from its slow diffusion coefficient and electron transfer at the platinum counter electrode, thus resulting in low fill factor values. Lowering the charge transfer resistance at the counter electrode can be obtained by increasing the thickness and/or the active area of the counter electrode or choosing different electrode materials (vide infra).^[166,167] Hence, its utilization can result in transmittance loss because of the higher loading electrocatalyst at the counter-electrode.^[165,166]

The modification of the redox potential by the insertion of different electron-withdrawing moieties in the ligand skeleton was studied on different redox mediators $[Co(dma-bpy)_3]^{2+}$, $[Co(me-bpy)_3]^{2+}$, and $[Co(cn-bpy)_3]^{2+}$ (dma-bpy = 2,2'-bipyridine-4,4'-bis(N,N-dimethylcarboxamide), me-bpy = 2,2'-bipyridine-4,4'-bis(methylester), cn-bpy = 2,2'-bipyridine-4,4'-dicarbonitrile) (Table 5 entry 10–12).^[168] This modification offers higher redox potentials and minimizes the impact of mass transport limitation on the photocurrent by introducing shorter alkyl chains.^[168] The redox potential decreases with the increase of the electron-withdrawing nature of the ligands in the order $[Co(cn-bpy)_3]^{2+}$ (0.9 V vs NHE) > $[Co(me-bpy)_3]^{2+}$ (0.72 V vs NHE) > $[Co(dma-bpy)_3]^{2+}$ (0.51 V vs NHE) $[Co(bpy)_3]^{2+}$. It is worth noticing that the complex stability tends to decrease as the redox potential increases. All mentioned cobalt complexes in both oxidized and reduced forms have strong absorption bands in the UV region and weaker band in the visible region ($<200\ M^{-1}\ cm^{-1}$), which

Table 5. Summary of cobalt-based redox couple suitable for NIR-DSSCs.

Entry	Name	Structure of complex	Redox potential (V vs NHE)	Absorption in the visible region [$M^{-1} cm^{-1}$]	Refs.
1	R=H [Co(bpy) ₃]		0.56	$\epsilon_{450} \approx 90$	[145]
2	R=OMe [Co(dMeO-bpy) ₃]		0.37	$\epsilon_{450} < 120$	[159]
3	R= t-Bu [Co(dtb-bpy) ₃]		0.42	$\epsilon_{440} \approx 140$	[157]
4	R=Me [Co(dm-bpy) ₃]		0.43	$\epsilon_{450} < 150$	[157]
5	X=H [Co(phen) ₃]		0.62	$\epsilon_{450} < 90$	[157]
6	X=Cl [Co(Cl-phen) ₃]		0.82	$\epsilon_{450} < 200$	[157]
7	X=NO ₂ [Co(NO ₂ phen) ₃]		0.92	$\epsilon_{450} < 200$	[157]
8	[Co(dbbip) ₂]		0.59-0.65	Co(II) $\epsilon_{480} = 130$ Co(III) $\epsilon_{480} = 260$	[165]
9	R=Cl [Co(Cl-terpy) ₂]		0.603	Co(II) $\epsilon_{440} = 849$ Co(III) $\epsilon_{440} = 395$	[148]
10	[Co(dma-bpy) ₃]		0.51	$\epsilon_{450} \approx 180$	[168]

Table 5. Continued.

Entry	Name	Structure of complex	Redox potential (V vs NHE)	Absorption in the visible region [$M^{-1} \text{ cm}^{-1}$]	Refs.
11	[Co(me-bpy) ₃]		0.72	$\epsilon_{450} \approx 300$	[168]
12	[Co(cnbpy) ₃]		0.90	$\epsilon_{450} \approx 120$	[168]
13	[Co(bqp) ₂]		0.56	$\epsilon < 1500$	[167]
14	SBCC		0.78	n/a	[170]
15	[Co(ttcn) ₂]		0.69	n/a	[150]

may originate from d–d forbidden transitions of the metal (Figure 9c). The matching between optimal redox potentials and the practically null absorption in the visible makes these complexes a really interesting choice as mediators in selective NIR-DSSCs.

The substitution of 2,2':6',2''-terpyridine with 2,6-bis(8'-quinolinyl)pyridine ligand in cobalt-based complexes resulted

in the formation of [Co(bqp)₂]^{3+/2+} (Table 5 entry 13) complexes with relatively weak absorption in the visible range of spectra, which also endorses their application for NIR-DSSC. Both oxidized and reduced forms exhibit absorption in the UV region assigned to ligand-centered π – π^* transitions. The broad and relatively weak absorption ($<1500 \text{ M}^{-1} \text{ cm}^{-1}$) observed in the visible region is due to charge transfer (CT) phenomena. The

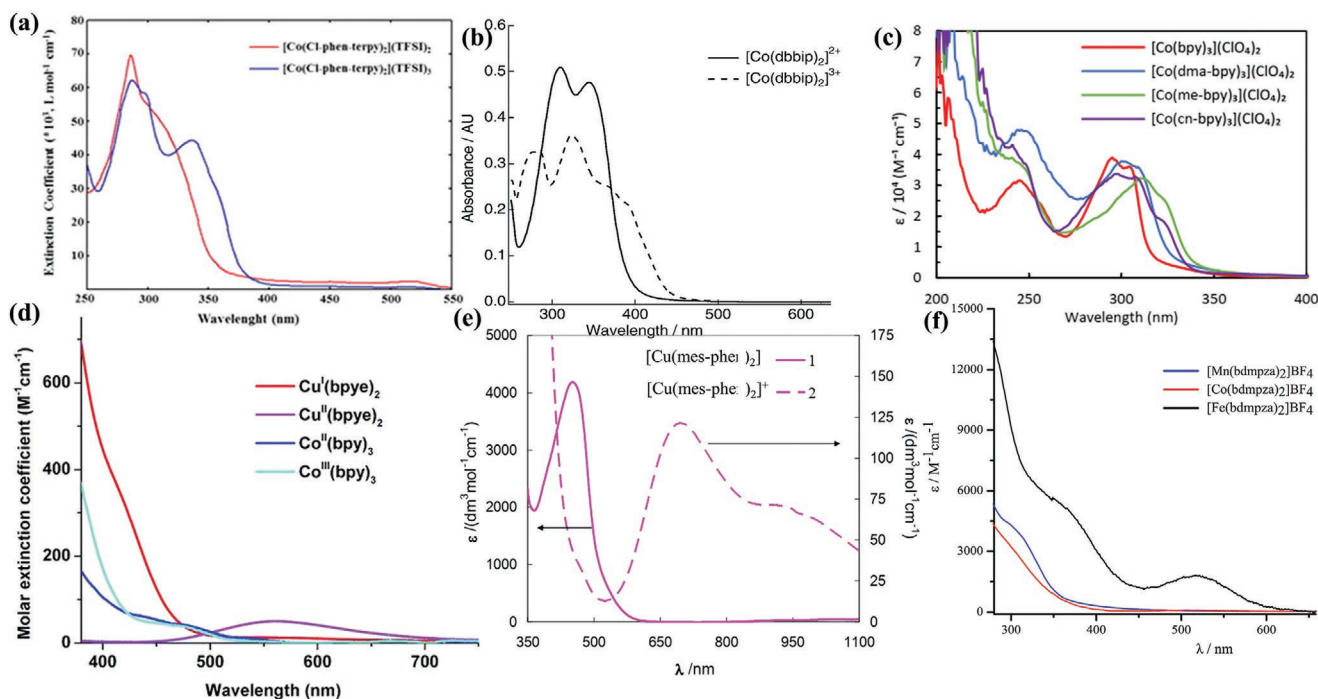


Figure 9. Absorption spectra of a) $[\text{Co}(\text{Cl-phen-terp})_2](\text{TFSI})_{2/3}$; ^[149] b) $[\text{Co}(\text{dbbip})_2]^{2+/3+}$; ^[164,165] c) $[\text{Co}(\text{dma-bpy})_3]^{2+}$, $[\text{Co}(\text{me-bpy})_3]^{2+}$, and $[\text{Co}(\text{cnbpy})_3]^{2+}$; ^[168] d) $[\text{Cu}(\text{bpye})_3]^{2+/+}$, $[\text{Co}(\text{bpy})_3]^{3+/2+}$; ^[176] e) $[\text{Cu}(\text{mes-phen})_2]^{2+/+}$; ^[178] f) comparison the absorption spectra of Mn, Cu, and Fe-based (bdmpza)₂ complexes; ^[180] a) Reproduced with permission. ^[149] Copyright 2013, Elsevier. b) Reproduced with permission. ^[164] Copyright 2001, American Chemical Society. c) Reproduced with permission. ^[168] Copyright 2015, American Chemical Society. d) Reproduced with permission. ^[176] Copyright 2016, Royal Society of Chemistry. e) Reproduced with permission. ^[178] Copyright 2016, American Chemical Society. f) Reproduced with permission. ^[180] Copyright 2017, Elsevier.

redox couple is fast as for most of this class of complexes with an equilibrium potential of 0.56 V versus NHE, which is 0.04 V more oxidative than $[\text{Co}(\text{tpy})_2]^{3+/2+}$ counterpart. ^[167]

Exploiting higher stability and higher oxidizing redox potentials, first reported by Nasr-Esfahani and co-workers, Schiff base metal complexes are potentially good candidates being their synthesis very straightforward and with quantitative yields (Table 5 entry 14). ^[169,170] The redox potential of the Schiff base cobalt complexes in acetonitrile is more positive than $[\text{Co}(\text{bpy})_3]$, leading to higher V_{OC} . However, J_{SC} , FF, and PCE values are still lower than the $[\text{Co}(\text{bpy})_3]^{3+/2+}$ -based reference device. ^[170] This may be attributed in part to the lower electron transfer rate at the platinum counter-electrode and the lower symmetry in the Schiff-based cobalt complex compared to the cobalt polypyridine complex.

The final goal of this part is to select/suggest unique redox mediators combining superior charge transfer properties, high transparency, and ability to regenerate NIR sensitizers efficiently. In this context, Hamann et al. employed different Co-based redox mediators with a NIR absorbing sensitizer (namely D35CPDT dye). ^[171] The approach led by Hamann et al. to obtain LS states Co(II)-based mediators was really meaningful in lowering reorganization energy by hampering the spin crossing. ^[150] Unfortunately, DSSCs employing $[\text{Co}(\text{ttn})_2]^{3+/2+}$ (Table 5 entry 15) suffered from faster nongeminate recombination dynamic compared to $[\text{Co}(\text{bpy})_3]^{3+/2+}$. As aforementioned, the first and sole real attempt to tailor a Co-based selective NIR-DSSC was made with VG20 dye and $[\text{Co}(\text{bpy})_3]^{3+/2+}$ as redox mediator in the electrolyte, delivering a 2.3% PCE, 68% AVT, and a CRI value of 92%.

When dealing with Co-based electrolytes, one should not forget that a major problem is the limited stability of the cobalt

complexes under prolonged irradiation conditions. There are several reasons for this lack of stability: i) dissociation of the complexes and ligand exchange, ii) cobalt complex adsorption on TiO_2 , and iii) slow irreversible oxidation of Co(II) by dissolved oxygen in the solvent. ^[172] Therefore, the effort in synthesizing transparent redox mediators should also match the requirement of long-term stability and the sustainability feature using cobalt may be questioned and be a penalizing point at the industrialization step. Indeed, cobalt is a Critical Raw Material. ^[173]

3.3.2. Copper-Based Electrolytes

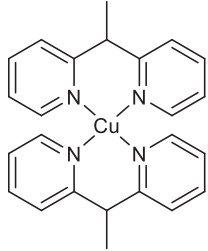
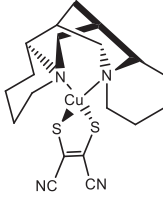
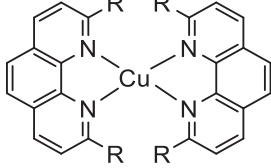
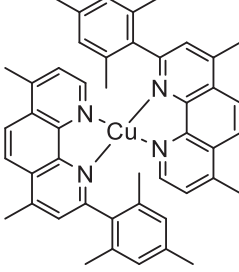
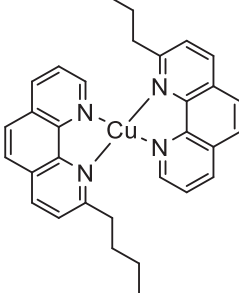
With the aim to replace cobalt metal center with a more sustainable and environmentally friendly transition metal, the first option is copper. The copper-based redox systems are particularly interesting as efficient redox mediators in liquid DSSCs because of their lower toxicity and their native property of having moderate reorganization energy that can be even further reduced by ligand engineering with fast electron self-exchange. This may also lead to a reduction in charge transport limitations and thus allow higher overall conversion efficiencies. ^[174,175] However, two important issues need to be tackled for their introduction in selective NIR-DSSC application. The first is the large difference in bond lengths and geometries between Cu(I) (tetrahedral) and Cu(II) (tetragonal) species, which can penalize the reorganization energy between the two oxidation states. Indeed, this could be milder by thoughtful engineering of the ligand. The second limitation is that Cu-complexes are usually much more absorbing in the visible region than the

Co-based counterparts (Figure 9d). In the following, we will briefly discuss some Cu-complexes effectively employed as redox mediators in conventional DSSC and we will evidence the details in order to reduce their absorption in the visible range and give some directions for the design of innovative, nearly colorless Cu-based redox couples.

A promising copper-based redox couple involving 1,1-bis(2-pyridyl)ethane (bpye) ligands were employed in the DSSCs showing not only promising efficiency but also highlight

the potential to develop further Cu-based redox couples for improving the NIR-DSSC technology (Figure 9d).^[176] The redox potential of $[\text{Cu}(\text{bpye})_2]^{2+/+}$ is 0.59 V versus NHE, which is 30 mV higher than that of $[\text{Co}(\text{bpy})_3]^{3+/2+}$ (Table 6 entry 1). The devices associating the $[\text{Cu}(\text{bpye})_2]^{2+/+}$ redox couple and the organic D- π -A LEG4 dye (3-(6-(4-(bis(2',4'-dibutoxy-[1,1'-biphenyl]-4-yl)amino)phenyl)-4,4-dihexyl-4Hcyclopenta[1,2-b:5,4-b']dithiophen-2-yl)-2-cyanoacrylic acid) exhibited a PCE of 9.0% ($V_{\text{OC}} = 904$ mV, $J_{\text{SC}} = 13.8$ mA cm⁻² and FF = 72%). The authors

Table 6. Summary of Copper-based redox couple of potential interests.

Entry	Name	Structure of complex	Redox potential (V vs NHE)	Absorption in the visible region [M ⁻¹ cm ⁻¹]	Refs.
1	$[\text{Cu}(\text{bpye})_2]$		0.59	n/a	[176]
2	$[\text{Cu}(\text{SP})(\text{mmt})]$		0.53	$\text{Cu(I)} \epsilon_{456} \approx 5 \times 10^3$ $\text{Cu(II)} \epsilon_{738} \approx 2 \times 10^3$	[177]
3	R=H $[\text{Cu}(\text{phen})_2]$		0.23	Weak	[177]
4	R=CH ₃ $[\text{Cu}(\text{dmp})_2]$		0.90	$\text{Cu(I)} \epsilon_{455} \approx 8 \times 10^3$ $\text{Cu(II)} \epsilon_{741} \approx 200$	[177]
5	R=mesityl $[\text{Cu}(\text{mes-phen})_2]$		0.60	$\text{Cu(I)} \epsilon_{451} \approx 4 \times 10^3$ $\text{Cu(II)} \epsilon_{696} \approx 150$	[178]
6	$[\text{Cu}(\text{dmmes-phen})_2]$		0.60	$\text{Cu(I)} \epsilon_{445} \approx 4.5 \times 10^3$ $\text{Cu(II)} \epsilon_{697} \approx 100$	[179]
7	$[\text{Cu}(\text{but-phen})_2]$		0.59	$\text{Cu(I)} \epsilon_{450} \approx 6 \times 10^3$ $\text{Cu(II)} \epsilon_{700} \approx 100$	[181]

demonstrated slower nongeminate recombination compared to the Co-based system and a higher photocurrent ascribed to a faster dye regeneration and improved charge collection efficiency. Aging under light exposure shows that, after an initial drop in PCE from 9% to 6%, the devices can remain afterward stable for up to 700 h.^[176]

The photophysical properties of a series of copper complexes, namely [Cu(SP)(mmt)]^{0/-} (Table 6 entry 2), (mmt = [(*-*-sparteine-N,N')](maleoni maleonitriledithiolato-S,S')) [Cu(phen)₂]^{2+/-} (Table 6 entry 3) (phen = 1,10-phenanthroline) [Cu(dmp)₂]^{2+/-} (Table 6 entry 4), (dmp = 2,9-dimethyl-1,10-phenanthroline) were reported by Hattori and co-workers.^[177] The one-electron redox potential of [Cu(SP)(mmt)], [Cu-(dmp)₂](CF₃SO₃)₂, and [Cu(phen)₂](CF₃SO₃)₂ in acetonitrile were determined to be 0.53 V, 0.90 V and 0.23 V versus NHE, respectively. The obtained cell photovoltage with these new mediators were in the range of 0.57–0.66 V with a trend agreeing the order of the redox potentials.^[177] Worse photovoltaic properties of [Cu(phen)₂]^{2+/-} compared to Co analogues-based devices were ascribed to the slower electron self-exchange rate and lower redox potential.

With a small change in the ligand structure, i.e., the absence of methyl moieties in the 2 and 7 position, [Cu(mes-phen)₂]^{2+/-} exhibits a similar redox potential value with respect to the dimethyl-substituted complex while the reorganization energy is changing (Table 6 entry 5). The absorption spectrum of the copper complex [Cu(mes-phen)₂]^{2+/-} in acetonitrile shows a broad absorption band centered at 451 nm with an absorption coefficient of $\epsilon_{\max} \approx 4 \times 10^3 \text{ M}^{-1} \text{ cm}^{-1}$ due to metal-to-ligand charge transfer (MLCT) transition, similarly to [Cu(dmms-phen)₂]²⁺ and [Cu(dmp)₂]⁺ exhibiting λ_{\max} at 445 nm ($\epsilon_{\max} \approx 4.5 \times 10^3 \text{ M}^{-1} \text{ cm}^{-1}$) and 455 nm ($\epsilon_{\max} \approx 8 \times 10^3 \text{ M}^{-1} \text{ cm}^{-1}$), respectively (Figure 9e). Its oxidized form [Cu(mes-phen)₂]²⁺ exhibits a much less intense transition centered at around 696 nm ($\epsilon_{\max} \approx 150 \text{ M}^{-1} \text{ cm}^{-1}$) as for [Cu(dmms-phen)₂]²⁺ and at 697 nm ($\epsilon_{\max} \approx 100 \text{ M}^{-1} \text{ cm}^{-1}$) and 741 nm ($\epsilon_{\max} \approx 200 \text{ M}^{-1} \text{ cm}^{-1}$) for [Cu(dmp)₂]²⁺.^[178] Colombo et al. investigated a new redox couple, namely [Cu(2-mesityl-4,7-dimethyl-1,10-phenanthroline)₂]^{2+/-} (named [Cu(dmms-phen)₂]^{2+/-}) and compared its efficiency with the 2,9-dimethyl-1,10-phenanthroline (named [Cu(dmp)₂]^{2+/-}), I⁻/I₃⁻ and [Co(dtb-bpy)₃]^{3+/2+} redox mediators (Table 6 entry 6).^[179] The complexes [Cu(dmms-phen)₂]^{2+/-} and [Cu(dmp)₂]^{2+/-} had redox potential close to 0.60 V versus NHE, comparable to Co-based reference.

Based on these works, it appears that the potentiality to introduce this class of complexes for application in NIR-DSSC is nested in the design of specific ligands having the ability to limit MLCT-type transition in order to lower the optical absorption of the Cu(I) species.

A fascinating springboard for sustainable DSSC can consider a solar cell based in which both dye and redox mediator are based on the same metal ions. The coupling of a copper dye with a copper electrolyte (Cu complexes with the 2,9-dimethyl-1,10-phenanthroline ([Cu(dmp)₂]^{2+/-}) and 2-*n*-butyl-1,10-phenanthroline ligands ([Cu(but-phen)₂]^{2+/-}) in a DSSC resulted in a PCE close to 3% (Table 6 entry 7).^[181–183] Unfortunately, this approach has a drawback for the implementation in NIR-DSSC because all copper dyes developed so far are exhibiting a strong absorption in the visible range.

3.3.3. Manganese and Iron-Based Electrolytes

Homoleptic manganese and iron-based complexes with mono-anionic N,N,O-heteroscorpionate ligands can be considered for NIR-DSSCs.^[180] Indeed, this type of ligand can be used as a model to study the influence of structural features on the characteristics of the redox mediator. Both Mn(II) and Fe(II) complexes are in the HS states based on magnetic measurements. A characteristic feature of these complexes is the internal reorganization caused by a Jahn–Teller effect or by spin-state changes upon the redox reaction. These effects may slow down the non-geminate recombination. The molecular structures for manganese and divalent iron complexes exhibit almost an octahedral, homoleptic coordination sphere around the metal center. Interestingly for the purpose of selective NIR-DSSC, the UV-Vis absorption fingerprint of such complexes shows no absorption in the visible range regardless of the oxidation state (Figure 9f). By contrast, a charge transfer band located at 517 nm was found for the Fe(III) complex, but with a sufficiently low molar extinction coefficient ($\epsilon \approx 1800 \text{ M}^{-1} \text{ cm}^{-1}$).^[184] Electrochemical characterization of [Mn(bdmpza)₂]BF₄ (Table 7, entry 1) and [Fe(bdmpza)₂]BF₄ (Table 7, entry 2), evidenced a reversible redox reaction located at 0.34 V and 0.46 V versus NHE, respectively.^[180]

In order to increase electrolyte transparency, tris(acetylacetonato) manganese (IV)/(III), [Mn(acac)₃]⁺⁰ (Table 7, entry 3) is a promising complex.^[185] A comparison of the UV-Vis spectra of the [Mn(acac)₃]⁺⁰ electrolyte and a typical [Co(bpy)₃]^{3+/2+} electrolyte shows that the former has lower absorption in the visible range ($\epsilon_{\max} = 143 \text{ M}^{-1} \text{ cm}^{-1}$ at 543 nm). The redox potential of the [Mn(acac)₃]⁺⁰ is 0.49 V versus NHE, thus approaching to the ideal value. However, the electron lifetime of devices including [Mn(acac)₃]⁺⁰ in the electrolyte is around 1 ms time, a one order of magnitude shorter compared to the benchmark I₃⁻/I⁻ redox couple or the [Co(bpy)₃]^{3+/2+}. This comparative study was carried out based on commercially available carbazole dye (MK2) and ruthenium N719 dye. For the sake of comparison, the PCE obtained with MK2 dye was 6.1% for cobalt-based, 4.6% for iodine and 4.4% for manganese-based redox couple.

Ferricinium/ferrocene redox couple (Fc⁺/Fc) and its derivatives are one-electron redox couples (Table 7 entry 4–14). They have been proposed in the literature by Spiccia et al. as an alternative to the benchmark I₃⁻/I⁻.^[186] Ferrocene molecule consists of a sandwich structure with the Fe(II) ions between two negatively charged cyclopentadienyl (Cp) rings, creating a very stable 18-electron system.^[187] Its most remarkable characteristic is its high stability to temperature, air, and water.^[188] The redox potential is independent of the solvent. One advantage of ferrocene as a redox mediator is that the regeneration process does not involve high-energy intermediate species, thus leading to negligible energy losses.^[186] Conventional DSSCs with ferrocene redox mediator yielded very good PCE values up to 7.5% in conjunction with a metal-free organic sensitizer Carbz-PAHTDTT.^[186] Unfortunately, its utilization for selective NIR-DSSC may be rather limited owing to its too high oxidizing potential, which will likely limit the dye regeneration kinetic. This is the case for instance, for VG20 dyes. In addition, ferricinium counterpart

Table 7. Summary of iron and manganese-based redox couple suitable for selective NIR-DSSCs.

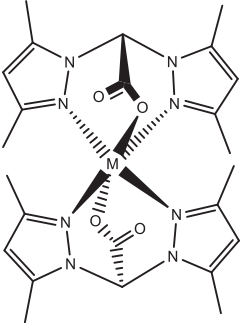
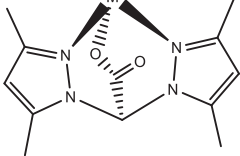
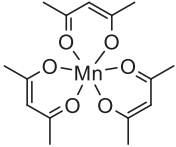
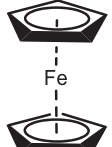
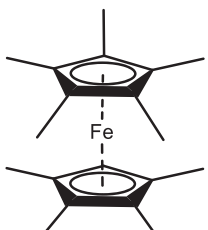
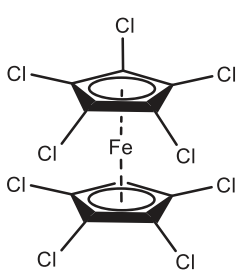
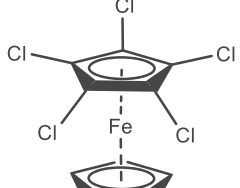
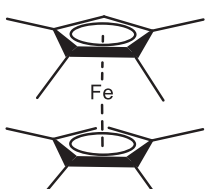
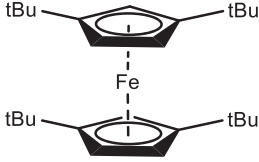
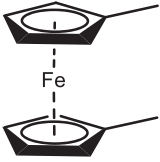
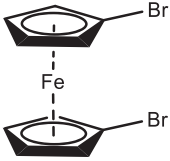
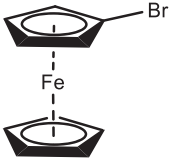
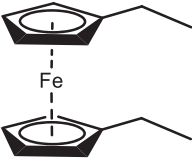
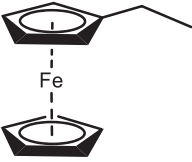
Entry	Name	Structure of complex	Redox potential (V vs NHE)	Absorption in the visible region [$M^{-1} \text{ cm}^{-1}$]	Refs.
1	M=Mn [Mn(bdmpza) ₂]		0.34	No absorption maxima for both Mn(II) and Mn(III)	[180]
2	M=Fe [Fe(bdmpza) ₂]		0.46	Fe(II) no absorption in the range 400–800 nm Fe(III) $\epsilon_{517} \approx 1816$	[180]
3	[Mn(acac) ₃]		0.49	Mn(III) $\epsilon_{550} \approx 75$ Mn(IV) $\epsilon_{543} \approx 143$	[185]
4	Fc/Fc ⁺		0.63	Fc $\epsilon_{442} = 95$	[186]
5	Me ₁₀ Fc/Me ₁₀ Fc ⁺		0.09	Fc $\epsilon_{423} = 97$ Fc ⁺ $\epsilon_{778} = 488$	[189]
6	Cl ₁₀ Fc/Cl ₁₀ Fc ⁺		0.95	n/a	[190]
7	Cl ₅ Fc/Cl ₅ Fc ⁺		0.80	n/a	[190]
8	Me ₈ Fc/Me ₈ Fc ⁺		0.24	Fc $\epsilon_{428} = 95$ Fc ⁺ $\epsilon_{750} = 380$	[191]

Table 7. Continued.

Entry	Name	Structure of complex	Redox potential (V vs NHE)	Absorption in the visible region [$M^{-1} \text{ cm}^{-1}$]	Refs.
9	$t\text{Bu}_4\text{Fc}/t\text{Bu}_4\text{Fc}^+$		0.41	$\text{Fc } \epsilon_{462} = 105 \text{ Fc}^+ \epsilon_{750} = 380$	[191]
10	$\text{Me}_2\text{Fc}/\text{Me}_2\text{Fc}^+$		0.54	$\text{Fc } \epsilon_{438} = 96 \text{ Fc}^+ \epsilon_{462} = 105$	[191]
11	$\text{Br}_2\text{Fc}/\text{Br}_2\text{Fc}^+$		0.94	n/a	[192]
12	$\text{BrFc}/\text{BrFc}^+$		0.80	n/a	[192]
13	$\text{Et}_2\text{Fc}/\text{Et}_2\text{Fc}^+$		0.51	n/a	[192]
14	$\text{EtFc}/\text{EtFc}^+$		0.57	n/a	[192]

is poorly stable as being very sensitive to oxygen and superoxide leading to the formation of dinuclear iron complexes. Interestingly, the redox potential of ferrocene can be easily tuned through the functionalization of the cyclopentadienyl rings with a variety of electron donating or withdrawing substituents.^[189,190] This approach was recently investigated by both Sauvage et al.^[191] and Bach et al.^[192] The alkylated Fe-complexes are probably the most interesting for selective NIR-DSSC application. By the introduction of such electron donor unit, the electronic enriching of the iron 3d orbitals confers to the complex valuable properties for the NIR-DSSC. It affords to stabilize the oxidized form noticeably.^[25] Second, it affords to modify the absorption features of both ferrocene and ferricinium derivatives. This family of redox mediators benefits from a low molar extinction coefficient due to the forbidden d-d transition, ensuring a negligible amount of light absorbed in the visible region.^[191] The introduction of

simple electron-donating units like the methyl or *tert*-butyl group on cyclopentadienyl rings afford great tunability of the redox potential down to 0.240 V versus NHE without drastically increasing the reorganization energy between Fe^{3+} and Fe^{2+} forms in the range of only few tenths of mV. The spin forbidden d-d transitions of ferrocene derivatives shift slightly toward the blue region with an increasing number of electron-donating groups on the cyclopentadienyl-rings with very little change in absorptivity values, whereas the ligand-to-metal transitions of the corresponding ferricinium salt move significantly to the near-IR region. These results clearly highlight that ferrocene-based redox couples can be a potential alternative for transparent electrolyte in selective NIR-DSSC with further development of cyclopentadienyl modified unit and with improved solubility in nitrile-based solvent which is today a major drawback in the utilization of such class of redox mediator.

Table 8. TEMPO-based redox couples of interest for selective NIR-DSSC applications.

Entry	Name	Structure of complex	Redox potential (V vs NHE)	Refs.
1	TEMPO ^{0/+}		0.80	[193]
2	OH-TEMPO ^{0/+}		0.90	[194]
3	NHCOCH ₃ -TEMPO ^{0/+}		1.00	[194]
4	CN-TEMPO ^{0/+}		1.08	[194]
5	[C-I][I] ^{0/+}		0.71	[195]
6	TEMPO-I ^{0/+}		0.30	[196]
7	TEMPO-III ^{0/+}		0.30	[196]
8	[MeIm-TEMPO][TFSI] ^{0/+}		1.02	[197]
9	[Im-TEMPO][TFSI] ^{0/+}		0.93	[198]

Table 8. Continued.

Entry	Name	Structure of complex	Redox potential (V vs NHE)	Refs.
10	[Im-bisTEMPO][TFSI] ^{0/+}		0.95	[198]
11	AZA ^{0/+}		0.85	[199]

3.3.4. Organic-Based Redox Mediator

Besides the metal-based redox couples, purely organic redox mediators represent an important sake for the application in selective NIR-DSSC to achieve colorless devices and overcome the limitations displayed by the metal-based redox couples in terms of more transparency and improved sustainability compared to transition metal complexes.^[173] Indeed, organic redox molecules are, in principle, easier to synthesize and recycle. It can take advantage of relatively cheap starting materials and fewer synthetic steps, thus resulting in more cost-effective and sustainable redox mediators.^[173]

The first application of an organic redox couple in DSSCs was reported by Grätzel et al. in 2008 using the 2,2,6,6-tetramethylpiperidine-1-oxyl (TEMPO) (Table 8 entry 1).^[193] The corresponding solar cell based on D149 achieved a promising PCE of 5.4% compared to 6.7% with the standard triiodide/iodide redox couple. Despite the superior photovoltage, TEMPO-based electrolyte is penalized by faster nongeminate recombination and well-known instability of the oxidized TEMPO⁺, which affects not only the device performance and stability but also jeopardizes this type of redox mediator for application.

TEMPO is a radical-type redox mediator which involves a fast one-electron process at 0.80 V versus NHE (Figure 10). This type of radical redox couple affords to have transparent electrolyte and optimally limits internal energy losses as it has no reorganization energy while displaying all the features of a very rapid redox system. It has a greater diffusion coefficient, between 10⁻⁵ to 10⁻⁴ cm² s⁻¹ compared to less than 10⁻⁵ cm² s⁻¹ for the metal-based redox couples.^[142] Unfortunately, its high redox potential makes it hardly exploitable for narrowed bandgap NIR sensitizers. Indeed, most of these sensitizers have HOMO energy levels also in the range of 0.8 V versus NHE. However, new design of such NIR sensitizers can potentially open the way for TEMPO^{0/+} compatibility for selective NIR-DSSC. As a matter of fact, also for the nitroxide species, the redox potential can be finely tuned by inserting different types of substituents in the 4-position. Indeed, the

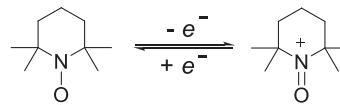


Figure 10. TEMPO oxidation process.

Table 9. Disulfide/thiolate-based redox couples of interest for selective NIR-DSSC.

Entry	Name	Structure of complex	Redox potential (V vs NHE)	Refs.
1	TMFDS ²⁺ / TMTU		0.53	[200]
2	T ₂ /T ⁻		0.48	[169]
3	BAT/AT ⁻		0.53	[205]
4	BET/ET ⁻		0.48	[213]
5	n-BuT ₂ /T ⁻		0.48	[207]
6	n-HexT ₂ /T ⁻		0.48	[207]
7	n-OctT ₂ /T ⁻		0.48	[207]
8	DTT/TT ⁻		0.12	[208]
9	SD/S ⁻		0.50	[206]
10	BMT/ McMT ⁻		0.15	[209]
11	BMO/ McMO ⁻		0.25	[210]
12	BPO/ McPO ⁻		0.37	[210]

Table 9. Continued.

Entry	Name	Structure of complex	Redox potential (V vs NHE)	Refs.
13	MTDD ²⁺ / MDTD		0.47	[211]
14	BMIT/BMIDT		0.72	[212]

insertion of the electron-withdrawing unit was proved to positively shift the redox potential while leading to lower diffusion coefficients (Table 8 entry 2–4).^[194] Further modifications on 4-position have been carried out by attaching hindered moieties to prevent the charge recombination (Table 8 entry 5–10). The latter has been applied in hybrid systems with iodide source-based ionic liquids in a liquid electrolyte, improving the thermal stability, the life of the cell and the general performance of the devices.^[195–198]

A relevant breakthrough for the NIR-DSSC field in nitroxide radicals was achieved by the synthesis of a structure based on 2-azaadamantan-N-oxyl (AZA) (Table 8 entry 11). The rigid and symmetric adamantane framework inhibits the elimination of the α -substituted protons improving the stability of the oxidized form, albeit it also leads to a slightly too high redox potential of 0.85 V versus NHE. The lower hindered structure of AZA confers a higher diffusion coefficient in the electrolyte. Combining AZA redox couples and D205 dye, Nishide et al. achieved a very promising PCE of 8.1%.^[199] However, important efforts in synthesis are needed since, although these radical redox mediators gather all desirable properties, either the redox potential is too high or below current triiodide/iodide redox couple but do not fall in the desired range of 0.65 V versus NHE.

Alongside nitrosyl-based couples, disulfide/thiourea and disulfide/thiolate-based redox couples are highly interesting since their redox potential is sufficiently more positive than the HOMO energy level of the current NIR-sensitizers. In 2010, Li et al.^[200] reported a non-corrosive electrolyte based on tetramethyl thiourea (TMTU) (Table 9 entry 1). TMTU and its oxidized dimer species (TMFDS²⁺) are colorless and soluble in common nitrile solvents. The redox couple is reversible at 0.53 V versus NHE. It is a two-electron redox process to lead to the disulfide bridge formation for the oxidized species (Figure 11).^[201] This different behavior produces electronic interstates and leads to higher reorganization energies.

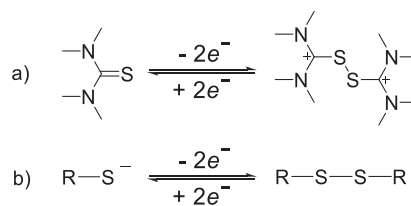


Figure 11. a) TMTU oxidation process. b) disulfide/thiolate oxidation process.

The lower activity of Pt counter-electrode towards all disulfide/thiolate-based redox couples requires the development of innovative materials based on carbon, inorganic compounds, and conducting polymers that will be discussed in Section 3.4.^[202–206] Further investigations on TMFDS²⁺/TMTU redox couple focused on its interaction with different types of sensitizers, such as the ruthenium complexes and common organic sensitizers as indoline. The authors highlighted an improvement of regeneration yield in organic dyes associated with TMFDS²⁺/TMTU redox mediator.^[200,201]

The same year, Grätzel et al. reported a closely related disulfide/thiolate redox couple based on 5-mercapto-1-methyltetrazole (named, T⁻) (Table 9 entry 2), paving the way to the development of several azole-based redox couples.^[169] Compared to the TMFDS²⁺/TMTU system, this family of tetrazole redox mediators has the same negligible absorption in the visible range and has an easier tunability of the redox potential. The alkyl substitution with a progressive longer chain and bulkier substituent leads to a gradual decrease in the apparent diffusion coefficient of the redox couple without affecting its redox potential (Table 9 entry 3–7).^[205,207,213] Moving on triazole, the redox potential can be noticeably decreased compared to the tetrazole counterpart. Therefore, this triazole family may not represent an ideal candidate as a suitable transparent electrolyte for selective NIR-DSSC. For instance, the DTT/TT⁻ shows a redox potential of 0.12 V versus NHE only (Table 9 entry 8) and a maximum of 0.50 V versus NHE has been achieved on SD/S⁻ redox couple (Table 9 entry 9) thanks to the incorporation of a very strong CF₃ electron-withdrawing unit.^[206–208] Intermediate values of redox potential can be obtained by modifying the central core with different heteroatoms, for

instance, by replacing one nitrogen atom by sulfur or oxygen (Table 9 entry 10–12)^[209,210] or by merging to a thione-based reduced species (Table 9 entry 13).^[211] The thiopropionic acid-based redox couple (Table 9 entry 14) reported by Yan et al. is the only example of a mediator based on this structure. It is so far the most oxidizing redox mediator based on disulfide/thiolate chemistry attaining as high as 0.72 V versus NHE. As seen for the tetrazole, the thiopropionic acid-based redox couple is also characterized by a negligible absorption in the visible range.^[212] Among all disulfide/thiolate-based couples proposed in the literature, BAT/AT⁻ (Table 9 entry 3) and BET/ET⁻ (Table 9 entry 4) were interestingly applied in combination with a fully transparent counter-electrode based on PEDOT and NiS, achieving PCE of 6.07% and 6.25% in association with N719 dye, respectively.^[213,214]

Two-electron organic redox couples based on benzoquinone/hydroquinone have been reported with colorless features (Figure 12a).^[215–217] The advantage compared to the dithiolate is the absence of a dimeric structure formation, which consequently reduces energy losses related to the bond formation and covalent S–S bond cleavage. It also alleviates the role of the electrocatalyst for the counter-electrode.

The two-electron process is well-visible on the cyclic voltammogram with the occurrence of two quasi-reversible processes at 0.19 V versus NHE and 0.59 V versus NHE (Figure 12b).^[215,216] However, the first electron process is too low for practical application and the second process suffers from instability issues in air. This leads to important precautions needed for the electrolyte storage while also requiring device fabrication under inert atmosphere. Long-term stability will also call for robust encapsulation.

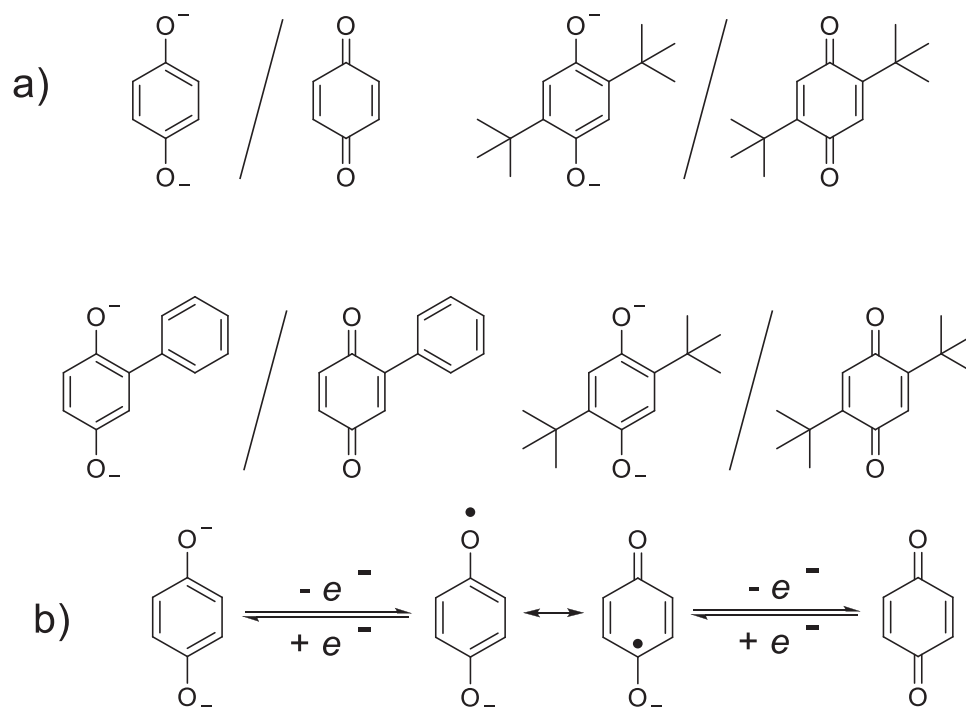


Figure 12. a) Benzoquinone/hydroquinone-based redox couple and b) Benzoquinone/hydroquinone oxidation process.

Table 10. Binary redox systems.

Entry	Redox mediator	Redox potential (V vs NHE)	Ref.
1	I^-/I_2^- , I_2^-/I_2Br^-	0.56	[219]
2	I^-/SCN^- , I_3^-/I_2SCN^-	0.47	[220]
3	S_2^-/S_2^{2-} and I^-	0.75 and 0.35	[222]
4	TEMPO ⁺⁰ and Co(bpy) ₃ ^{3+/2+}	0.80 and 0.56	[223]
5	TPAA ⁺⁰ and Co(bpy) ₃ ^{3+/2+}	0.79 and 0.56	[224]

3.3.5. Binary Redox Systems

In the context of colorless and transparent NIR-DSSC, binary-based redox couples are one important alternative that should be considered seriously. The first binary system reported consisted of the addition of a second redox species in the iodide-based electrolyte either to form a new interhalogen/pseudohalogen species, to reduce the amount of tri-iodide present in the electrolyte, thus lowering the light absorption in the visible range substantially, or to insert an intermediate step for the dye regeneration. These redox couples have been primarily elaborated to enhance the cell photovoltage.^[218]

Nath et al. have examined both interhalogen and pseudohalogen redox couples ($I^-/Br^-/I_2^-/I_2Br^-$) and ($I^-/SCN^-/I_3^-/I_2SCN^-$) (Table 10 entry 1 and 2).^[219,220] The formation of the interhalogen ion, determined via ESI-MS, was characterized by cyclic voltamperometry. It was found a more positive redox potential than the benchmark I_3^-/I^- redox couple. Recently, for the case of the mixed Br^-/I^- redox couple, it was proven the possibility to tune the light absorption in the visible by varying the relative concentration of I^- and Br^- in the electrolyte.^[221]

With the aim of reaching transparent electrolytes, the work of Cong et al. requires particular attention by mixing sulfur and iodine (Figure 13, Table 10 entry 3).^[222] This type of electrolyte has been optimized in association with VG20-C₁₆ dye in our group. It was achieved excellent optical properties in light of an AVT value crossing 80% threshold, a value greater than double

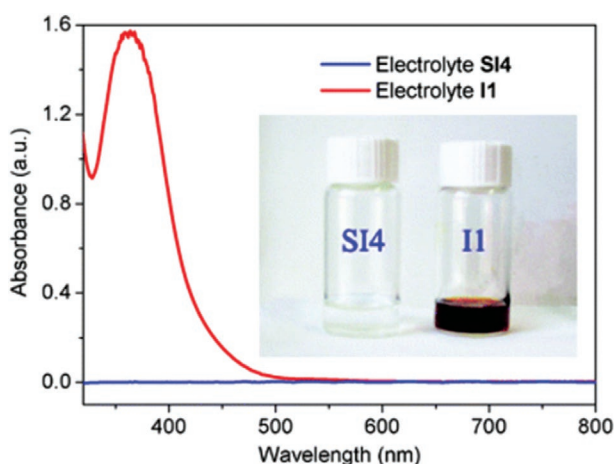


Figure 13. UV-vis absorption spectrum of S_2^-/S_2^{2-} and I^- redox couple compared to I_3^-/I^- redox couple. Reproduced with permission.^[222] Copyright 2012, Royal Society of Chemistry.

glazing windows, and a CRI of 96%. This is the best optical result of a selective NIR-DSSC reached so far and among the best values reported for TPV. The devices exhibited a maximum PCE of 2.5%. Cong et al. also pioneered the hybrid redox system between TEMPO and Co complexes (Table 10 entry 4).^[223] The most relevant finding in this work is nested in the observation of a faster dye regeneration, slowing down the fast recombination issue of the TEMPO and reducing the mass transport problematic of the Co complexes, thus resulting in a higher cell photovoltage. However, as previously mentioned, TEMPO, other than being highly unstable in its oxidized form, has a redox potential too close to actually reported HOMO levels of the NIR-dyes.

An alternative to TEMPO was found in TPAA (tris(p-anisyl) amine) by Hao et al. (Table 10 entry 5). The introduction of this molecule ensures higher stability in MPN electrolyte compared to the TEMPO-Co redox system while maintaining the optimized electron transfer kinetics on the photoanode side.^[224] Unfortunately, also in this case, the redox potential lies too close to the dye's HOMO level (0.79 V vs NHE), thus may be a very interesting solution waiting for NIR-sensitizers with stronger stabilized HOMO levels.

A thoughtful design of the redox mediator and more generally, of the electrolyte is mandatory to obtain transparent and colorless DSSCs providing a good photoconversion efficiency. The former choice could lead to the implementation of metal-based complexes: they have been thoroughly investigated to be implemented in the conventional device and their chemistry is well known. Among them, transparency-wise, cobalt complexes seem to be the most promising one coupling practical null absorption in the visible region and good efficiency in conjunction with NIR dyes. On the other hand, fast recombination reaction at the photoanode/electrolyte interface limits the device's efficiency. Moreover, some serious issues arise in terms of sustainability, being cobalt a Critical Raw Material. In order to overcome these two issues, cobalt could be replaced by other metals, i.e., copper, iron, or manganese. Copper complexes have been profusely investigated in conventional devices (both in liquid and solid configuration); by means of ligand engineering is possible to reduce the reorganization energy required in the Cu(I)–Cu(II) transition leading to maximized efficiency. Unfortunately, the most important drawbacks of Cu-based redox mediator are their partial absorption in the visible range that seems to prevent their application in colorless DSSCs; yet, some efforts have been made in order to properly modified the organic ligand to shift the MLCT in the UV region and to reduce the contribution of the d–d. Aiming at complete transparency in the visible range, both iron and manganese could be valuable choices. Ferrocene and its derivatives, once implemented in complete devices, lead to very high AVT but the overall efficiency (and thus LUE) is quite limited due to the high redox potential that prevents efficient dye regeneration. In this case, ligand engineering just slightly influences the electrochemical properties of the complexes. With respect to manganese complexes, just few but promising results have been reported so far.

Besides metal-based complexes also fully organic redox systems have been proposed to be applied in colorless DSSCs, being characterized by very low absorption in the visible range. Two main classes of redox systems have been investigated so

far, namely TEMPO-based and disulfide/thiolate-based redox couples. The former, widely employed in conventional DSSC is hardly exploitable in NIR-based device because of a too high redox potential (between 0.80 and 1.00 V vs NHE) that makes impossible an effective regeneration of the NIR dye. On the other hand, disulfide/thiolate-based redox couples show more suitable redox potential but they are characterized to slower electron transfer kinetic due to required bond formation/cleavage. Indeed, some efforts deal with the modification of the organic scaffold to limit the energy losses of this process and to optimize the PCE. Additionally, disulfide/thiolate systems also require tailored counter electrode to prevent their irreversible absorption, e.g., on platinum films. Very recently, also binary redox systems have been proposed. The aim of the exploitation of the latter is to couple the advantages of each system, trying to minimize the drawbacks. This binary allows obtaining colorless electrolytes that properly work also in conjugation with NIR dyes opening the way to transparent and efficient DSSCs.

3.4. Fully Transparent Counter Electrodes

The counter electrode (CE) is the last important part of the DSSC to ensure the effective regeneration of the reduced form of the redox couple while closing the circuit of the photogalvanic cell.^[225] The property of the CE influences the device performance in particular through the fill factor value.^[226] The support FTO glass is usually coated by a nanocatalyst to reduce the charge transfer resistance (R_{CT}) at the counter electrode, thus the type of electrocatalyst strongly depends on the type of redox mediator used in the electrolyte. The prerequisites for the electrocatalyst are i) high electrochemical catalytic activity for the reduction process and to avoid electrode polarization,^[227–229] ii) inertness with respect to the electrolyte components, and iii) high thermal and photostability. For NIR-DSSC, the CE requires a high level of transparency which can be achieved either by an ultrathin electrocatalyst layer or via a transparent conducting material.

Historically, a platinum-coated FTO glass is employed as a CE. It represents so far the best electrocatalyst to reduce tri-iodide to iodide. On the other hand, it can be corroded by iodine-based redox couples in particular for electrolytes free of guanidinium thiocyanate.^[230] Best performing devices usually involve opaque Pt-based CE deposited either by screen-printing or drop-casting.^[231,232] In this case, the CE displays relatively high optical reflectance,^[231] which can enhance light confinement in the device of regular DSSC but is an out parameter for NIR-DSSC application. Controlling the thickness of the electrocatalyst layer to a level that will become optically transparent while maintaining its high electrochemical activity is an important stake.^[233,234]

Otaka et al. demonstrated that a Pt thickness as low as 0.5 nm has no negative impact on the photovoltaic characteristics while providing a good transmittance in the visible region,^[235] thus appealing for selective NIR-DSSC application^[236] and for bifacial devices.^[237] Alternatively, Gong et al. reported a film transmittance reaching 95% for rGO-modified Pt films, leading to a PCE of 7.7% (Table 11 entry 1).^[238] Note that in this case, the

Table 11. Different classes of transparent counter-electrode of possible interest for selective NIR-DSSC.

Entry	Material	Transmittance [%]	Electrolyte	Photocurrent density [mA cm ⁻²] and PCE value (%) into brackets	Refs.
1	rGO+Pt	90%	I ₃ ⁻ /I ⁻	16 (7.7)	[238]
2	rGO	81%	I ₃ ⁻ /I ⁻	16 (3.6)	[243]
3	Exfoliated Graphene	Same of FTO (only relative data available)	I ₃ ⁻ /I ⁻	12 (3.2)	[246]
4	Graphene	85%	I ₃ ⁻ /I ⁻	6 (2.3)	[244]
5	CoS honey	65%	I ₃ ⁻ /I ⁻	14 (6.0)	[266]
6	CoS	80%	I ₃ ⁻ /I ⁻	17 (8.5)	[267]
7	NiS	75%	I ₃ ⁻ /I ⁻	12 (5.9)	[275]
8	NiS	82%	I ₃ ⁻ /I ⁻	15 (7.4)	[276]
9	NiSe	88%	I ₃ ⁻ /I ⁻	17 (8.0)	[262]
10	FeSe	78% at 550 nm	I ₃ ⁻ /I ⁻	17 (9.2)	[279]
11	MoS ₂	79%	I ₃ ⁻ /I ⁻	17 (7.4)	[280]
12	Mo _{0.6} Se	85%	I ₃ ⁻ /I ⁻	16 (8.0)	[279]
13	CuSe	100%	I ₃ ⁻ /I ⁻	12 (6.0)	[284]
14	Cu _{2-x} Se@N-doped carbon nanosheets	83%	Co-based	13 (7.6)	[285]

contribution of the FTO substrate was subtracted in the transmittance calculation.

When selecting appropriate electrocatalysts to replace the platinum, it has been considered that both the charge transfer resistance and the sheet resistance should be low enough to ensure a fast electron transfer to the FTO layer.^[225] It should be pointed out that both transmittance and sheet resistance are intrinsic properties of the film depending on the deposition technique and the conditions of the thermal post-treatment. Among alternatives to platinum, carbonaceous materials,^[239] conducting polymers,^[240] and metal oxides or sulfides (except for the Co-based ones),^[241] can provide excellent catalytic properties while remaining low cost and sustainable. However, most of them do not comply with the transparency standard required.

Among C-based materials, graphene and reduced graphene oxide (rGO) have attracted great attention due to their unique features, combining excellent electrical and thermal conductivity with high optical transparency at the sub-nanometer thickness (Table 11 entry 2).^[242,243] Yet, the deposition of graphene sheets onto FTO glass remains challenging. Both transmittance and conductivity strongly decrease when more than 4–5 sheets are deposited.^[244,245] Nemala et al. reported on the application of pressure exfoliated single graphene sheet as possible CE in DSSC (Table 11 entry 3).^[246] They have reached a transparency level close to 100%. However, the low catalytic activity of the CE with respect to the tri-iodide/iodide redox system strongly penalized the fill factor value compared to Pt. Dodo-Arhan et al. reported on a graphene layer grown by chemical vapor deposition (CVD) on FTO reaching a transmittance value of 80% and a PCE of 4% ($\text{ff} = 55\text{--}60\%$) with a custom-made I-based electrolyte.^[247] Similar transmittance values (81%) and

power conversion efficiency (3.6%) were reported by Jang et al. with moderately reduced GO. Another example of rGO films was reported by Roy-Mayhew et al. who successfully achieved thermally reduced graphene oxide CE efficient for iodine-based, Co-based and S-based redox mediators, reaching a PCE of 6.7%, 4.5%, and 3.5%, respectively.^[248] The advantage of a thermally driven reduction of graphene oxide is nested in its higher level of transparency compared to the ones conventionally obtained with chemically or electrochemically rGO.^[249] An innovative approach was reported by Choi et al., who produced rGO by the Hummer's method and successively deposited it onto FTO glass by electrophoresis.^[244,250] By controlling the deposition time, they were able to modulate both film transparency and its electrochemical activity. For short deposition time (5 seconds under 30 V polarization), 85% transparency was achieved with a film able to support current density close to 6 mA cm⁻² (Table 11 entry 4). However, longer deposition time was reported to affect both the optical and the electrical properties of the resulting film.

For transparent CE, research on conducting polymers is also very fruitful due to their good catalytic activity, excellent stability, and ease of tuning their properties through simple synthetic modifications.^[251–254] Yet, a relatively thick polymeric film is required to achieve a good catalytic activity, meaning that transmittance values higher than 70% are hardly obtainable. However, few noteworthy exceptions have been reported. For example, Lee et al. successfully reduced by in situ polymerization a PEDOT-based CE thickness down to 60 nm leading to a transmission value of 88% at 550 nm.^[255] However, compared to carbon-based CE, the film obtained exhibited a relatively high surface resistivity of 140 Ω sq⁻¹. This characteristic can be mitigated by the introduction of a graphene layer sheltering the PEDOT film. This affords to enhance the overall film's mechanical stability while decreasing the surface resistivity down to 60 Ω sq⁻¹. This has a beneficial consequence for reducing the charge transfer resistance, by ≈50% compared to Pt with an I-based electrolyte.^[245] Unfortunately, the introduction of a graphene layer with their methodology reduced the CE transmittance down to 70% due to excessive light interactions at the interface between the two materials.

Grätzel et al. proposed a new class of CE based on transition metal materials, namely CoS.^[256] This new family has been extended to sulfides and selenides (TMS),^[257] phosphides (TMP),^[258] nitrides (TMN),^[259] carbides (TMC),^[260] and oxides (TMO).^[261] A systematic study for iron, nickel, cobalt selenides, and sulfides as counter-electrode started back in 2009 as a result from potential lower cost.^[226,262–264] TMSs and TMOs are the most widely investigated electrocatalyst as being easily synthesizable even for large areas together with being thermally, chemically, and electrochemically robust. TMNs and TMCs usually exhibit very good electrocatalytic activity, especially with I₃⁻/I⁻ redox couple, albeit they are less robust than their oxide and sulfur-based counterpart. PCE value is regularly the main metric highlighted while the optical properties of the CE or the charge transfer resistance grasped less attention.

Cobalt selenides and sulfides were first investigated, obtaining power conversion efficiencies comparable to the standard of Pt.^[256] Congiu et al. highlighted the superiority of CoS with an I₃⁻/I⁻ based electrolyte in terms of charge transfer

resistance: 1.51 and 2.30 Ω cm² for CoS and Pt, respectively. A similar level of transparency was obtained between the two CE, 78% at 555 nm compared to 82% for Pt.^[265] The transparency of the CE strongly depends on the morphology of the particles. For example, Lin et al. reported CoS-based CE with a honeycomb morphology also reaching a higher level of performances ($R_{CT} = 1.45 \text{ } \Omega \text{ cm}^2$) than Pt-based CE ($R_{CT} = 2.03 \text{ } \Omega \text{ cm}^2$) (Table 11 entry 5). However, the high crystallinity of the film penalizes the film's transmittance which only reaches a maximum of ca. 65%.^[266] More transparent (>80% transmittance at 555 nm) and more efficient CE films were obtained by Huo et al. through a hydrothermal approach leading to a PCE = 8.5%, $J_{SC} = 17 \text{ mA cm}^{-2}$.^[267] In addition, the authors modified these films with a controlled amount of rGO allowing to reach a PCE of 10%.

Nickel oxide nanoparticles have been largely employed in p-type DSSC,^[16,268] and its catalytic activity toward the reduction of tri-iodide has been thoroughly reported. However, under continuous illumination, negative charged iodide species tend to strongly chemisorb onto the electrode's surface, limiting its catalytic activity.^[269] To avoid this drawback, NiSx and NiSex materials have been largely explored as a new type of CE.^[270–273] These materials are cost-effective and could be easily synthesized.^[274] However, some precautions are required to be taken during the synthesis to avoid the formation of hydroxide and oxide phases that jeopardize both the catalytic activity and the stability of the CE in complete devices. The synthesis under H₂S or H₂Se flow is required to avoid the formation of harmful impurities. Zhang et al. investigated the effect of the morphology of NiS nanostructures on their optoelectronic properties (Table 11 entry 7).^[275] The morphology could be carefully modulated by the amount and the nature of the template employed during the synthesis. Among the different nanostructures proposed, the nanosphere was proved to be the most transparent (75% at 555 nm), however with a lower catalytic activity (R_{CT} = 6.68 Ω cm², that the double compared to Pt-based CE, respectively, when an I-based electrolyte is employed). The highest level of electrocatalytic activity is obtained with nanoflower-type morphology but at the expense of the film's transparency owing to aggregation. A step forward in this trade-off between transparency and electrochemical activity has been demonstrated by the work of Song et al., who reached a high level of transparency greater than 80 % over the whole spectrum (Table 11 entry 8).^[276] The replacement of sulfur with selenium improves the electrocatalytic activity of the CE, reaching a charge transfer resistance lower than 3 Ω cm² (with a I-based electrolyte), a value three times lower than conventional Pt. The authors also reached a high level of transparency greater than 90 % over the whole visible range (Table 11 entry 9).^[262] Ku et al. reported highly transparent NiS CE exceeding 90 % value and associated with both tri-iodide/iodide and sulfur-based redox mediators. In conjunction with the latter, they obtained a PCE of 6.25% (FF = 68%, R_{CT} = 2.4 Ω cm²) which is much better than the reference Pt-based counter electrodes (FF = 50%, R_{CT} = 48.2 Ω cm²). Additionally, the NiS electrode was proved to lose its catalytic activity with time due to the formation of Ni-thiolate bonds at the interface between NiS and the electrolyte.

Iron-based materials have also been explored. The hematite α-Fe₂O₃ has been showing ability to reduce triiodide

efficiently.^[277] However, its bandgap value of 2.1 eV leads to substantial light absorption in the visible range, thus not fulfilling one requisite for NIR-DSSCs. A similar issue arises when hematite is replaced with the pyrite FeS.^[278] The enhancement of the optical transparency of the iron-based CE can be obtained by the substitution of S with Se that allows enhancing the transmittance to almost 80% and remarkably high PCE approaching 10% (FF = 72%, RCT 5.5 Ω cm²) and 5.5% in front- and rear-illumination geometry (Table 11 entry 10).^[279]

Another interesting material for counter-electrodes is MoS₂. Although it is usually opaque, Kim et al. reported counter-electrodes based on 2D MoS₂ catalyst that can reach up to 80% transmittance after optimizing the thermal treatment.^[280] In this work is also highlighted the necessary trade-off between such high transparency and the device performance since high annealing temperature leads to poorer electrocatalytic activity (Table 11 entry 11). Jeong et al. reported a low-temperature approach below 100 °C using ALD to achieve semi-transparent CE (65% @ 555 nm), working as well as Pt standards in the presence of an I-based electrolyte (RCT = 4.75 Ω cm²), which can be used for bi-facial DSSC.^[281] When sulfur is replaced by selenium, the films are attaining a very high level of transparency above 85% with good electrocatalytic activity compared to I₃⁻/I⁻ redox couple (Table 11 entry 12).^[282] An interesting approach to tune the transparency of the hydrothermal CuSe₂ was proposed by Tang et al., who reported on the synthesis of CuSe at different pH and their simultaneous deposition of FTO: the most transparent electrode was obtained at a relatively low alkaline pH of 9 leading to transparency close to 100% after subtraction of the FTO transmittance (Table 11 entry 13).^[284] More recently, a transparent CE reaching 83% transmittance was developed by Ou et al. based on Cu_{2-x}Se@N-doped carbon nanosheets associated with the cobalt couple (i.e. tris(2,2'-bipyridine)-cobalt(II)/(III)) as the redox mediator for bifacial DSSC application and demonstrating good chemical stability (Table 11 entry 14).^[284]

Highly transparent CE has been first developed for bifacial DSSC applications. Very interesting results have been obtained in this field and this knowledge grasp is of particular inspiration for the selective NIR-DSSC. As an added value, some of them have also been designed to reduce both the synthetic steps and the production energy required in order to increase their sustainability and ecofriendliness. Albeit very high transparency (even close to 90%) (Figure 14) has been obtained, one should note that these CE have been optimized to work in conjugation with the standard iodine-based electrolyte. The absence of literature about the coupling of transparent CE and alternative redox mediator prevents us to draw very specific conclusions. Indeed, each redox mediator has its own electrochemistry and the CE should be tailored to assure the highest electrocatalytic behavior and the longest longevity. Among the different materials proposed, the most promising results have been obtained with carbon-based materials, especially graphene and its derivatives. They have also been proven to work properly with Co-based redox systems. However, importantly for the NIR-DSSC application, they often required a trade-off between transparency and catalytic activity. Very promising results have also been obtained with sulfide-based and selenide-based CE. The beneficial effect assured by their good catalytic properties

with respect to conventional I₃⁻/I⁻ based electrolyte combined to high optical transmittance could be jeopardized by stability issues when organic-based redox mediators are used. In the case of sulfide/thiolate redox couple, one should consider that the reduced species of the electrolyte could irreversibly bind on the CE surface leading to a dramatic decrease in cell performances. Similar issue could arise from the implementation of a metal based redox system, especially if there are based on atom with good affinity with S or Se, as copper, iron, and cobalt are.

3.5. Antireflective Coatings for NIR-DSSC

To achieve specifications in terms of transparency, antireflective coating (ARC) aims to reduce optical losses due to reflection (R) owing to refractive index mismatch between glass and air ($n_{\text{glass}} \approx 1.52$; $n_{\text{air}} = 1$) in agreement with Fresnel's law (Equation 10).^[286] The corresponding reflection in contact with air is 4.3% per interface, resulting in a total optical loss of 8.6% only by light reflection and solely considering the two external interfaces. Indeed, the same approximation with different values of reflection loss will apply inside the DSSC cell, through FTO/electrolyte, TiO₂/electrolyte interface, and CE/electrolyte interface.

Usually, ARC consists of a submicrometric layer thickness with the main function of accommodating the refractive index change between the two aforementioned media, thus minimizing light reflection to increase the cell's AVT and maximizing light transmission in the range of the dye's absorption to enhance PCE.

$$R = \frac{(1 - n_{\text{glass}})^2}{(1 + n_{\text{glass}})^2} \quad (26)$$

Typically, ARCs can reduce the reflection per interface down to 1% level, thus increasing the transmission by 7–8%. ARCs can be categorized into three main types: single layer (SLARC), multilayers (MLARC), and “moth-eye.” For successful integration of the ARC, pores with a diameter in the range of the incident wavelength should be avoided accordingly to the Mie-scattering theory. Single-layer ARC consists of a layer of material with controlled thickness and refractive index value between the air's and substrate's ones resulting from its chemical nature or porosity (Figure 15a-1-4). Multilayers ARC relies upon the successive use of different materials of various refractive indexes to cumulatively reduce reflection at different wavelengths (Figure 15b). In some cases, MLARC is achieved by depositing layers while gradually tuning the refractive index, generating a gradient of refractive index (Figure 15c-5). Another possibility to form such a gradient consists of the periodic nano-texturation of the ARC, by imitating the surface structure of a moth-eye (Figure 15c-6).

For a SLARC, the total thickness (d) is crucial to obtain destructive interferences between the reflected light between air/ARC interface and ARC/substrate interface. For this, a so-called “quarter wave” layer is needed following Equation 27:

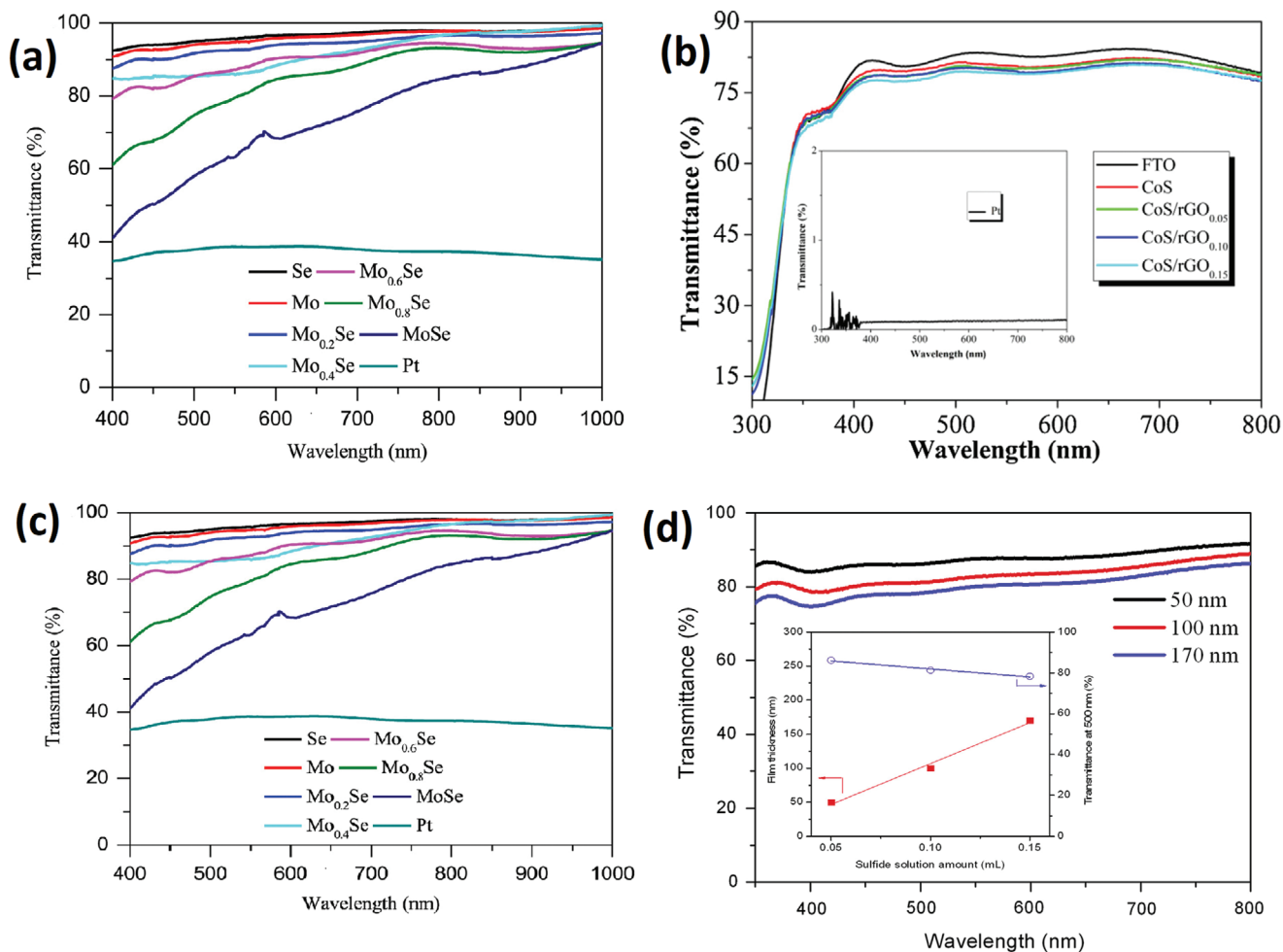


Figure 14. Transmittance curves of CE films based on a) CoSe^[278] b) CoS/rGo composites^[267] c) MoSe^[279] and d) NiS.^[280] a) Reproduced with permission.^[278] Copyright 2014, American Chemical Society. b) Reproduced with permission.^[267] Copyright 2016, Elsevier. c) Reproduced with permission.^[279] Copyright 2015, Elsevier. d) Reproduced with permission.^[280] Copyright 2015, Elsevier.

$$n_{arc} \times d = \frac{\lambda}{4} \quad (27)$$

The simplified Fresnel equation at the air/ARC interface enables the calculation of the best ARC refractive index to abate light reflection following Equation 28:^[287,288]

$$n_{arc} = \sqrt{n_{air} \times n_{sub}} \quad (28)$$

Therefore, in the case of selective NIR-DSSC, an efficient SLARC can be designed with a material exhibiting a refractive index of 1.23 and a thickness of 114 nm (**Figure 16**).

The ARCs can be elaborated with polymer-based materials, inorganic compounds, or a mix of these two.^[289–291]

Polymers have been widely discussed in the literature due to their processability, low cost, flexibility, and their tunable refractive indexes.^[292,293] A well-known strategy consists of increasing the film's porosity following the volume averaging theory, which relates the volume of voids in the film and its refractive index by Equation 29:^[294–296]

$$n_{pc} = \left[\left(1 - \frac{P}{100} \right) (n_{dc}^2 - 1) + 1 \right]^{1/2} \quad (29)$$

Where n_{pc} and n_{dc} are the refractive index of the pores (air) and nonporous material, respectively, and P is the porosity of the layer.

Another approach for nanoporous ARC film is the use of polymer colloids such as PMMA (poly methyl methacrylate),^[299,300] PTFEMA (poly(2,2,2-trifluoroethyl methacrylate))^[301] or a mixture of PS (polystyrene) and PMMA.^[300] After depositing by spin-coating, a gain of around 4% in transmittance has been reported regardless of the type of polymer used. However, although this type of ARC is optically optimal, this polymer technology suffers from a lack of long-term stability under UV irradiation and lack of mechanical adhesion to the glass surface.

These drawbacks can be tackled by replacing the polymer with inorganic materials deposited either by vacuum process,^[302] chemical vapor deposition,^[303] or wet processing like sol-gel.^[304,305] Unfortunately, a simple quarter-wave ARC cannot be totally fulfilled because the lowest refractive index

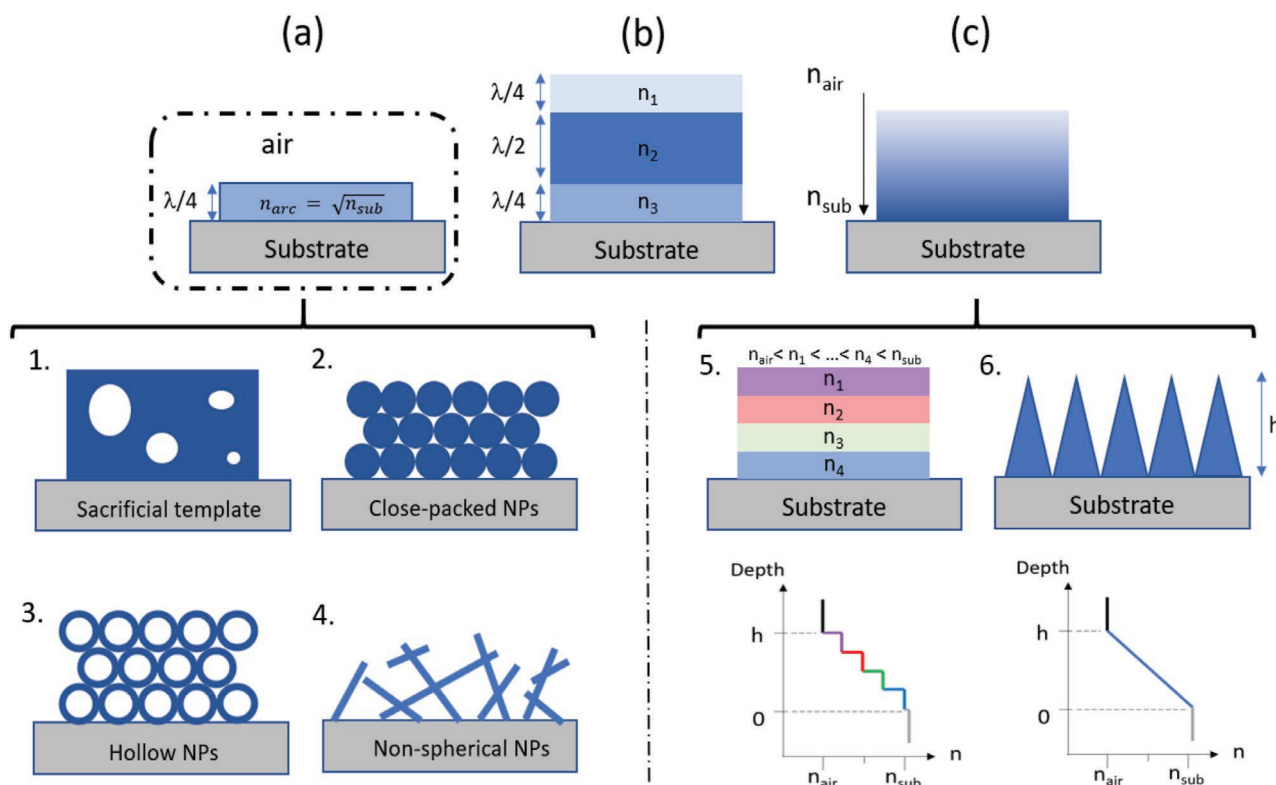


Figure 15. Schematic illustration of different existing categories of ARCs: a) Quarter-wave SLARCs, b) multilayer interference coating, and c) gradient-index ARCs. Gradient-index ARCs can be subcategorized in MLARCs (c).5. and “Moth-eyes” like (c).6. textures with their associated gradient of the refractive index profile.

of inorganic material is $n = 1.38$ for MgF_2 . In this case, it is required the formation of multilayer ARCs (see Figure 15a,b) or the implementation of nano-objects or nanotexturization to minimize further the light reflection.^[292] However, the vacuum process of MgF_2 is not compatible with DSSC fabrication which requires a post-annealing treatment at ca. 450°C , a temperature

well above the thermal stability limit of amorphous MgF_2 . It is also not totally compatible with an end process for DSSC because the high vacuum level will challenge the sealing retaining the liquid electrolyte. Based on these technical limitations, one of the simplest approaches consists of the deposition of silica nanospheres by spin-coating even though SiO_2

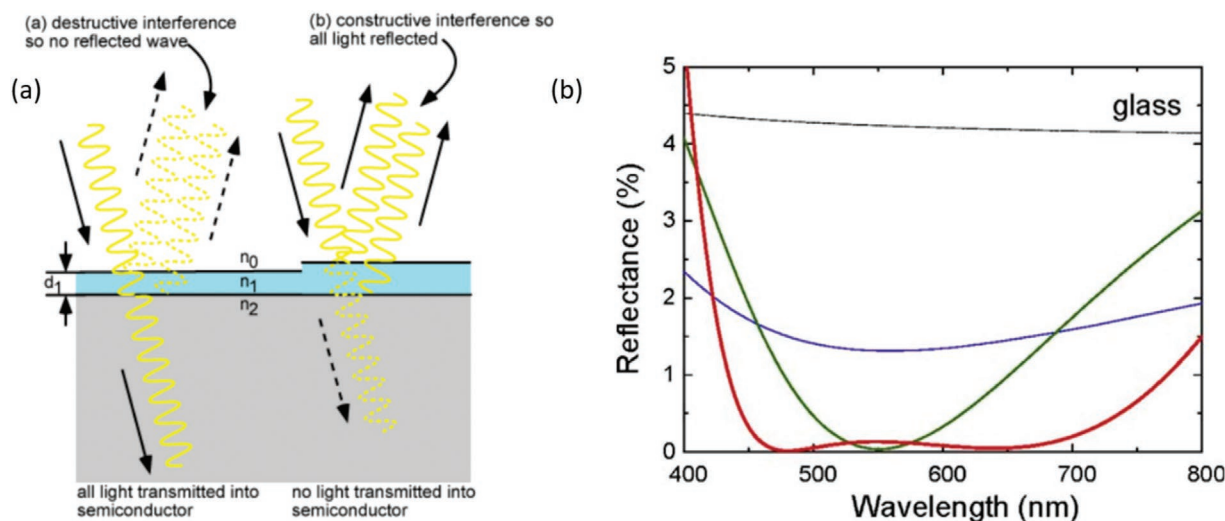


Figure 16. a) Operative principle of a quarter-wave SLARCs. Reproduced under the terms of use of ref. [297] Copyright 2019. C.B. Honsberg and S.G. Bowden and b) reflectance as a function of wavelength for ARCs (air/glass)]. Blue curve: SLARC made of $1/4 \text{MgF}_2$; green curve: quarter-quarter Arcs made of $1/4 \text{MgF}_2$, $1/4 \text{Al}_2\text{O}_3$. Red curve: three layers ARCs made of $1/4 \text{MgF}_2$, $1/2 \text{ZrO}_2$, $1/4 \text{Al}_2\text{O}_3$. Reproduced with permission.^[298] Copyright 2010, Elsevier.

has not the optimal refractive index with a value of 1.45 in the visible range.^[306,307] Once deposited, they can form a layer with a different level of random/organized arrangement depending on the deposition technique and conditions. Once annealed, those NPs form a 3D network with a porosity ranging from 26% to more than 75% depending on the particles size, morphology, spatial arrangement of NPs, and the concentration of binding molecules added in the colloidal solution.^[308–311] To achieve a medium refractive index of 1.23, a porosity of 53% is needed.^[292] In that way, Li et al. have elaborated a protocol to synthesize SiO₂ NPs of 100 nm diameter followed by a spin-coating step that allows forming a monolayer of NPs at the surface of a DSSC (see Figure 16a).^[312] In that ideal conditions, and in addition to an internal ARC made of ZnO NPs at the FTO/TiO₂ interface, the authors reported a transmittance gain in the whole visible and NIR range by 5%, resulting in a gain of J_{sc} from 10 to 12 mA cm⁻² and an increase of PCE by 5.8% with N719 dye. Naim et al. have recently demonstrated the possibility of reproducing this protocol with VG20-C₁₆.^[25] By applying SiO₂ ARC on both sides of a transparent selective NIR-DSSC, they managed to measure a significant increase of transparency in the visible and NIR region based on a 3.8 μm thick TiO₂ photoanode. The AVT value increased from 70% to 76%, thus demonstrating the relevance of ARC deposition for NIR-DSSC application. The PCE was also slightly enhanced as a result of the improved transmittance in the NIR region (Figure 17c). Unfortunately, the mechanical stability of such layer remains low due to the high porosity. Chen et al. have addressed this important issue by forming inter-NPs chemical bonds once deposited on the substrate thanks to hydroxylation of silica surfaces in presence of H₂O₂.^[313] Another option relies on adding an organic binder such as polypropylene glycol, which

can tune the medium refractive index as expected from the effective model theory^[314,315] in the range of 1.13 to 1.34.^[316,317] A complementary approach relies on tailoring the morphology of the nanoparticles, for instance through hollow-nano-objects.^[292,313,318–320]

More recently, focus has been given on new biosourced material for SLARCs for DSSC such as cellulose or chitin NCs or nanofibers. To our knowledge, the only application on NIR-DSSC consists in chitin nanoneedles obtained from shrimp wastes recycling. By spin-coating a thin layer of ca. 100–200 nm chitin NCs, we have measured on a complete NIR-DSSC based on VG20-C₁₆, a gain of transmittance in the visible and NIR range affording a J_{sc} gain from 11.4 to 12.7 mA cm⁻² leading to an enhancement of PCE from 2.6% to 2.8% (Figure 17). We also demonstrated an AVT increase of 3.1%.

As the FTO/TiO₂ interface also contributes to the total light losses in DSSC, some ARCs research also focused on this interface, particularly through nanometric coating made of ZnO^[312] or ZnSnO₄.^[321] Additionally, electrolyte based on acetonitrile allows reducing substantially reflections occurring at FTO/ electrolyte and TiO₂/electrolyte interfaces as modeled by Wenger et al., due to its low refractive index in the visible and NIR range ($n \approx 1.35$) in comparison to FTO ($n \approx 2.0–1.7$) and TiO₂ ($n \approx 2.0–1.8$).^[322]

MLARCs can consist of a periodic multilayer quarter-wave coating or a multilayer stacking of materials with different refractive indexes, alternating high and low (photonic bandgap crystals) or gradually increasing according to a gradient.^[323]

In the simplest design (quarter-quarter stack),^[324] the external layer is made of a lower refractive index material in comparison with the internal layer (in contact with the substrate). The

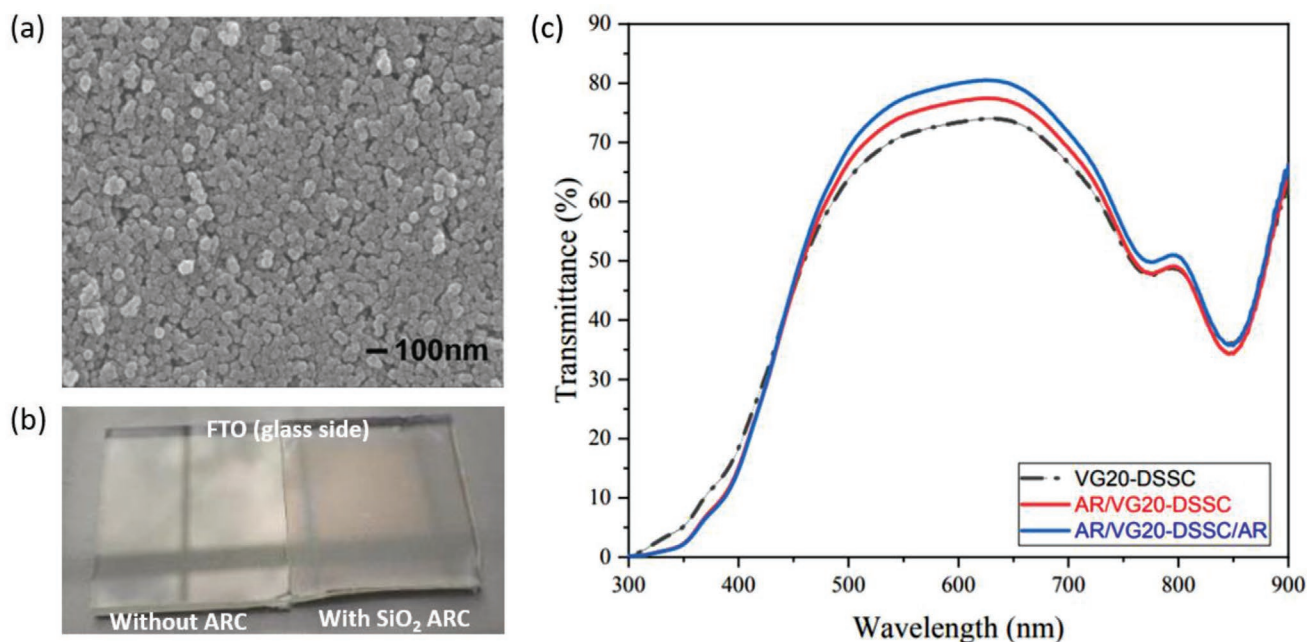


Figure 17. a) SEM pictures of 100 nm SiO₂ NPs deposited on a glass substrate by spin-coating. Reproduced with permission.^[312] Copyright 2019, Elsevier. b) Photography of FTO substrate (glass side) exposed under sunlight with and without SiO₂ ARC (1 monolayer of NPs, 100 nm). c) Comparison of total transmittance of a complete DSSC (dye = VG20-C₁₆) with and without SiO₂ ARC (1 monolayer of NPs, ≈ 100 nm per glass/air interface). Reproduced with permission.^[25] Copyright 2021, American Chemical Society.

reflection plot as a function of the refractive index presents for this kind of “quarter-quarter” MLARCs a typical “V” shape curve with a distinct minimum (Figure 16b). The optimal refractive index for these two layers can be calculated (for a targeted wavelength) following Equation 30:

$$\frac{1}{n_{\text{sub}}} = \left(\frac{n_L}{n_H} \right)^2 \quad (30)$$

where n_L and n_H are the refractive indexes of the low and high refractive index coatings, respectively. An example of quarter-quarter MLARCs can be with an external layer (on air interface) made of MgF_2 ($n = 1.38$) and an internal layer (on glass interface) made of CeF_3 ($n = 1.65$) or Al_2O_3 ($n = 1.76$).^[298]

To minimize reflections on a broader wavelength range broad band ARC (BBARC)^[324] were studied by introducing a third layer (called “absentee layer” composed of a dielectric material with a thickness equal to $\lambda/2$) in between the two quarter-quarter layers. Based on Fresnel’s theory, the continuous transition of refractive index from 1 to 1.5 (no steep walk contrary to SLARCs) is mandatory to achieve BBARC from visible to NIR range. Such a BBARC can consist of an external layer made of MgF_2 ($n = 1.38$), an intermediate layer made of ZrO_2 ($n = 2.1$) and an internal layer made of CeF_3 ($n = 1.65$) or Al_2O_3 ($n = 1.76$) (Figure 16b).^[298]

Ulusoy et al.^[290] have reported a MLARCs based on ORganically MODified SILlica (ORMOSIL). Tuning the porosity of this coating^[325,326] decreases progressively the refractive index of successive layers resulting in a gain in light transmission in the visible range in between 2% and 5% for a single FTO substrate. The same authors also measure a significant increase of 23% for the J_{sc} on a working DSSC based on N719 dye.

As aforementioned, hollow structure are used to prepare low refractive layer^[327] and MgF_2 is a very interesting material for ARCs as it presents the lowest refractive index among inorganic materials ($n = 1.38$).^[328,329] Bao et al.^[313] have achieved an ARC consisting of a bottom layer made of chemically bonded silica nanoparticles and a top layer made of hollow MgF_2 nanorods with a refractive index that can be adjusted from 1.10 to 1.35. Another design of ARCs is “Moth-eye” like texture; able to limit reflection due to the presence of a spatially ordered array of sub-micrometric dots. In other words, this strategy consists of the formation of a periodic framework directly on the glass substrate. Many types of geometry have been studied, such as nanohemisphere, cones, and pyramidal.^[298] When incident light penetrates this lattice, the refractive index progressively enhances due to the increased volume ratio of material/air with depth. The geometric profile of the “dots” directly determines the refractive index gradient profile. Those dots are usually formed by top-down techniques such as ion-beam etching,^[330] template imprinting,^[331] and NPs assembly/sintering.^[332]

Kim et al.^[333] have illustrated a route to creating a “moth-like” ARCs via photolithography of a “hard” silicon master, which then can be replicated by deposition and reticulation of a “soft” layer of PDMS (Poly dimethyl siloxane). After removing the template, a textured PDMS film is obtained with a gradient of refractive index from 1 to 1.43. Optimal reduction of R (4.3% compared to the reference value of 7.9%) has been measured for pores-radius of 300 nm while presenting a good

transmittance in NIR, interesting for increasing the PCE and AVT of NIR-DSSC. An interesting example applied directly on DSSC with N3 dye has been highlighted by Tsai and Tu,^[334] showing a gain of transmittance of 5% from 400 to 800 nm with a gain in PCE leading to 6.8% through a moth-eyes sub-micrometric PMMA ARC. Lim et al.^[335] or Heo et al.^[336] were providing other examples consisting of a reduction of reflectance of ca. 3% and between 5%–10% respectively in the whole visible range by forming moth-eyes ARCs made of PDMS or PTFE, respectively. In both cases, the final PCE of DSSC based on N719 was demonstrated.

Regardless of the transparency gain achieved, many authors have pointed the two major disadvantages of current ARCs. For polymer-based and nanotextured ones, mechanical strength and durability versus external conditions such as solar irradiation are important issues. For MLARCs, their elaboration via multistep process (coating, curing steps, etc) can reach a high cost. Considering photovoltaic applications, one should weight the pros and cons and emphasize a low-cost and efficient ARC that is easily applicable to high volumes and for large substrates.

4. Conclusions and Prospects

The emergence of TPV represents a new opportunity for DSSC. The current state of the art for NIR selective technologies, luminescent solar concentrators being the more transparent and organic PV having the highest efficiency reported so far. However, the interest in NIR-DSSC stands in their ability to reach high transparency as recently demonstrated by our group and the possibility of reaching efficiencies close to the theoretical 10.8% calculated by Lunt. For the future of this technology, the main effort should be targeting the improvement of the PCE. The current state of the art provides detailed information regarding which are the main limitations for NIR-DSSC as already discussed in this review. We can estimate that a fully optimized selective NIR-DSSC can reach a maximum PCE value of ca. 8%. This value has been calculated, estimating that the maximum photocurrent density achievable would be ca. 13 mA cm⁻² considering the total sun photon flux between 350 to 420 nm and 750 to 950 nm. We can estimate realizable to reach a cell photovoltage of ca. 0.8 V considering an electrolyte based on a redox mediator in the range of 0.65 V vs. NHE and a fill factor value of 75%.

With this review, we intend to provide the reader a full understanding of color perception and its evaluation. When it comes to the aesthetic assessment of TPV, to our knowledge, there are different metrics that can be applied other than the ones presented in the main text. Therefore, we find it important to introduce other evaluation methods that can help extend the applicability of the technology in the market and compare it with other emerging TPV.

In evaluating the CRI two important metrics are obtained, which help identify the position of the test sample on the CIE color space, x and y in the CIE 1931 known as chromaticity coordinates and u and v in the CIE 1976, known as uniform chromaticity coordinates. On the perimeter of the chromaticity diagram, it is also possible to define the dominant wavelength which helps relating the final coloration of

the test sample to a monochromatic color. It is determined by drawing a straight line from the equal-energy point ($x_{ee} = y_{ee} = 1/3$) to the chromaticity coordinates of the test sample and by then extending this straight line to the perimeter of the chromaticity diagram.^[337] Once the dominant wavelength is known, the next step in the characterization is the evaluation of the color purity (saturation), which is given by the distance in the chromaticity diagram between the chromaticity coordinates of the investigated sample and the coordinates of the equal-energy point of the sample divided by the distance between the equal-energy point and the dominant wavelength point:

$$\text{Color purity } (P_c) = \frac{\sqrt{(x - x_{ee})^2 + (y - y_{ee})^2}}{\sqrt{(x_d - x_{ee})^2 + (y_d - y_{ee})^2}} \quad (31)$$

where (x_d, y_d) , (x_{ee}, y_{ee}) and (x, y) are the chromaticity coordinates of the dominant wavelength, equal-energy point, and the tested sample, respectively. The final value of P_c varies between 0 and 1, representing respectively a pale color when the point is close to the reference white and highly saturated color when close to the purple boundary.^[26]

In this same color space, it is possible to project the black body locus, representing the color variation of a black body with the temperature (Figure 18). This results in another important metric in the color evaluation named the correlated color temperature (CCT) associated with the light source's tone. Each temperature corresponds to one tone and is specified in degrees Kelvin. The CCT value is calculated from McCamy's equation reported below (Equation 16)^[338] and it allows understanding of whether the color is neutral, bluish white, or reddish white.^[22]

$$\text{CCT} = 449n^3 + 3525n^2 + 6823.3n + 5520.33 \quad (32)$$

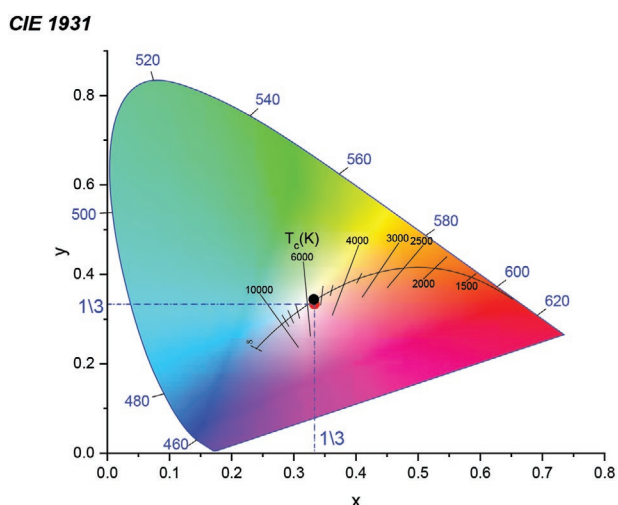


Figure 18. CIE 1931 chromaticity space projecting black body locus (black line), the $x = y = 1/3$ position in red and A.M. 1.5G illuminant position in black.

where $n = \frac{(x - 0.3320)}{(0.1858 - y)}$ and x and y being the chromaticity coordinates in the CIE 1931 color space.

To further complete the aesthetic assessment of the aforementioned parameters, we also find it important to define the suitable standard illuminants, which have the role in portraying illumination conditions and are defined by the CIE. For this aim, we define the white point of an illuminant in the chromaticity diagram, which coordinates in the CIE space are obtained by illuminating a white object with the reference illuminant of choice. By changing the white point, one can partially compensate for changes due to the color of the illuminant. Typical white points used in color evaluation are the equal energy point ($x_{ee} = y_{ee} = 1/3$) and the D_{65} illuminant (x_{65}, y_{65}) = (0.3112, 0.3371) which is a representation of the average daylight. In order to simulate the color perception through the TPV with an incandescent bulb as the illumination source (the case of internal lightning condition), the CIE standardizes the illuminant A, which represents a tungsten-filament lamp operating at CCT of 2856 K. With the final aim of using TPV technologies for building integration, we highly recommend using A.M. 1.5G as standard illuminant, which is characterized by a CCT value of 5513 K.

Acknowledgements

F.G. and M.B. contributed equally to this work. The authors acknowledge financial support from "IMPRESSIVE" project which received funding from the European Union's Horizon2020 research and innovation program under grant agreement number n°826013. W.N. and F.S. thank the financial support from the Agence Nationale de la Recherche (ANR) "VISION-NIR" program under grant agreement number ANR-17-CE05-0037. T.T. acknowledges the financial support from Spanish MINECO (CTQ2017-85393-P (Phthalophoto), PID2020-116490GB-I00 (Porphyrinoids)) and ERA-NET/European Commission/MINECO, (UNIQUE, SOLAR-ERA.NET Cofound 2 N° 008/ PCI2019-111889-2. IMDEA Nanociencia acknowledges support from the "Severo Ochoa" Programme for Centres of Excellence in R&D (MINECO, Grant SEV2016-0686). W.N., F.G., and F.S. thank Prof. A. Di Carlo, Dr. F. Matteocci, and Dr. D. Rossi from University Tor Vegata for fruitful discussion on AVT, CRI, and CCT assessment. A.A.T. acknowledges Grant of the President of Russia for Young Scientists MK-1702.2020.3.

Conflict of Interest

The authors declare no conflict of interest.

Keywords

colorless dye-sensitized solar cells, colorless electrolytes, NIR-dyes, sustainable transparent photovoltaics, transparent counter electrodes

Received: May 22, 2021

Revised: July 7, 2021

Published online:

- [1] SolarPower Europe, EU Market Outlook for Solar Power 2020–2024, **2020**, <https://www.solarpowereurope.org/> (accessed: May 2021).
- [2] C. Kim, K. S. Kim, H. Y. Kim, Y. S. Han, *J. Mater. Chem.* **2008**, *18*, 5809.
- [3] G. E. Eperon, D. Bryant, J. Troughton, S. D. Stranks, M. B. Johnston, T. Watson, D. A. Worsley, H. J. Snaith, *J. Phys. Chem. Lett.* **2015**, *6*, 129.
- [4] X. Zhang, G. E. Eperon, J. Liu, E. M. J. Johansson, *Nano Energy* **2016**, *22*, 70.
- [5] M. Saifullah, S. Ahn, J. Gwak, S. Ahn, K. Kim, J. Cho, J. H. Park, Y. J. Eo, A. Cho, J. S. Yoo, J. H. Yun, *J. Mater. Chem. A* **2016**, *4*, 10542.
- [6] J. W. Lim, D. J. Lee, S. J. Yun, *ECS Solid State Lett.* **2013**, *2*, Q47.
- [7] F. Guo, H. Azimi, Y. Hou, T. Przybilla, M. Hu, C. Bronnbauer, S. Langner, E. Spiecker, K. Forberich, C. J. Brabec, *Nanoscale* **2015**, *7*, 1642.
- [8] E. Della Gaspera, Y. Peng, Q. Hou, L. Spiccia, U. Bach, J. J. Jasieniak, Y. B. Cheng, *Nano Energy* **2015**, *13*, 249.
- [9] R. R. Lunt, *Appl. Phys. Lett.* **2012**, *101*, 043902.
- [10] R. R. Lunt, V. Bulovic, *Appl. Phys. Lett.* **2011**, *98*, 113305.
- [11] C. C. Chen, L. Dou, R. Zhu, C. H. Chung, T. B. Song, Y. B. Zheng, S. Hawks, G. Li, P. S. Weiss, Y. Weiss, *ACS Nano* **2012**, *6*, 7185.
- [12] C. J. Traverse, R. Pandey, M. C. Barr, R. R. Lunt, *Nat. Energy* **2017**, *2*, 849.
- [13] Y. Zhao, G. A. Meek, B. G. Levine, R. R. Lunt, *Adv. Opt. Mater.* **2014**, *2*, 606.
- [14] ASTM G173-03(2020), Standard Tables for Reference Solar Spectral Irradiances: Direct Normal and Hemispherical on 37° Tilted Surface, **2020**, <https://www.astm.org/Standards/G173.html> (accessed: June 2021).
- [15] B. O'Regan, M. Gratzel, *Nature* **1991**, *353*, 737.
- [16] A. Hagfeldt, G. Boschloo, L. Sun, L. Kloo, H. Pettersson, *Chem. Rev.* **2010**, *110*, 6595.
- [17] D. Saccone, S. Galliano, N. Barbero, P. Quagliotto, G. Viscardi, C. Barolo, *Eur. J. Org. Chem.* **2016**, *2016*, 2244.
- [18] C. Martín, M. Ziótek, A. Douhal, *J. Photochem. Photobiol. C: Photochem. Rev.* **2016**, *26*, 1.
- [19] R. Katoh, A. Furube, *J. Photochem. Photobiol. C: Photochem. Rev.* **2014**, *20*, 1.
- [20] J. Bisquert, F. Fabregat-Santiago, in *Dye-Sensitized Solar Cells*, 1st ed., ImprintEPFL Press **2010**, p. 423.
- [21] A. Roy, A. Ghosh, S. Bhandari, P. Selvaraj, S. Sundaram, T. K. Mallick, *J. Phys. Chem. C* **2019**, *123*, 23834.
- [22] A. Ghosh, P. Selvaraj, S. Sundaram, T. K. Mallick, *Sol. Energy* **2018**, *163*, 537.
- [23] K. Zhang, C. Qin, X. Yang, A. Islam, S. Zhang, H. Chen, L. Han, *Adv. Energy Mater.* **2014**, *4*, 1.
- [24] Q. Huaiulmé, V. M. Mwalukuku, D. Joly, J. Liotier, Y. Kervella, P. Maldivi, S. Narbey, F. Oswald, A. J. Riquelme, J. A. Anta, R. Demadrille, *Nat. Energy* **2020**, *5*, 468.
- [25] W. Naim, V. Novelli, I. Nikolinakos, N. Barbero, I. Dzeba, F. Grifoni, Y. Ren, T. Alnasser, A. Velardo, R. Borrelli, S. Haacke, S. M. Zakeeruddin, M. Graetzel, C. Barolo, F. Sauvage, *JACS Au* **2021**, *1*, 409.
- [26] M. R. Hunt, R. W. G. Pointer, *Measuring Colour*, John Wiley & Sons Inc., Chichester, UK **2011**.
- [27] D. L'Eclairage, *Comm. Int. L'Eclairage, Vienna, Austria* **1995**.
- [28] N. Ohta, A. Robertson, *Colorimetry: Fundamentals and Applications*, Vol. 30, John Wiley & Sons, New York **2006**.
- [29] C. Yang, D. Liu, M. Bates, M. C. Barr, R. R. Lunt, *Joule* **2019**, *3*, 1803.
- [30] K. Pydzińska, M. Ziótek, *Dyes Pigm.* **2015**, *122*, 272.
- [31] M. Ziótek, J. Karolczak, M. Zalas, Y. Hao, H. Tian, A. Douhal, *J. Phys. Chem. C* **2014**, *118*, 194.
- [32] O. Bräm, A. Cannizzo, M. Chergui, *Phys. Chem. Chem. Phys.* **2012**, *14*, 7934.
- [33] T. Yoshihara, R. Katoh, A. Furube, M. Murai, Y. Tamaki, K. Hara, S. Murata, H. Arakawa, M. Tachiya, *J. Phys. Chem. B* **2004**, *108*, 2643.
- [34] M. J. Marchena, G. De Miguel, B. Cohen, J. A. Organero, S. Pandey, S. Hayase, A. Douhal, *J. Phys. Chem. C* **2013**, *117*, 11906.
- [35] M. K. Nazeeruddin, P. Péchy, T. Renouard, S. M. Zakeeruddin, R. Humphry-Baker, P. Cointe, P. Liska, L. Cevey, E. Costa, V. Shklover, L. Spiccia, G. B. Deacon, C. A. Bignozzi, M. Grätzel, *J. Am. Chem. Soc.* **2001**, *123*, 1613.
- [36] A. Abbotto, F. Sauvage, C. Barolo, F. De Angelis, S. Fantacci, M. Graetzel, N. Manfredi, C. Marinzi, M. K. Nazeeruddin, *Dalton Trans.* **2011**, *40*, 234.
- [37] S. Altobello, R. Argazzi, S. Caramori, C. Contado, S. Da Fré, P. Rubino, C. Choné, G. Larramona, C. A. Bignozzi, *J. Am. Chem. Soc.* **2005**, *127*, 15342.
- [38] A. Baumann, C. Curia, J. H. Delcamp, *ChemSusChem* **2020**, *13*, 2503.
- [39] J. Park, G. Viscardi, C. Barolo, N. Barbero, *Chimia* **2013**, *67*, 129.
- [40] T. Higashino, Y. Kurumisawa, S. Nimura, H. Iiyama, H. Imahori, *Eur. J. Org. Chem.* **2018**, *2018*, 2537.
- [41] W. M. Campbell, A. K. Burrell, D. L. Officer, K. W. Jolley, *Coord. Chem. Rev.* **2004**, *248*, 1363.
- [42] Y. Fu, T. Lu, Y. Xu, M. Li, Z. Wei, H. Liu, W. Lu, *Dyes Pigm.* **2018**, *155*, 292.
- [43] Ö. Birel, S. Nadeem, H. Duman, *J. Fluoresc.* **2017**, *27*, 1075.
- [44] C. Encinas, E. Otazo, L. Rivera, S. Miltsov, J. Alonso, *Tetrahedron Lett.* **2002**, *43*, 8391.
- [45] Z. Li, Z. hui Jin, K. Kasatani, H. Okamoto, *Phys. B: Condens. Matter* **2006**, *382*, 229.
- [46] L. Zhang, J. M. Cole, *J. Mater. Chem. A* **2017**, *5*, 19541.
- [47] Z. Yan, S. Guang, X. Su, H. Xu, *J. Phys. Chem. C* **2012**, *116*, 8894.
- [48] C. H. Chang, Y. C. Chen, C. Y. Hsu, H. H. Chou, J. T. Lin, *Org. Lett.* **2012**, *14*, 4726.
- [49] J. H. Yum, P. Walter, S. Huber, D. Rentsch, T. Geiger, F. Nüesch, F. De Angelis, M. Grätzel, M. K. Nazeeruddin, *J. Am. Chem. Soc.* **2007**, *129*, 10320.
- [50] T. Geiger, S. Kuster, J.-H. Yum, S.-J. Moon, M. K. Nazeeruddin, M. Grätzel, F. Nüesch, *Adv. Funct. Mater.* **2009**, *19*, 2720.
- [51] S. Kuster, F. Sauvage, M. K. Nazeeruddin, M. Grätzel, F. A. Nüesch, T. Geiger, *Dyes Pigm.* **2010**, *87*, 30.
- [52] T. Maeda, Y. Hamamura, K. Miyamura, N. Shima, S. Yagi, H. Nakazumi, *Org. Lett.* **2011**, *13*, 5994.
- [53] T. Maeda, S. Arikawa, H. Nakao, S. Yagi, H. Nakazumi, *New J. Chem.* **2013**, *37*, 701.
- [54] C. Magistris, S. Martiniani, N. Barbero, J. Park, C. Benzi, A. Anderson, C. H. Law, C. Barolo, B. O'Regan, *Renewable Energy* **2013**, *60*, 672.
- [55] T. Maeda, S. Nitta, Y. Sano, S. Tanaka, S. Yagi, H. Nakazumi, *Dyes Pigm.* **2015**, *122*, 160.
- [56] J. Park, C. Barolo, F. Sauvage, N. Barbero, C. Benzi, P. Quagliotto, S. Coluccia, D. Di Censo, M. Grätzel, M. K. Nazeeruddin, G. Viscardi, *Chem. Commun.* **2012**, *48*, 2782.
- [57] T. Maeda, S. Mineta, H. Fujiwara, H. Nakao, S. Yagi, H. Nakazumi, *J. Mater. Chem. A* **2013**, *1*, 1303.
- [58] J. Park, N. Barbero, J. Yoon, E. Dell'Orto, S. Galliano, R. Borrelli, J.-H. Yum, D. Di Censo, M. Grätzel, M. K. Nazeeruddin, C. Barolo, G. Viscardi, *Phys. Chem. Chem. Phys.* **2014**, *16*, 24173.
- [59] C. Qin, Y. Numata, S. Zhang, X. Yang, A. Islam, K. Zhang, H. Chen, L. Han, *Adv. Funct. Mater.* **2014**, *24*, 3059.
- [60] P. F. Santos, L. V. Reis, P. Almeida, A. S. Oliveira, L. F. Vieira Ferreira, *J. Photochem. Photobiol. A: Chem.* **2003**, *160*, 159.
- [61] S. Galliano, V. Novelli, N. Barbero, A. Smarra, G. Viscardi, R. Borrelli, F. Sauvage, C. Barolo, *Energies* **2016**, *9*, 486.

- [62] A. Ehret, L. Stuhl, M. T. Spitzer, *J. Phys. Chem. B* **2001**, *105*, 9960.
- [63] G. Pepe, J. M. Cole, P. G. Waddell, S. McKechnie, *Mol. Syst. Des. Eng.* **2016**, *1*, 86.
- [64] W. Wu, F. Meng, J. Li, X. Teng, J. Hua, *Synth. Met.* **2009**, *159*, 1028.
- [65] T. Ono, T. Yamaguchi, H. Arakawa, *Sol. Energy Mater. Sol. Cells* **2009**, *93*, 831.
- [66] K. Sayama, S. Tsukagoshi, T. Mori, K. Hara, Y. Ohga, A. Shinpou, Y. Abe, S. Suga, H. Arakawa, *Sol. Energy Mater. Sol. Cells* **2003**, *80*, 47.
- [67] K. Funabiki, H. Mase, A. Hibino, N. Tanaka, N. Mizuhata, Y. Sakuragi, A. Nakashima, T. Yoshida, Y. Kubota, M. Matsui, *Energy Environ. Sci.* **2011**, *4*, 2186.
- [68] T. Geiger, I. Schoger, D. Rentsch, A. C. Véron, F. Oswald, T. Meyer, F. Nüesch, *Int. J. Photoenergy* **2014**, *2014*, 258984.
- [69] M. Urbani, G. De La Torre, M. K. Nazeeruddin, T. Torres, *Chem. Soc. Rev.* **2019**, *48*, 2738.
- [70] C. C. Lever, A. B. P. Lever, in *Phthalocyanines, Properties and Applications*, Vol. 1–4, (Eds: C. C. Leznoff, A. B. P. Lever), Wiley VCH, New York **1997**.
- [71] Y. C. Shen, L. Wang, Z. Lu, Y. Wei, Q. Zhou, H. Mao, H. Xu, *Thin Solid Films* **1995**, *257*, 144.
- [72] M. K. Nazeeruddin, R. Humphry-Baker, M. Grätzel, D. Wöhrle, G. Schnurpfel, G. Schneider, A. Hirth, N. Trombach, *J. Porphyrins Phthalocyanines* **1999**, *3*, 230.
- [73] J.-J. Cid, J.-H. Yum, S.-R. Jang, M. K. Nazeeruddin, E. Martínez-Ferrero, E. Palomares, J. Ko, M. Grätzel, T. Torres, *Angew. Chem.* **2007**, *119*, 8510.
- [74] P. Y. Reddy, L. Giribabu, C. Lyness, H. J. Snaith, C. Vijaykumar, M. Chandrasekharan, M. Lakshmikantham, J. H. Yum, K. Kalyanasundaram, M. Grätzel, M. K. Nazeeruddin, *Angew. Chem., Int. Ed.* **2007**, *46*, 373.
- [75] S. Mori, M. Nagata, Y. Nakahata, K. Yasuta, R. Goto, M. Kimura, M. Taya, *J. Am. Chem. Soc.* **2010**, *132*, 4054.
- [76] M. Ince, R. Kuboi, T. Ince, K. Yoshimura, D. Motoyoshi, M. Sonobe, R. Kudo, S. Mori, M. Kimura, T. Torres, *Sustainable Energy Fuels* **2021**, *5*, 584.
- [77] M. Kimura, H. Nomoto, N. Masaki, S. Mori, *Angew. Chem., Int. Ed.* **2012**, *51*, 4371.
- [78] M. Kimura, H. Nomoto, H. Suzuki, T. Ikeuchi, H. Matsuzaki, T. N. Murakami, A. Furube, N. Masaki, M. J. Griffith, S. Mori, *Chem. Eur. J.* **2013**, *19*, 7496.
- [79] H. Matsuzaki, T. N. Murakami, N. Masaki, A. Furube, M. Kimura, S. Mori, *J. Phys. Chem. C* **2014**, *118*, 17205.
- [80] T. Ikeuchi, H. Nomoto, N. Masaki, M. J. Griffith, S. Mori, M. Kimura, *Chem. Commun.* **2014**, *50*, 1941.
- [81] M. E. Ragoussi, J. J. Cid, J. H. Yum, G. De La Torre, D. Di Censo, M. Grätzel, M. K. Nazeeruddin, T. Torres, *Angew. Chem., Int. Ed.* **2012**, *51*, 4375.
- [82] M. E. Ragoussi, J. H. Yum, A. K. Chandiran, M. Ince, G. De La Torre, M. Grätzel, M. K. Nazeeruddin, T. Torres, *ChemPhysChem* **2014**, *15*, 1033.
- [83] M. Urbani, M. Grätzel, M. K. Nazeeruddin, T. Torres, *Chem. Rev.* **2014**, *114*, 12330.
- [84] S. Mathew, A. Yella, P. Gao, R. Humphry-Baker, B. F. E. Curchod, N. Ashari-Astani, I. Tavernelli, U. Rothlisberger, M. K. Nazeeruddin, M. Grätzel, *Nat. Chem.* **2014**, *6*, 242.
- [85] A. Yella, C.-L. Mai, S. M. Zakeeruddin, S.-N. Chang, C.-H. Hsieh, C.-Y. Yeh, M. Grätzel, *Angew. Chem.* **2014**, *126*, 3017.
- [86] T. Bessho, S. M. Zakeeruddin, C. Y. Yeh, E. W. G. Diau, M. Grätzel, *Angew. Chem., Int. Ed.* **2010**, *49*, 6646.
- [87] A. Yella, H.-W. Lee, H. N. Tsao, C. Yi, A. K. Chandiran, M. K. Nazeeruddin, E. W.-G. Diau, C.-Y. Yeh, S. M. Zakeeruddin, M. Grätzel, *Science* **2011**, *334*, 629.
- [88] J. Luo, M. Xu, R. Li, K. W. Huang, C. Jiang, Q. Qi, W. Zeng, J. Zhang, C. Chi, P. Wang, J. Wu, *J. Am. Chem. Soc.* **2014**, *136*, 265.
- [89] C. L. Mai, W. K. Huang, H. P. Lu, C. W. Lee, C. L. Chiu, Y. R. Liang, E. W. G. Diau, C. Y. Yeh, *Chem. Commun.* **2010**, *46*, 809.
- [90] G. De Miguel, M. Marchena, M. Ziótek, S. S. Pandey, S. Hayase, A. Douhal, *J. Phys. Chem. C* **2012**, *116*, 12137.
- [91] V. Novelli, N. Barbero, C. Barolo, G. Viscardi, M. Sliwa, F. Sauvage, *Phys. Chem. Chem. Phys.* **2017**, *19*, 27670.
- [92] A. Janotti, C. G. Van De Walle, *Rep. Prog. Phys.* **2009**, *72*, 126501.
- [93] Q. Zhang, G. Cao, *J. Mater. Chem.* **2011**, *21*, 6769.
- [94] Q. Zhang, T. P. Chou, B. Russo, S. A. Jenekhe, G. Cao, *Angew. Chem., Int. Ed.* **2008**, *47*, 2402.
- [95] K. Tennakone, G. R. R. A. Kumara, I. R. M. Kottegoda, V. P. S. Perera, *Chem. Commun.* **1999**, 15.
- [96] H. Wang, A. L. Rogach, *Chem. Mater.* **2014**, *26*, 123.
- [97] M. S. Park, Y. M. Kang, G. X. Wang, S. X. Dou, H. K. Liu, *Adv. Funct. Mater.* **2008**, *18*, 455.
- [98] K. Sayama, H. Sugihara, H. Arakawa, *Chem. Mater.* **1998**, *10*, 3825.
- [99] P. Wang, S. M. Zakeeruddin, P. Comte, R. Charvet, R. Humphry-Baker, M. Grätzel, *J. Phys. Chem. B* **2003**, *107*, 14336.
- [100] C. Magne, F. Dufour, F. Labat, G. Lancel, O. Durupthy, S. Cassaignon, T. Pauporté, *J. Photochem. Photobiol., A* **2012**, *232*, 22.
- [101] B. Tan, E. Toman, Y. Li, Y. Wu, *J. Am. Chem. Soc.* **2007**, *129*, 4162.
- [102] L. Huang, L. Jiang, M. Wei, *Electrochem. Commun.* **2010**, *12*, 319.
- [103] Y. Suzuki, Y. Okamoto, N. Ishii, *J. Phys.: Conf. Ser.* **2015**, *596*, 012001.
- [104] S. M. Gupta, M. Tripathi, *Cent. Eur. J. Chem.* **2012**, *10*, 279.
- [105] F. Dufour, S. Pigeot-Remy, O. Durupthy, S. Cassaignon, V. Ruaux, S. Torelli, L. Mariey, F. Maugé, C. Chanéac, *Appl. Catal., B* **2015**, *174–175*, 350.
- [106] M. Ali Ahmad, B. Prelot, F. Dufour, O. Durupthy, A. Razafitianam aharavo, J. M. Douillard, C. Chaneac, F. Villieras, J. Zajac, *J. Phys. Chem. C* **2013**, *117*, 4459.
- [107] A. Kumar, *Am. J. Nano Res. Appl.* **2018**, *6*, 1.
- [108] M. T. Norman, M. A. Ashraf, A. Ali, *Environ. Sci. Pollut. Res.* **2019**, *26*, 3262.
- [109] B. Roose, S. Pathak, U. Steiner, *Chem. Soc. Rev.* **2015**, *44*, 8326.
- [110] *Interfacial Engineering in Functional Materials for Dye-Sensitized Solar Cells* (Eds: A. Pandikumar, K. Jothivenkatachalam, K. B. Bhojanaa), Wiley, New York **2020**.
- [111] M. R. Mohammadi, A. M. Bakhshayesh, F. Sadri, M. Masroor, *J. Sol-Gel Sci. Technol.* **2013**, *67*, 77.
- [112] A. K. Chandiran, F. Sauvage, M. Casas-Cabanas, P. Comte, S. M. Zakeeruddin, M. Graetzel, *J. Phys. Chem. C* **2010**, *114*, 15849.
- [113] A. V. Manole, M. Dobromir, M. Gîrtan, R. Mallet, G. Rusu, D. Luca, *Ceram. Int.* **2013**, *39*, 4771.
- [114] H. Seo, Y. Wang, D. Ichida, G. Uchida, N. Itagaki, K. Koga, M. Shiratani, S. H. Nam, J. H. Boo, *Jpn. J. Appl. Phys.* **2013**, *52*, 2.
- [115] X. Zhang, F. Liu, Q. L. Huang, G. Zhou, Z. S. Wang, *J. Phys. Chem. C* **2011**, *115*, 12665.
- [116] A. M. Cant, F. Huang, X. L. Zhang, Y. Chen, Y. B. Cheng, R. Amal, *Nanoscale* **2014**, *6*, 3875.
- [117] Z. Tong, T. Peng, W. Sun, W. Liu, S. Guo, X. Z. Zhao, *J. Phys. Chem. C* **2014**, *118*, 16892.
- [118] H. Krysova, P. Mazzolini, C. S. Casari, V. Russo, A. L. Bassi, L. Kavan, *Electrochim. Acta* **2017**, *232*, 44.
- [119] J. Anuntahirunrat, Y. M. Sung, P. Pooyodying, *IOP Conf. Ser.: Mater. Sci. Eng.* **2017**, *229*, 012019.
- [120] R. G. Breckenridge, W. R. Hosler, *Phys. Rev.* **1953**, *91*, 793.
- [121] M. Law, L. E. Greene, J. C. Johnson, R. Saykally, P. Yang, *Nat. Mater.* **2005**, *4*, 455.
- [122] J. Qian, P. Liu, Y. Xiao, Y. Jiang, Y. Cao, X. Ai, H. Yang, *Adv. Mater.* **2009**, *21*, 3663.
- [123] C. G. Fonstad, R. H. Rediker, *J. Appl. Phys.* **1971**, *42*, 2911.
- [124] Y. Fukai, Y. Kondo, S. Mori, E. Suzuki, *Electrochem. Commun.* **2007**, *9*, 1439.
- [125] A. N. M. Green, E. Palomares, S. A. Haque, J. M. Kroon, J. R. Durrant, *J. Phys. Chem. B* **2005**, *109*, 12525.
- [126] P. Tiwana, P. Docampo, M. B. Johnston, H. J. Snaith, L. M. Herz, *ACS Nano* **2011**, *5*, 5158.

- [127] P. Pratim Das, A. Roy, S. Das, P. S. Devi, *Phys. Chem. Chem. Phys.* **2016**, *18*, 1429.
- [128] C. Chen, Y. Li, X. Sun, F. Xie, M. Wei, *New J. Chem.* **2014**, *38*, 4465.
- [129] T. J. Coutts, D. L. Young, X. Li, W. P. Mulligan, X. Wu, *J. Vac. Sci. Technol., A* **2000**, *18*, 2646.
- [130] A. Kay, M. Grätzel, *Chem. Mater.* **2002**, *14*, 2930.
- [131] A. Merazga, F. Al-Subai, A. M. Albaradi, A. Badawi, A. Y. Jaber, A. A. B. Alghamdi, *Mater. Sci. Semicond. Process.* **2016**, *41*, 114.
- [132] T. V. Nguyen, H. C. Lee, M. Alam Khan, O. B. Yang, *Sol. Energy* **2007**, *81*, 529.
- [133] E. Palomares, J. N. Clifford, S. A. Haque, T. Lutz, J. R. Durrant, *Chem. Commun.* **2002**, *2*, 1464.
- [134] E. Palomares, J. N. Clifford, S. A. Haque, T. Lutz, J. R. Durrant, *J. Am. Chem. Soc.* **2003**, *125*, 475.
- [135] G. R. R. A. Kumara, K. Tennakone, V. P. S. Perera, A. Konno, S. Kaneko, M. Okuya, *J. Phys. D: Appl. Phys.* **2001**, *34*, 868.
- [136] C. S. Chou, F. C. Chou, J. Y. Kang, *Powder Technol.* **2012**, *215*, 38.
- [137] D. Maheswari, P. Venkatchalam, *Aust. J. Chem.* **2015**, *68*, 881.
- [138] T. Y. Cho, K. W. Ko, S. G. Yoon, S. S. Sekhon, M. G. Kang, Y. S. Hong, C. H. Han, *Curr. Appl. Phys.* **2013**, *13*, 1391.
- [139] M. Bonomo, A. Di Carlo, D. Dini, *J. Electrochem. Soc.* **2018**, *165*, H889.
- [140] T. W. Hamann, J. W. Ondersma, *Energy Environ. Sci.* **2011**, *4*, 370.
- [141] D. P. Hagberg, J. H. Yum, H. J. Lee, F. De Angelis, T. Marinado, K. M. Karlsson, R. Humphry-Baker, L. Sun, A. Hagfeldt, M. Grätzel, M. K. Nazeeruddin, *J. Am. Chem. Soc.* **2008**, *130*, 6259.
- [142] Y. Saygili, M. Stojanovic, N. Flores-Díaz, S. M. Zakeeruddin, N. Vlachopoulos, M. Grätzel, A. Hagfeldt, *Inorganics* **2019**, *7*, 30.
- [143] A. A. Tsaturyan, A. P. Budnyk, C. Ramalingan, *ACS Omega* **2019**, *4*, 10991.
- [144] S. Soman, S. C. Pradhan, M. Yoosuf, M. V. Vinayak, S. Lingamoorthy, K. R. Gopidas, *J. Phys. Chem. C* **2018**, *122*, 14113.
- [145] F. Bella, S. Galliano, C. Gerbaldi, G. Viscardi, *Energies* **2016**, *9*, 384.
- [146] L. Giribabu, R. Bolligarla, M. Panigrahi, *Chem. Rec.* **2015**, *15*, 760.
- [147] K. Kakiage, Y. Aoyama, T. Yano, K. Oya, J. I. Fujisawa, M. Hanaya, *Chem. Commun.* **2015**, *51*, 15894.
- [148] K. Ben Aribia, T. Moehl, S. M. Zakeeruddin, M. Grätzel, *Chem. Sci.* **2013**, *4*, 454.
- [149] P. Salvatori, G. Marotta, A. Cinti, E. Mosconi, M. Panigrahi, L. Giribabu, M. K. Nazeeruddin, F. De Angelis, *Inorg. Chim. Acta* **2013**, *406*, 106.
- [150] J. Baillargeon, Y. Xie, A. L. Raitheal, B. Ghaffari, R. J. Staples, T. W. Hamann, *Inorg. Chem.* **2018**, *57*, 11633.
- [151] I. Krivokapic, M. Zerara, M. L. Daku, A. Vargas, C. Enachescu, C. Ambrus, P. Tregenna-Piggott, N. Amstutz, E. Krausz, A. Hauser, *Coord. Chem. Rev.* **2007**, *251*, 364.
- [152] E. Mosconi, J. H. Yum, F. Kessler, C. J. Gómez García, C. Zuccaccia, A. Cinti, M. K. Nazeeruddin, M. Grätzel, F. De Angelis, *J. Am. Chem. Soc.* **2012**, *134*, 19438.
- [153] O. Sato, *Proc. Jpn. Acad., Ser. B* **2012**, *88*, 213.
- [154] N. Shimamoto, S. I. Ohkoshi, O. Sato, K. Hashimoto, *Inorg. Chem.* **2002**, *41*, 678.
- [155] C. Förster, M. Dorn, T. Reuter, S. Otto, G. Davarci, T. Reich, L. Carrella, E. Rentschler, K. Heinze, *Inorganics* **2018**, *6*, 86.
- [156] M. T. , S. H. Molla, Z. M. , N. Mizukoshi, H. Furukawa, Y. Ogomi, S. S. Pandey, *Prog. Photovoltaics* **2015**, *23*, 1100.
- [157] T. W. Hamann, *Dalton Trans.* **2012**, *41*, 3111.
- [158] M. Stojanović, N. Flores-Díaz, Y. Ren, N. Vlachopoulos, L. Pfeifer, Z. Shen, Y. Liu, S. M. Zakeeruddin, J. V. Milić, A. Hagfeldt, *Helv. Chim. Acta* **2021**, *104*.
- [159] Z. Z. Sun, K. M. Zheng, Q. S. Li, Z. S. Li, *RSC Adv.* **2014**, *4*, 31544.
- [160] J. H. Yum, E. Baranoff, F. Kessler, T. Moehl, S. Ahmad, T. Bessho, A. Marchioro, E. Ghadiri, J. E. Moser, C. Yi, M. K. Nazeeruddin, M. Grätzel, *Nat. Commun.* **2012**, *3*, 631.
- [161] M. K. Kashif, J. C. Axelson, N. W. Du, C. M. Forsyth, C. J. Chang, R. Long, L. Spiccia, U. Bach, *J. Am. Chem. Soc.* **2012**, *134*, 16646.
- [162] M. K. Kashif, R. A. Milhaisen, M. Nippe, J. Hellerstedt, D. Z. Zee, N. W. Duffy, B. Halstead, F. De Angelis, S. Fantacci, M. S. Fuhrer, C. J. Chang, Y. B. Cheng, J. R. Long, L. Spiccia, U. Bach, *Adv. Energy Mater.* **2016**, *6*, 1600874.
- [163] S. M. Feldt, E. A. Gibson, E. Gabrielsson, L. Sun, G. Boschloo, A. Hagfeldt, *J. Am. Chem. Soc.* **2010**, *132*, 16714.
- [164] H. Nusbaumer, J. E. Moser, S. M. Zakeeruddin, M. K. Nazeeruddin, M. Grätzel, *J. Phys. Chem. B* **2001**, *105*, 10461.
- [165] H. Nusbaumer, S. M. Zakeeruddin, J. E. Moser, M. Grätzel, *Chem. – Eur. J.* **2003**, *9*, 3756.
- [166] P. J. Cameron, L. M. Peter, S. M. Zakeeruddin, M. Grätzel, *Coord. Chem. Rev.* **2004**, *248*, 1447.
- [167] N. A. Lee, B. A. Frenzel, J. Rochford, S. E. Hightower, *Eur. J. Inorg. Chem.* **2015**, *23*, 3843.
- [168] J. T. Kirner, C. M. Elliott, *J. Phys. Chem. C* **2015**, *119*, 17502.
- [169] S. Yang, H. Kou, H. Wang, K. Cheng, J. Wang, *New J. Chem.* **2010**, *34*, 313.
- [170] M. Nasr-Esfahani, M. Zendeheel, N. Yaghoobi Nia, B. Jafari, M. Khosravi Babadi, *RSC Adv.* **2014**, *4*, 15961.
- [171] Y. Xie, J. Baillargeon, T. W. Hamann, *J. Phys. Chem. C* **2015**, *119*, 28155.
- [172] J. Gao, M. Bhagavathi Achari, L. Kloo, *Chem. Commun.* **2014**, *50*, 6249.
- [173] N. Mariotti, M. Bonomo, L. Fagioli, N. Barbero, C. Gerbaldi, F. Bella, C. Barolo, *Green Chem.* **2020**, *22*, 7168.
- [174] Y. Liu, S.-C. Yiu, C.-L. Ho, W.-Y. Wong, *Coord. Chem. Rev.* **2018**, *375*, 514.
- [175] R. Ilmi, I. Juma Al-busaidi, A. Haque, M. S. Khan, *J. Coord. Chem.* **2018**, *71*, 3045.
- [176] J. Cong, D. Kinschel, Q. Daniel, M. Safdari, E. Gabrielsson, H. Chen, P. H. Svensson, L. Sun, L. Kloo, *J. Mater. Chem. A* **2016**, *4*, 14550.
- [177] S. Hattori, Y. Wada, S. Yanagida, S. Fukuzumi, *J. Am. Chem. Soc.* **2005**, *127*, 9648.
- [178] M. Magni, R. Giannuzzi, A. Colombo, M. P. Cipolla, C. Dragonetti, S. Caramori, S. Carli, R. Grisorio, G. P. Suranna, C. A. Bignozzi, D. Roberto, M. Manca, *Inorg. Chem.* **2016**, *55*, 5245.
- [179] A. Colombo, G. Di Carlo, C. Dragonetti, M. Magni, A. Orbelli Biroli, M. Pizzotti, D. Roberto, F. Tessore, E. Benazzi, C. A. Bignozzi, L. Casarin, S. Caramori, *Inorg. Chem.* **2017**, *56*, 14189.
- [180] S. Pflöck, A. Beyer, L. Müller, N. Burzlauff, *Polyhedron* **2017**, *125*, 34.
- [181] C. Dragonetti, M. Magni, A. Colombo, F. Fagnani, D. Roberto, F. Melchiorre, P. Biagini, S. Fantacci, *Dalton Trans.* **2019**, *48*, 9703.
- [182] C. Dragonetti, M. Magni, A. Colombo, F. Melchiorre, P. Biagini, D. Roberto, *ACS Appl. Mater. Interfaces* **2018**, *1*, 751.
- [183] A. Colombo, C. Dragonetti, F. Fagnani, D. Roberto, F. Melchiorre, P. Biagini, *Dalton Trans.* **2019**, *48*, 9818.
- [184] R. L. Lord, F. A. Schultz, M. H. Baik, *J. Am. Chem. Soc.* **2009**, *131*, 6189.
- [185] I. R. Perera, A. Gupta, W. Xiang, T. Daeneke, U. Bach, R. A. Evans, C. A. Ohlin, L. Spiccia, *Phys. Chem. Chem. Phys.* **2014**, *16*, 12021.
- [186] T. Daeneke, T.-H. Kwon, A. B. Holmes, N. W. Duffy, U. Bach, L. Spiccia, *Nat. Chem.* **2011**, *3*, 211.
- [187] T. J. Kealy, P. L. Pauson, *Nature* **1951**, *168*, 1039.
- [188] A. Bhattacharjee, A. Rooj, D. Roy, M. Roy, *J. Exp. Phys.* **2014**, *2014*, 513268.
- [189] I. Noviandri, K. N. Brown, D. S. Fleming, P. T. Gulyas, P. A. Lay, A. F. Masters, L. Phillips, *J. Phys. Chem. B* **1999**, *103*, 6713.
- [190] K. N. Brown, P. T. Gulyas, P. A. Lay, N. S. McAlpine, A. F. Masters, L. Phillips, *J. Chem. Soc. Dalton Trans.* **1993**, *6*, 835.
- [191] A. Paul, R. Borrelli, H. Bouyanff, S. Gottis, F. Sauvage, *ACS Omega* **2019**, *4*, 14780.

- [192] T. Daeneke, A. J. Mozer, T. H. Kwon, N. W. Duffy, A. B. Holmes, U. Bach, L. Spiccia, *Energy Environ. Sci.* **2012**, *5*, 7090.
- [193] Z. Zhang, P. Chen, T. N. Murakami, S. M. Zakeeruddin, M. Grätzel, *Adv. Funct. Mater.* **2008**, *18*, 341.
- [194] F. Kato, N. Hayashi, T. Murakami, C. Okumura, K. Oyaizu, H. Nishide, *Chem. Lett.* **2010**, *39*, 464.
- [195] T. C. Chu, R. Y. Y. Lin, C. P. Lee, C. Y. Hsu, P. C. Shih, R. Lin, S. R. Li, S. S. Sun, J. T. Lin, R. Vittal, K. C. Ho, *ChemSusChem* **2014**, *7*, 146.
- [196] A. Dhar, N. S. Kumar, M. Asif, R. L. Vekariya, *J. Photochem. Photobiol. A: Chem.* **2018**, *363*, 1.
- [197] X. Chen, D. Xu, L. Qiu, S. Li, W. Zhang, F. Yan, *J. Mater. Chem. A* **2013**, *1*, 8759.
- [198] W. Zhang, L. Qiu, X. Chen, F. Yan, *Electrochim. Acta* **2014**, *117*, 48.
- [199] F. Kato, A. Kikuchi, T. Okuyama, K. Oyaizu, H. Nishide, *Angew. Chem., Int. Ed.* **2012**, *51*, 10177.
- [200] D. Li, H. Li, Y. Luo, K. Li, Q. Meng, M. Armand, L. Chen, *Adv. Funct. Mater.* **2010**, *20*, 3358.
- [201] Y. Liu, J. R. Jennings, M. Parameswaran, Q. Wang, *Energy Environ. Sci.* **2011**, *4*, 564.
- [202] L. Wang, M. Wu, Y. Gao, T. Ma, *Appl. Phys. Lett.* **2011**, *98*, 98.
- [203] J. Zhang, H. Long, S. G. Miralles, J. Bisquert, F. Fabregat-Santiago, M. Zhang, *Phys. Chem. Chem. Phys.* **2012**, *14*, 7131.
- [204] Y. Liu, J. R. Jennings, Q. Wang, *ChemSusChem* **2013**, *6*, 2124.
- [205] X. Li, Z. Ku, Y. Rong, G. Liu, L. Liu, T. Liu, M. Hu, Y. Yang, H. Wang, M. Xu, P. Xiang, H. Han, *Phys. Chem. Chem. Phys.* **2012**, *14*, 14383.
- [206] A. Hilmi, T. A. Shoker, T. H. Ghaddar, *ACS Appl. Mater. Interfaces* **2014**, *6*, 8744.
- [207] K. Funabiki, Y. Saito, M. Doi, K. Yamada, Y. Yoshikawa, K. Manseki, Y. Kubota, M. Matsui, *Tetrahedron* **2014**, *70*, 6312.
- [208] H. Tian, E. Gabrielsson, P. W. Lohse, N. Vlachopoulos, L. Kloo, A. Hagfeldt, L. Sun, *Energy Environ. Sci.* **2012**, *5*, 9752.
- [209] H. Tian, L. Sun, *J. Mater. Chem.* **2011**, *21*, 10592.
- [210] H. Tian, X. Jiang, Z. Yu, L. Kloo, A. Hagfeldt, L. Sun, *Angew. Chem.* **2010**, *122*, 7486.
- [211] M. M. Rahman, J. Wang, N. C. D. Nath, J. J. Lee, *Electrochim. Acta* **2018**, *286*, 39.
- [212] Y. Zhang, Z. Sun, C. Shi, F. Yan, *RSC Adv.* **2016**, *6*, 70460.
- [213] Z. Ku, X. Li, G. Liu, H. Wang, Y. Rong, M. Xu, L. Liu, M. Hu, Y. Yang, H. Han, *J. Mater. Chem. A* **2013**, *1*, 237.
- [214] T. C. Li, F. Fabregat-Santiago, O. K. Farha, A. M. Spokoyny, S. R. Raga, J. Bisquert, C. A. Mirkin, T. J. Marks, J. T. Hupp, *J. Phys. Chem. C* **2011**, *115*, 11257.
- [215] M. Cheng, X. Yang, F. Zhang, J. Zhao, L. Sun, *Angew. Chem., Int. Ed.* **2012**, *51*, 9896.
- [216] M. Cheng, X. Yang, C. Chen, J. Zhao, F. Zhang, L. Sun, *Phys. Chem. Chem. Phys.* **2013**, *15*, 15146.
- [217] <https://doi.org/10.1016/j.solener.2018.03.084>.
- [218] N. C. D. Nath, J.-J. Lee, *J. Ind. Eng. Chem.* **2019**, *78*, 53.
- [219] N. C. D. Nath, H. J. Lee, W. Y. Choi, J. J. Lee, *Electrochim. Acta* **2013**, *109*, 39.
- [220] N. C. D. Nath, I. S. Jung, P. J. Park, J. J. Lee, *Electrochim. Acta* **2015**, *167*, 95.
- [221] K. Yoo, N. C. Deb Nath, H. C. Kang, S. Muthu, J.-J. Lee, *ECS J. Solid State Sci. Technol.* **2021**, *10*, 025007.
- [222] J. Cong, X. Yang, Y. Hao, L. Kloo, L. Sun, *RSC Adv.* **2012**, *2*, 3625.
- [223] J. Cong, Y. Hao, G. Boschloo, L. Kloo, *ChemSusChem* **2015**, *8*, 264.
- [224] Y. Hao, W. Yang, L. Zhang, R. Jiang, E. Mijangos, Y. Saygili, L. Hammarström, A. Hagfeldt, G. Boschloo, *Nat. Commun.* **2016**, *7*, 13934.
- [225] G. R. Li, X. P. Gao, *Adv. Mater.* **2020**, *32*, 1905578.
- [226] X. Zhang, Y. Yang, S. Guo, F. Hu, L. Liu, *ACS Appl. Mater. Interfaces* **2015**, *7*, 8457.
- [227] N. Papageorgiou, W. F. Maier, M. Grätzel, *J. Electrochem. Soc.* **1997**, *144*, 876.
- [228] A. Hauch, A. Georg, *Electrochim. Acta* **2001**, *46*, 3457.
- [229] U. Ahmed, M. Alizadeh, N. A. Rahim, S. Shahabuddin, M. S. Ahmed, A. K. Pandey, *Sol. Energy* **2018**, *174*, 1097.
- [230] E. Olsen, G. Hagen, S. Eric Lindquist, *Sol. Energy Mater. Sol. Cells* **2000**, *63*, 267.
- [231] C. H. Yoon, R. Vittal, J. Lee, W. S. Chae, K. J. Kim, *Electrochim. Acta* **2008**, *53*, 2890.
- [232] G. Calogero, P. Calandra, A. Irrera, A. Sinopoli, I. Citro, G. Di Marco, *Energy Environ. Sci.* **2011**, *4*, 1838.
- [233] X. Fang, T. Ma, G. Guan, M. Akiyama, T. Kida, E. Abe, *J. Electroanal. Chem.* **2004**, *570*, 257.
- [234] N. Papageorgiou, *Coord. Chem. Rev.* **2004**, *248*, 1421.
- [235] H. Otaka, M. Kira, K. Yano, S. Ito, H. Mitekura, T. Kawata, F. Matsui, *J. Photochem. Photobiol., A* **2004**, *164*, 67.
- [236] M. Saifullah, J. Gwak, J. H. Yun, A. Abate, H. J. Snaith, G. Gigli, K. Konstantinidis, J. P. Mannaerts, M. L. Schnoes, G. J. Zyzdzik, W. Wischmann, M. Powalla, J. F. Guillemoles, D. Lincot, H. W. Schock, N. Katoh, A. Takeichi, K. Takechi, M. Shiozawa, *J. Mater. Chem. A* **2016**, *4*, 8512.
- [237] Y. Yang, T. Chen, D. Pan, Z. Zhang, X. Guo, *Acta Chim. Sin.* **2018**, *76*, 681.
- [238] H. H. Gong, S. H. Park, S.-S. Lee, S. C. Hong, *Int. J. Precis. Eng. Manuf.* **2014**, *15*, 1193.
- [239] M. Kouhnavard, N. A. Ludin, B. V. Ghaffari, K. Sopian, S. Ikeda, *ChemSusChem* **2015**, *8*, 1510.
- [240] S. Thomas, T. G. Deepak, G. S. Anjusree, T. A. Arun, S. V. Nair, A. S. Nair, *J. Mater. Chem. A* **2014**, *2*, 4474.
- [241] P. Wei, X. Chen, G. Wu, J. Li, Y. Yang, Z. Hao, X. Zhang, L. Liu, *Chin. J. Catal.* **2019**, *40*, 1282.
- [242] H. Wang, Y. H. Hu, *Energy Environ. Sci.* **2012**, *5*, 8182.
- [243] J. D. Roy-Mayhew, I. A. Aksay, *Chem. Rev.* **2014**, *114*, 6323.
- [244] H. Choi, S. Hwang, H. Bae, S. Kim, H. Kim, M. Jeon, *Electron. Lett.* **2011**, *47*, 281.
- [245] K. S. Lee, Y. Lee, J. Y. Lee, J. H. Ahn, J. H. Park, *ChemSusChem* **2012**, *5*, 379.
- [246] S. S. Nemala, P. Kartikay, K. S. Aneja, P. Bhargava, H. L. M. Bohm, S. Bohm, S. Mallick, *ACS Appl. Energy Mater.* **2018**, *1*, 2512.
- [247] D. Dodoo-Arhin, M. Fabiane, A. Bello, N. Manyala, *Ind. Eng. Chem. Res.* **2013**, *52*, 14160.
- [248] J. D. Roy-Mayhew, G. Boschloo, A. Hagfeldt, I. A. Aksay, *ACS Appl. Mater. Interfaces* **2012**, *4*, 2794.
- [249] S. J. Li, Y. Xing, D. H. Deng, M. M. Shi, P. P. Guan, *J. Solid State Electrochem.* **2015**, *19*, 861.
- [250] D. Li, M. B. Müller, S. Gilje, R. B. Kaner, G. G. Wallace, *Nat. Nanotechnol.* **2008**, *3*, 101.
- [251] Y. H. Ha, N. Nikolov, S. K. Pollack, J. Mastrangelo, B. D. Martin, R. Shashidhar, *Adv. Funct. Mater.* **2004**, *14*, 615.
- [252] M. Biancardo, K. West, F. C. Krebs, *J. Photochem. Photobiol., A* **2007**, *187*, 395.
- [253] S. S. Jeon, C. Kim, J. Ko, S. S. Im, *J. Mater. Chem.* **2011**, *21*, 8146.
- [254] J. Wu, Q. Li, L. Fan, Z. Lan, P. Li, J. Lin, S. Hao, *J. Power Sources* **2008**, *181*, 172.
- [255] K. S. Lee, H. K. Lee, D. H. Wang, N. G. Park, J. Y. Lee, O. O. Park, J. H. Park, *Chem. Commun.* **2010**, *46*, 4505.
- [256] M. Wang, A. M. Anghel, B. Marsan, N. L. C. Ha, N. Pootrakulchote, S. M. Zakeeruddin, M. Grätzel, *J. Am. Chem. Soc.* **2009**, *131*, 15976.
- [257] H. Lin, Q. Zhu, D. Shu, D. Lin, J. Xu, X. Huang, W. Shi, X. Xi, J. Wang, L. Gao, *Nat. Mater.* **2019**, *18*, 602.
- [258] R. Prins, M. E. Bussell, *Catal. Lett.* **2012**, *142*, 1413.
- [259] S. Dong, X. Chen, X. Zhang, G. Cui, *Coord. Chem. Rev.* **2013**, *257*, 1946.
- [260] M. Naguib, O. Mashtalir, J. Carle, V. Presser, J. Lu, L. Hultman, Y. Gogotsi, M. W. Barsoum, *ACS Nano* **2012**, *6*, 1322.
- [261] C. N. R. Rao, *Annu. Rev. Phys. Chem.* **1989**, *40*, 291.

- [262] Y. Duan, Q. Tang, J. Liu, B. He, L. Yu, *Angew. Chem., Int. Ed.* **2014**, *53*, 14569.
- [263] F. Gong, H. Wang, X. Xu, G. Zhou, Z. S. Wang, *J. Am. Chem. Soc.* **2012**, *134*, 10953.
- [264] Y.-C. Wang, D.-Y. Wang, Y.-T. Jiang, H.-A. Chen, C.-C. Chen, K.-C. Ho, H.-L. Chou, C.-W. Chen, *Angew. Chem.* **2013**, *125*, 6826.
- [265] M. Congiu, M. Bonomo, M. L. De Marco, D. P. Dowling, A. Di Carlo, D. Dini, C. F. O. Graeff, *ChemistrySelect* **2016**, *1*, 2808.
- [266] J. Y. Lin, J. H. Liao, T. C. Wei, *Electrochem. Solid-State Lett.* **2011**, *14*, 3.
- [267] J. Huo, J. Wu, M. Zheng, Y. Tu, Z. Lan, *Electrochim. Acta* **2016**, *187*, 210.
- [268] M. Bonomo, D. Dini, F. Decker, *Front. Chem.* **2018**, *6*, 1.
- [269] M. Bonomo, D. Dini, A. G. Marrani, R. Zannoni, *Colloids Surfaces A Physicochem. Eng. Asp.* **2017**, *532*, 464.
- [270] a) X. Sun, J. Dou, F. Xie, Y. Li, M. Wei, *Chem. Commun.* **2014**, *50*, 9869; b) Z. Wan, C. Jia, Y. Wang, *Nanoscale* **2015**, *7*, 12737; c) H. Sun, D. Qin, S. Huang, X. Guo, D. Li, Y. Luo, Q. Meng, *Energy Environ. Sci.* **2011**, *4*, 2630.
- [271] L. Li, Q. Lu, W. Li, X. Li, A. Hagfeldt, W. Zhang, M. Wu, *J. Power Sources* **2016**, *308*, 37.
- [272] C. Feng, Z. Jin, M. Zheng, Z. S. Wang, *Electrochim. Acta* **2018**, *281*, 237.
- [273] J. Jia, J. Wu, Y. Tu, J. Hou, M. Zheng, J. Lin, *J. Alloys Compd.* **2015**, *640*, 29.
- [274] F. Gong, X. Xu, Z. Li, G. Zhou, Z. S. Wang, *Chem. Commun.* **2013**, *49*, 1437.
- [275] C. Zhang, Y. Li, L. Deng, P. Zhang, X. Ren, S. Yun, *J. Solid State Electrochem.* **2016**, *20*, 2373.
- [276] J. Song, G. R. Li, C. Y. Wu, X. P. Gao, *J. Power Sources* **2014**, *266*, 464.
- [277] a) Y. Hou, D. Wang, X. H. Yang, W. Q. Fang, B. Zhang, H. F. Wang, G. Z. Lu, P. Hu, H. J. Zhao, H. G. Yang, *Nat. Commun.* **2013**, *4*, 1583; b) M. Congiu, M. L. De Marco, M. Bonomo, O. Nunes-Neto, D. Dini, C. F. O. Graeff, *J. Nanoparticle Res* **2017**, *19*, 7.
- [278] S. Shukla, N. H. Loc, P. P. Boix, T. M. Koh, R. R. Prabhakar, H. K. Mulmudi, J. Zhang, S. Chen, C. F. Ng, C. H. A. Huan, N. Mathews, T. Sritharan, Q. Xiong, *ACS Nano* **2014**, *8*, 10597.
- [279] J. Liu, Q. Tang, B. He, L. Yu, *J. Power Sources* **2015**, *282*, 79.
- [280] S. S. Kim, J. W. Lee, J. M. Yun, S. I. Na, *J. Ind. Eng. Chem.* **2015**, *29*, 71.
- [281] T. Jeong, S.-Y. Ham, B. Koo, P. Lee, Y.-S. Min, J.-Y. Kim, M. J. Ko, *J. Ind. Eng. Chem.* **2019**, *80*, 106.
- [282] Y. Duan, Q. Tang, B. He, Z. Zhao, L. Zhu, L. Yu, *J. Power Sources* **2015**, *284*, 349.
- [283] P. Yang, Z. Zhao, L. Zhu, Q. Tang, *J. Alloys Compd.* **2015**, *648*, 930.
- [284] P. Li, Q. Tang, *J. Power Sources* **2016**, *317*, 43.
- [285] J. Ou, B. Hu, S. He, W. Wang, Y. Han, *Sol. Energy* **2020**, *201*, 693.
- [286] E. Born, M. Wolf, in *Principles of Optics Electromagnetic Theory of Propagation, Interference and Diffraction of Light*, Elsevier, Cambridge **2002**, p. 13.
- [287] M. S. W. Wong, P. A. Sermon, *Thin Solid Films* **1997**, *293*, 185.
- [288] R. Messner, *Optik* **1947**, *2*, 228.
- [289] L. Zhang, Y. Li, J. Sun, J. Shen, *Langmuir* **2008**, *24*, 10851.
- [290] T. G. Ulusoy, B. Daglar, A. Yildirim, A. Ghobadi, M. Bayindir, A. K. Okyay, *J. Photonics Energy* **2015**, *5*, 053090.
- [291] U. Tuvshindorj, A. Yildirim, F. E. Ozturk, M. Bayindir, *ACS Appl. Mater. Interfaces* **2014**, *6*, 9680.
- [292] P. Buskens, M. Burghoorn, M. C. D. Mourad, Z. Vroon, *Langmuir* **2016**, *32*, 6781.
- [293] S. Walheim, E. Schäffer, J. Mlynek, U. Steiner, *Science* **1999**, *283*, 520.
- [294] B. E. Yoldas, *Appl. Opt.* **1980**, *19*, 1425.
- [295] B. E. Yoldas, D. P. Partlow, *Thin Solid Films* **1985**, *129*, 1.
- [296] M. M. Braun, L. Pilon, *Thin Solid Films* **2006**, *496*, 505.
- [297] C. B. Honsberg, S. G. Bowden, *Design-of-silicon-cells: Anti-reflection-coatings*, page on www.pveducation.org, **2019** (accessed: April 2021).
- [298] S. Chattopadhyay, Y. F. Huang, Y. J. Jen, A. Ganguly, K. H. Chen, L. C. Chen, *Mater. Sci. Eng., R* **2021**, *69*, 1.
- [299] H. Jiang, K. Yu, Y. Wang, *Opt. Lett.* **2007**, *32*, 575.
- [300] H. Jiang, W. Zhao, C. Li, Y. Wang, *Soft Matter* **2011**, *7*, 2817.
- [301] J. W. Ha, I. J. Park, S. B. Lee, *Macromolecules* **2008**, *41*, 8800.
- [302] J. Szczyrbowski, G. Bräuer, G. Teschner, A. Zmelty, *J. Non-Cryst. Solids* **1997**, *218*, 25.
- [303] A. Szeghalmi, M. Helgert, R. Brunner, F. Heyroth, U. Gösele, M. Knez, *Appl. Opt.* **2009**, *48*, 1727.
- [304] D. Chen, *Solar Energy Mater. Solar Cells* **2001**, *68*, 313.
- [305] G. M. Nogueira, D. Banerjee, R. E. Cohen, M. F. Rubner, *Langmuir* **2011**, *27*, 7860.
- [306] B. G. Prevo, Y. Hwang, O. D. Velev, *Chem. Mater.* **2005**, *17*, 3642.
- [307] K. Askar, Z. Gu, C. J. Leverant, J. Wang, C. Kim, B. Jiang, P. Jiang, *Opt. Letter.* **2018**, *43*, 5238.
- [308] X. Li, J. Shen, *Thin Solid Films* **2011**, *519*, 6236.
- [309] J. Zha, X. Lu, Z. Xin, *J. Sol-Gel Sci. Technol.* **2015**, *74*, 677.
- [310] L. Zou, X. Li, Q. Zhang, J. Shen, *Langmuir* **2014**, *30*, 10481.
- [311] Y. Li, H. Lv, L. Ye, L. Yan, Y. Zhang, B. Xia, H. Yan, B. Jiang, *RSC Adv.* **2015**, *5*, 20365.
- [312] W. Li, F. Lv, T. Shu, X. Tan, L. Jiang, T. Xiao, P. Xiang, *Mater. Lett.* **2019**, *243*, 108.
- [313] L. Bao, Z. Ji, H. Wang, R. Chen, *Langmuir* **2017**, *33*, 6240.
- [314] V. D. Bruggeman, *Ann. Phys.* **1935**, *416*, 636.
- [315] J. C. Maxwell-Garnett, *Philos. Trans. R. Soc., A* **1904**, *203*, 385.
- [316] J. Sun, X. Cui, C. Zhang, C. Zhang, R. Ding, Y. Xu, *J. Mater. Chem. C* **2015**, *3*, 7187.
- [317] B. Xiao, B. Xia, H. Lv, X. Zhang, B. Jiang, *J. Sol-Gel Sci. Technol.* **2012**, *64*, 276.
- [318] J. J. Yuan, O. O. Mykhaylyk, A. J. Ryan, S. P. Armes, *J. Am. Chem. Soc.* **2007**, *129*, 1717.
- [319] P. Buskens, N. Arfsten, R. Habets, H. Langermans, A. Overbeek, J. Scheerder, J. Thies, N. Viets, *Glass Perform Days* **2009**.
- [320] J. Hu, M. Chen, X. Fang, L. Wu, *Chem. Soc. Rev.* **2011**, *40*, 5472.
- [321] S. S. Shin, W. S. Yang, J. H. Noh, J. H. Suk, N. J. Jeon, J. H. Park, J. S. Kim, W. M. Seong, S. Il Seok, *Nat. Commun.* **2015**, *6*, 7410.
- [322] S. Wenger, M. Schmid, G. Rothenberger, A. Gentsch, M. Gratzel, J. O. Schumacher, *J. Phys. Chem. C* **2011**, *10218*.
- [323] K. Xie, M. Guo, H. Huang, *J. Mater. Chem. C* **2015**, *3*, 10665.
- [324] H. A. Macleod, *Thin-Film Optical Filters*, CRC Press, Boca Raton, FL **2010**.
- [325] A. Yildirim, T. Khudiyev, B. Daglar, H. Budunoglu, A. K. Okyay, M. Bayindir, *ACS Appl. Mater. Interfaces* **2013**, *5*, 853.
- [326] H. Budunoglu, A. Yildirim, M. O. Guler, M. Bayindir, *ACS Appl. Mater. Interfaces* **2011**, *3*, 539.
- [327] H. Tang, H. Wang, J. He, *J. Phys. Chem. C* **2009**, *113*, 14220.
- [328] D. Grosso, C. Boissière, C. Sanchez, *Nat. Mater.* **2007**, *6*, 572.
- [329] L. Bao, J. Wu, H. Wang, R. Chen, *Mater. Lett.* **2016**, *185*, 464.
- [330] C. H. Sun, A. Gonzalez, N. C. Linn, P. Jiang, B. Jiang, *Appl. Phys. Lett.* **2008**, *92*, 051107.
- [331] J. Huang, X. Wang, Z. L. Wang, *Nanotechnology* **2008**, *19*, 025602.
- [332] Y. Saito, T. Kosuge, *Sol. Energy Mater. Sol. Cells* **2007**, *91*, 1800.
- [333] M. cheol Kim, S. Jang, J. Choi, S. M. Kang, M. Choi, *Nano-Micro Lett.* **2019**, *11*, 1.
- [334] J. K. Tsai, Y. S. Tu, *Materials* **2017**, *10*, 296.
- [335] J. H. Lim, J. W. Leem, J. S. Yu, *RSC Adv.* **2015**, *5*, 61284.
- [336] S. Y. Heo, J. K. Koh, G. Kang, S. H. Ahn, W. S. Chi, K. Kim, J. H. Kim, *Adv. Energy Mater.* **2014**, *4*, 1300632.
- [337] E. F. Schubert, *Light-Emitting Diodes*, Cambridge University Press, Cambridge **2006**.
- [338] C. S. McCamy, *Color Res. Appl.* **1992**, *17*, 142.



Fionnuala Grifoni obtained her M.Sc. degree in Industrial Chemistry in 2019 from the University of Turin, Department of Chemistry, under the supervision of Dr. Barbero and in cooperation with Dr. Sauvage. Currently, she is a doctoral student at the Laboratoire de Réactivité et Chimie Solide (LRCS), in the University of Picardie Jules Verne, Amiens, in Dr. Sauvage's group, exploring colorless and transparent near infrared dye sensitized solar cells.



Matteo Bonomo got his master degree (2015) and Ph.D. (2018) at La Sapienza, University of Rome under the supervision of Prof. D. Dini. Then, he joined the University of Turin as post-Doc researcher where he is currently working as an assistant professor. His work is mainly related to the synthesis and characterization of innovative materials for emerging photovoltaics. More recently, he has been involved in the investigation of structural and electronic properties of ionic liquids and deep eutectic solvents for energy-related application. He is (co)author of 52 publications (h-index 15, >600 citations) in international peer-reviewed journals.



Waad Naim is a Ph.D. student with the supervision of Dr. Frédéric Sauvage at the Laboratoire de Réactivité et Chimie des Solides (LRCS), Université Picardie, in Amiens, France. She received her bachelor's degree in physical chemistry in 2016 from Lebanese University. Then she received her M.S. in Advanced Spectroscopy in Chemistry in 2018 from Université de Lille. Her current research focuses on transparent photovoltaic based on NIR-DSSC technology.



Nadia Barbero is an assistant professor in Organic Chemistry at the University of Turin and her research interests are focused on the design and synthesis of new organic and hybrid materials for nonconventional and technological applications (nanotechnology, biotechnology and dye-sensitized solar cells). She has a long experience in NIR-DSSC and is currently involved in IMPRESSIVE EU project for the development of transparent solar cells. She is (co)author of 72 publications (h-index 24, >1300 citations).



Thomas Alnasser got his M.Sc. degree in Chemistry in 2009 at the Ecole Nationale Supérieure de Chimie, Biologie et Physique in Bordeaux (ENSCBP). Then he defended his Ph.D. thesis in Chemistry of nanomaterials in 2013 at Institut de Chimie de la Matière Condensée de Bordeaux (ICMCB). After two consecutive post-doctoral fellowships (LPCNO, Toulouse and LRCS, Amiens), he specialized in the synthesis, organization and characterization of various colloidal nanoparticles, covering a wide field of applications such as sensors, hard disk drive, light emitting devices and photovoltaics.



Iva Dzeba received her Ph.D. in Natural Sciences in the field of Chemistry from the University of Zagreb in 2015. After that she was working for 3 years as a postdoc in the field of photochemistry at Division of Materials Chemistry at Ruder Boskovic Institute. In 2019, she joined the Laboratory of Reactivity and Chemistry of Solids at the University of Picardie Jules Verne where she worked on photophysical characterization of DSSC. She is currently working as a researcher at Ruder Boskovic Institute. Her research interest includes photophysics and photochemistry of different systems.



Marco Giordano received his master's degree in Industrial Chemistry in 2018 at the University of Torino with a thesis on copper complexes for redox mediators in DSCs. In 2019 he joined European project IMPRESSIVE as junior researcher. Since the same year, he is a Ph.D. student in Chemical and Material Sciences at the University of Torino under the supervision of Prof. G. Viscardi. His research is focused on the synthesis of NIR sensitizers and redox couples for application in dye-sensitized solar cells.



Arshak Tsaturyan received his Ph.D. in Physical Chemistry in 2014 at Southern Federal University (Russia), under the supervision of Prof. V. A. Kogan. He is senior researcher at the Institute of Physical and Organic Chemistry at Southern Federal University. He had a fellowship at the University of Turin with prof. C. Barolo. His research interests are focused on the theoretical study of the electronic structure and photophysical properties of coordination compounds. He is (co)author of 40 publications in international peer-reviewed journals.



Maxence Urbani is a research staff in organic synthesis at *IMDEA-Nanociencia* (Madrid, Spain) in the Prof. Tomas Torres's group. His current research interests include the preparation and study of porphyrinoid molecules for their application in molecular photovoltaics, supramolecular chemistry and on-surface synthesis. His work results in more than 35 peer-reviewed article and more than 1300 citations.



Tomás Torres is the head of the Institute for Advanced Research in Chemical Sciences (IAdChem) and full professor of Organic Chemistry at the Autonoma University of Madrid and associated senior scientist at the IMDEA Nanoscience Institute. In addition to various fields of synthetic and supramolecular chemistry, his current research interests include the preparation and study of organic functional materials. His group, consists of 25 researchers, is currently exploring several areas of basic research and applications of phthalocyanines, porphyrins, and carbon nanostructures (e.g., fullerenes, carbon nanotubes, graphene), including organic and hybrid solar cells, and photodynamic therapy, with a focus on nanotechnology.



Claudia Barolo is a full professor of Industrial Chemistry at the Department of Chemistry of the University of Torino. Her research interest is focused mostly on the synthesis and characterization of organic and hybrid functional materials (from molecules to polymers) able to interact with light and their possible application in energy related fields (optoelectronics, lighting, and solar cells). She is also vice-coordinator of the PhD programme in Innovation for the Circular Economy at the University of Turin. Her work resulted in more than 125 publications (h-index 35, >4000 citations).



Frédéric Sauvage is currently research director at CNRS and group leader at the LCRS. He obtained his Ph.D. in 2006 under the supervision of Prof. Tarascon, post-doctoral fellow at Northwestern University (Prof. Poepplmeir) and joined the Swiss Federal Institute of Technology within the group of Prof. Grätzel. His research interest is on stability of dye-sensitized solar cells and perovskite solar cells, developed the concept of the transparent and colorless dye-sensitized solar cells based on wavelength selective NIR sensitization. He has published >90 peer-review articles, inventor of 8 patents and coordinator of the Impressive project funded by the EC.